CASL-U-2013-0181-001

Power uprates
and plant life extension

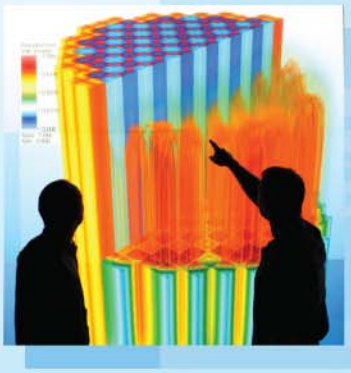

Engineering design
and analysis

Science-enabling
high performance
computing

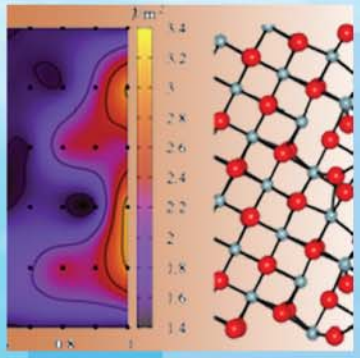

Fundamental science

Plant operational data

Consortium for Advanced Simulation of LWRs

Demonstration & Assessment of Advanced Modeling Capabilities for Multiphase Flow with Sub-cooled Boiling L2.THM.P7.01

Emilio Baglietto
Massachusetts Institute of Technology

Mark A. Christon
Los Alamos National Laboratory

Contributing PI's:
Jacopo Buongiorno
Yassin Hassan
Masahiro Kawaji
Gretar Tryggvason
Igor Bolotnov
Annalisa Manera
Michael Z. Podowski
Sreekanth Pannala
Jozsef Bakosi
Lori Pritchett-Sheats
Robert Nourgaliev

August 30, 2013

U.S. DEPARTMENT OF ENERGY | Nuclear Energy

REVISION LOG

Revision	Date	Affected Pages	Revision Description
0	08/30/2013	All	Initial Issuance
1	12/23/13	All	Revision received by Emilio

Document pages that are:

Export Controlled _____ _____

IP/Proprietary/NDA Controlled _____

Sensitive Controlled_____

Requested Distribution:

To:

CASL Senior Leader Team (SLT)

Extended Leadership Team (ELT)

Copy:

EXECUTIVE SUMMARY

This milestone is dedicated to demonstrating and assessing the advanced modeling capabilities that are being developed for application to multiphase flow with sub-cooled boiling. The theoretical framework for this development effort is Multiphase Computational Fluid Dynamics (M-CFD), which represents the central advancement in order to introduce the necessary first principle generality and 3-dimensional capabilities. The M-CFD approach has the demonstrated potential to overcome the limitations of current lumped-parameter methods typically referred to as "subchannel models".

The report documents the unavoidably broad efforts in the Thermal Hydraulics Focus Area, which is necessary to tackle the challenge of delivering robust M-CFD capability. Three key areas have been developed and are discussed in this report:

- development of a New Computational Framework
- deployment of Hardened Boiling Models
- construction of an Integrated M-CFD Closure

The report further describes the experimental and computational work that provides the bases to support the 3 key deliverables. Their contribution has been a crucial factor in the introduction of new models based on improved physical understanding, and this understanding is one of the primary focal points of this report.

An essential aspect that this milestone addresses is the need for improved closure generality to extend the predictive M-CFD capabilities. This feature should exemplify the key interpretation of the milestone objective. The goal of this work is to assess the delivered capabilities and direct the future improvements, as well as prepare the VERA CFD codes to be capable to first include and then further extend the capabilities beyond the current state-of-the-art.

Specifically, the milestone work has been completed in the following areas:

1) Construction of a baseline closure leveraging the existing extensive analysis and validation work.

2) Assessment of the potential of the baseline closure in comparison with existing state-of-the-art closure from PSBT benchmark experience.

3) Introduction of a second-generation closure from CASL-specific learning.

4) Delivery of common components derived from CASL experimental and ITM/DNS work.

5) Derivation of a new multiphase flow CFD approach for VERA CFD tools.

6) Delivery of VERA CFD first generation multiphase flow capabilities in Hydra-TH, with preliminary testing.

The models and capability delivered from this milestone provide the base for supporting the application of advanced modeling capabilities towards the pre-assigned DNB objective.

CONTENTS

EXECUTIVE SUMMARY iii

CONTENTS iv

FIGURES vi

TABLES viii

1. MILESTONE DESCRIPTION 1
1.1 Approach and Implementation 2
1.2 Working Group 4

2. BASELINE CLOSURE 6
2.1 General Description 6
2.2 RPI Closure Modeling Background 7
2.3 Derivation of a Reference Baseline Closure 8
2.3.1 Bubble Forces 8
2.3.2 Interfacial Heat Transfer 9
2.3.3 Wall Heat Transfer (Heat Partitioning for Forced Convection Sub-Cooled Boiling) 10
2.4 Assessment of the Baseline 11
2.4.1 New RPI-NPHASE model vs. STAR-CCM+ reference model 12
2.4.2 Implementation of the new RPI model in STAR-CCM+ 13
2.5 Conclusions and Future Work 16

3. ADVANCED BOILING CLOSURE 17
3.1 Modeling a New Physical Understanding 17
3.1.1 MIT Flow Boiling Facility 17
3.1.2 A New Look at Flow Boiling 20
3.2 Advanced Boiling Closure Formulation 27
3.2.1 GEN-I Heat Partitioning Limitations 27
3.2.2 GEN-II Heat Partitioning Model 28
3.3 Hardened Momentum Closure 40
3.3.1 Wall-Aware Lift Closure Formulation 41
3.4 The role of ITM/DNS work 45
Description of ITM/DNS Codes 45
PHASTA 45
Governing Equations 45
Level Set Method 46
FTC3D 47
ITM case design 48
Data extraction and drag/lift force measurement approach 49
Results for PHASTA simulations and measurements 51
Results for FTC3D simulations and measurements 62
Future Work 67

4. Hydra-TH MULTIPHASE FLOW 68
4.1 The Multiphase Development Plan 68

4.2 Multiphase Flow Algorithms 69
4.2.1 Fully-Implicit Algorithms 70
4.2.2 Fully-Coupled Momentum Exchange 73
4.3 General Purpose Library for Steam Properties 77
4.3.1 Water Property Models 78
4.3.2 Tabulation of Properties 79
4.4 Hydra-TH Multiphase Calculations 82
4.4.1 3x3 Rod Bundle 82
4.4.2 5x5 Rod Bundle 83

5. SUMMARY 86

6. REFERENCES 87

FIGURES

Figure 1: Flowchart of milestone implementation. 1
Figure 2: Flowchart of milestone implementation. 3
Figure 3: Flowchart of milestone contributors. 5
Figure 4: Graphical review of state-of-the- art M-CFD. 6
Figure 5: Performance of the new RPI model implemented in NPHASE and the reference STAR-CCM+ model against the Bartolomei experiment. Left: cross-section averaged liquid temperature as function of elevation; right: wall temperature (Tw) and liquid centerline temperature (Tcl) as function of elevation. 13
Figure 6: Performance of the new RPI model implemented in NPHASE and the reference STAR-CCM+ model against the Bartolomei experiment. Left: cross-section averaged void fraction as function of elevation; right: void fraction radial distribution at the test section outlet. 13
Figure 7: Performance of the new RPI model implemented in STAR-CCM+ and STAR-CCM+ model against the Bartolomei experiment - effect of gas-liquid interface to liquid heat transfer on liquid and wall temperatures. 14
Figure 8: Performance of the new RPI model implemented in STAR-CCM+ and STAR-CCM+ model against the Bartolomei experiment - effect of gas-liquid interface to liquid heat transfer on the void fraction. 14
Figure 9: Performance of the new RPI model implemented in STAR-CCM+ and STAR-CCM+ model against the Bartolomei experiment - effect of bubble departure diameter on liquid and wall temperatures. 15
Figure 10: Performance of the new RPI model implemented in STAR-CCM+ and STAR-CCM+ model against the Bartolomei experiment - effect of bubble departure diameter on the void fraction. 15
Figure 11: Performance of the new RPI model implemented in STAR-CCM+ and STAR-CCM+ model against the Bartolomei experiment - effect of heat partitioning on liquid and wall temperatures. 15
Figure 12: Performance of the new RPI model implemented in STAR-CCM+ and STAR-CCM+ model against the Bartolomei experiment - effect of heat partitioning on the void fraction. 16
Figure 13: Experimental setup for HSV and IR thermography (left), picture of the quartz section (middle), and diagram of flow channel with the heated area shown in red. 18
Figure 14: HSV (top) and IR (bottom) images for a high heat flux case. Heat flux: 600 kW/m^2-s, mass flux of 200 kg/m^2-s; subcooling: 9ºC; pressure:1.05 bar. 21
Figure 15: Surface temperature vs. time averaged over a 0.1-mm radius area on heater surface about the nucleation site circled in red in 21
Figure 16: HSV (top) and IR (bottom) of a bubble from the onset of sliding (t=0 ms) to the edge of the frame (t=166 ms). Heat flux: 130 kW/m^2/s; mass flux: 200 kg/m^2/s; subcooling: 10ºC; pressure: 1.05 bar 22
Figure 17: Temperature profile along the sliding bubble path at various time steps. t=0 is the onset of bubble sliding. The circles on the plot show the approximate position of the bubble at each time step. (The measurement uncertainty on temperature is $\pm$2.0℃; error bars not shown) Heat flux: 130 kW/m^2/s; mass flux: 200 kg/m^2/s; subcooling: 10ºC; pressure: 1.05 bar 23
Figure 18: Bubble departure diameters vs. mass flux for 1.05 bar and 15ºC subcooling (a), 10°C subcooling (b), 5ºC subcooling (c). Bubble departure diameters vs. mass flux for 1.5 bar and 15ºC subcooling (d), 10°C subcooling (e), 5ºC subcooling (f). 24
Figure 19: Example distribution of bubble periods. 25
Figure 20: Bubble period vs. wall superheat for 1.05 bar and 15ºC subcooling (a), 10°C subcooling (b), 5ºC subcooling (c). Bubble period vs. wall superheat for 1.5 bar and 15ºC subcooling (d), 10°C subcooling (e), 5ºC subcooling (f). 26
Figure 21: Depiction of the heat flux partitioning for subcooled flow boiling. 28
Figure 22: ITM Test Case 1 computational domain and illustration of the hemispherical obstacles [31]. 31
Figure 23: Velocity profile near the wall for a smooth surface and a surface with hemispherical obstacles. 32
Figure 24: Illustration of microlayer evaporation and condensation on a bubble attached to a heated wall. 33
Figure 25: Depiction of the microlayer with the maximum thickness shown. 33
Figure 26: Illustration of the maximum number of active nucleation sites on a heated surface with a magnified view to show the dry area, microlayer area, and the area of influence for a single bubble. 34
Figure 27: Illustration of the implementation of the maximum active nucleation site density. 35
Figure 28: Illustration of bubble growth at a nucleation site until it departs from the site and slides and lifts-off the heater surface. 36
Figure 29: Illustration of a bubble sliding from its inception point and then departing from the heater after sliding a distance $\boldsymbol{l}$. 37
Figure 30: Illustration of bubble growth on a heater and the area in the influence of the bubble that is involved in the quenching heat flux. 39

Figure 31: CFD representation of a boiling channel 40
Figure 32: Local closure approach for PWR application. 41
Figure 33: Lift/Wall forces near the wall of a bubbly pipe flow [23]. 42
Figure 34: Surface plot of DRP model and pointwise data for Re > 2 44
Figure 35: Surface plot of DRP model and pointwise data for Re ≤ 10 44
Figure 36: The front tracking code uses a fixed structured grid for the solution of the fluids equation and an unstructured surface grid to track the interface between the different fluids. 47
Figure 37: Simulation domain and control forces. Left: Setup and coordinates for the PHASTA runs. Right: Setup and coordinates for the FTC3D runs. 48
Figure 38. Summary of the S1/R25 case with uniform shear of 1.0. Top left shows sample of velocity distribution around the bubble, bottom left and right: control force evolution in horizontal and vertical directions, respectively. Top right shows basic case parameters and lift/drag coefficient evaluation results. 53
Figure 39. Summary of the S5 case with uniform shear of 5.0. 54
Figure 40. Summary of the S10 case with uniform shear of 10.0. 55
Figure 41. Summary of the S50 case with uniform shear of 50.0. 56
Figure 42. Summary of the R50 case with uniform shear of 1.0 with increase relative velocity. 57
Figure 43. Summary of the NSW0.5 case with uniform shear of 2.0. Bubble is located half the radius from the top no-slip wall. 58
Figure 44. Summary of the SW0.5 case with uniform shear of 2.0. Bubble is located half the radius from the top free-slip wall. 59
Figure 45. Summary of the ONSW0.5 case with uniform shear of 2.0. Bubble is located half the radius from the bottom no-slip wall. 60
Figure 46. Lift coefficient dependence on the distance from the wall (measured in bubble radii from the closest point of the interface to the wall). Red line shows the slip-wall condition option. 61
Figure 47. The bubble and the velocity field shown by a quiver plot. The color indicates the vertical velocity component. In the left frame the bubble is in the middle of the domain and in the right frame the bubble is close to the right wall. 64
Figure 48. The horizontal (top) and the vertical (bottom) component of the gravitational acceleration versus time, as adjusted by the PID controllers to keep the bubble stationary. 65
Figure 49. The lift and drag coefficients versus the Eotvos (Eo) number. 66
Figure 50. The lift (a) and drag (b) coefficient versus shear rate. 66
Figure 51. The effect of the distance to the wall on the lift (a) and drag (b) force on the bubbles. 66
Figure 52. The effect of the distance to the wall on the lift (a) and drag (b) force on the bubbles for a bubble Reynolds number = 50. 67
Figure 53: Diagram of codes, solution methods and Hydra-TH development stages. 69
Figure 54: Time-dependent differentially heated cavity problem. 70
Figure 55: Convergence history during multiple time-steps. 71
Figure 56: Temporal convergence rates and algorithmic domains for projection methods. 71
Figure 57: Re=100 flow past a cylinder with $\mathbf{3.5} \leq \boldsymbol{CFL} \leq \mathbf{60}$. 72
Figure 58: Convergence rates for fully-implicit projection and PISO algorithms. 73
Figure 59: Drag force verification problem. 74
Figure 60: Asymptotic phasic velocities for drag acting in the x, y and z-coordinate directions. 75
Figure 61: Asymptotic drag test for 5-fields with equal volume fractions. 75
Figure 62: Effect of bubble diameter on phasic velocity. 76
Figure 63: Effect of varying volume fraction on the asymptotic velocity. 76
Figure 64: Terminal velocity verification problem. 77
Figure 65: Tabulated density surface with triangulation overlaid in blue for the IAPWS-IF97 model. 80
Figure 66: Tabulated adiabatic sound speed surface with triangulation overlaid in blue for the IAPWS-IF97 model. 80
Figure 67: 3x3 Rod bundle showing a) boundary conditions on rod, spacer surfaces, and the sub-channel boundaries, b) surface mesh of the rod surface and spacer grid. 82
Figure 68: Snapshot of isosurfaces of the instantaneous phasic volume fraction near the spacer grid using the 2M mesh. 83
Figure 69: Flow domain for the 5x5 rod bundle showing the rods, the inlet/outlet planes, rod support, and the spacer grid. 84
Figure 70: Snapshot of the instantaneous bubble velocity in the streamwise direction. 84
Figure 71: Isosurfaces of the velocity magnitude for the velocity difference between the continuous liquid and bubble phases with the color indicating the magnitude of the streamwise drag. 85

TABLES

Table 1- Test matrix performed for 1.05 and 1.5 bar, and for subcoolings of 5, 10, and 15ºC. _____ *19*
Table 2 - Comparison of potential experiment conditions to PWR conditions and associated RPP. _____ *20*
Table 3. Definition of variables used in the smooth wall function. _____ *29*
Table 4. PHASTA mesh / simulation parameters _____ *52*
Table 5. The various parameters used for the FTC3D baseline case. _____ *63*
Table 6: Timing comparison between the fully-implicit projection algorithm in Hydra-TH and PISO in OpenFoam. A 2.66 GHz i7 processor was used for this comparison. _____ *73*
Table 7: Evaluation speed for analytic freesteam model versus three different UTri tabulations of the IAPWS-IF97 model. _____ *81*

1. MILESTONE DESCRIPTION

This milestone is intended to demonstrate & assess advanced modeling capabilities for multiphase flow with sub-cooled boiling for implementation in the Consortium for Advanced Simulation of Light Water Reactors (CASL) CFD codes. The end target of the work is to support advanced capabilities for Departure from Nucleate Boiling (DNB)-related predictions.

DNB is one of the safety-related Challenge Problems (CP) that CASL is addressing in support of Pressurized Water Reactor (PWR) power uprate, high fuel burnup, and plant lifetime extension. DNB occurs when the fuel rod clad surface is overheated due to formation of a local vapor layer, causing dramatic reduction in heat transfer capability and leading to fuel rod failure and radiation release. DNB is also referred to as Critical Heat Flux (CHF) and boiling crisis. It is one of the specified acceptable fuel design limits (SAFDL) that should not be exceeded during normal operation or anticipated operational occurrences (AOOs). The current regulatory acceptance criterion is that there should be a 95-percent probability at a 95-percent confidence level that a hot or limiting fuel rod in any PWR reactor core will not experience DNB during normal operation or AOOs [1].

This milestone describes and assesses the state of the advanced Thermal Hydraulics (T/H) capabilities development directed to DNB-related predictions. The framework of the T/H development is Multiphase Computational Fluid Dynamics (M-CFD), which is required in order to introduce the necessary first principle generality and 3-dimensional capabilities, which will allow overcoming the limitations of current subchannel analysis techniques.

Figure 1 provides a quick qualitative view of the key gains attainable from the availability of a 3-dimensional predictive multiphase flow T/H tool. From left to right, the new capabilities will provide new insights into local boiling heat transfer, for example in the mixing/and non-mixing vane grids region, 3 dimensional distribution of void inside the fuel assembly, which is for example one of the key aspects in supporting the modeling of Crud Induced Localized Corrosion (CILC), and further local prediction of local DNB mechanism.

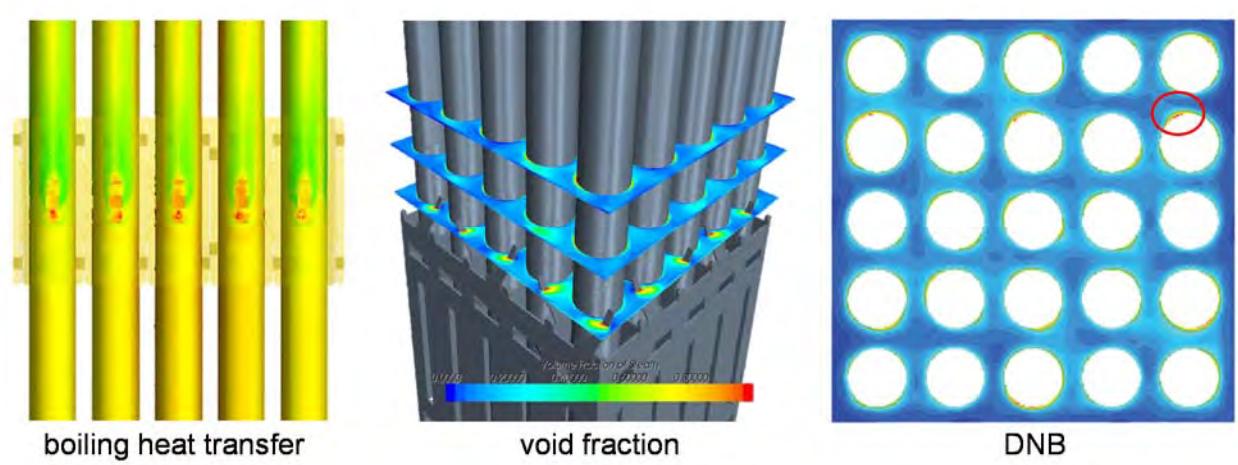

Figure 1: Flowchart of milestone implementation.

While single phase CFD has reached considerable maturity for fuel related applications, multiphase capabilities represent a fundamental next step to support the industry needs captured by the CASL challenge problems. In this sense, M-CFD is a challenge that relies on the mechanistic validity of its closure. Previous experience and industrial application are still limited. In this regard the nuclear industry has led this effort, as it could provide significant immediate benefits to the plant economics. Earlier research efforts, such the DOE sponsored Numerical Nuclear Reactor (DOE INERI 2001-04) (EPRI/DOE 2005-2007) and the OECD/NEA sponsored international benchmarks BFBT and PSBT [2-3] have made a great contribution in setting the bases and clearly constitute the starting point of this work. This work can therefore leverage the clear objective, and well-defined industry need for a predictive and robust M-CFD capability.

This report documents the cross-Focus-Area collaborative effort that is required to tackle the targeted robust M-CFD challenge. Three key areas have been developed and are discussed in this report: (1) the development of a New Computational Framework, (2) the deployment of Hardened Boiling Models, and (3) the construction of an Integrated M-CFD Closure. Further, computational simulations based on direct numerical simulation (DNS) of multiphase flow, and experimental work are an integral part of the effort, first to complete the understanding and support and drive the modelers effort, and second to provide calibration and validation data for the new framework. Their contribution has been a crucial factor in the introduction of new models based on improved physical understanding and is discussed in this report.

An important aspect of this milestone is the rigorous evaluation of the closure generality and their predictive capabilities. This effort focused on identifying the weaknesses and the need for future support activities. The goal of this milestone work is to assess the delivered capabilities and direct the future improvements effort as well as prepare the VERA CFD codes to be capable to first include and further extend the capabilities beyond the current state-of-the-art.

1.1 Approach and Implementation

The approach to the milestone work relies on a collaborative and synergetic work inside the CASL Thermal Hydraulics Methods (THM) Focus Area. The main challenge in the implementation is related to coordinating the various activities in a structure that allows sufficient independency of each task while still maintaining the necessary interaction, and further allowing for flexibility and minimal redundancy as fundamental risk mitigation strategies. The implementation adopted in this work is therefore based on 4 fundamental points:

1) Separation of Modeling and Computational Framework Development;
2) Built-in minimal redundancy;
3) Successive delivery of Gen 1 and Gen 2 models;
4) Dynamic interaction across multiple teams.

Figure 2 provides a flow chart description of the implementation concept. First of all the separation of Modeling and Computational Framework Development is evident. On the left side of the figure the closure modeling efforts are shown, while the core development team is in charge of the Hydra-TH methods development and implementation, a CFD team is also active and responsible for testing, V&V and VUQ activities. While these activities are not a part of this milestone it is important to note the interaction as the Core Development must efficiently interact with the VUQ activities during the platform design.

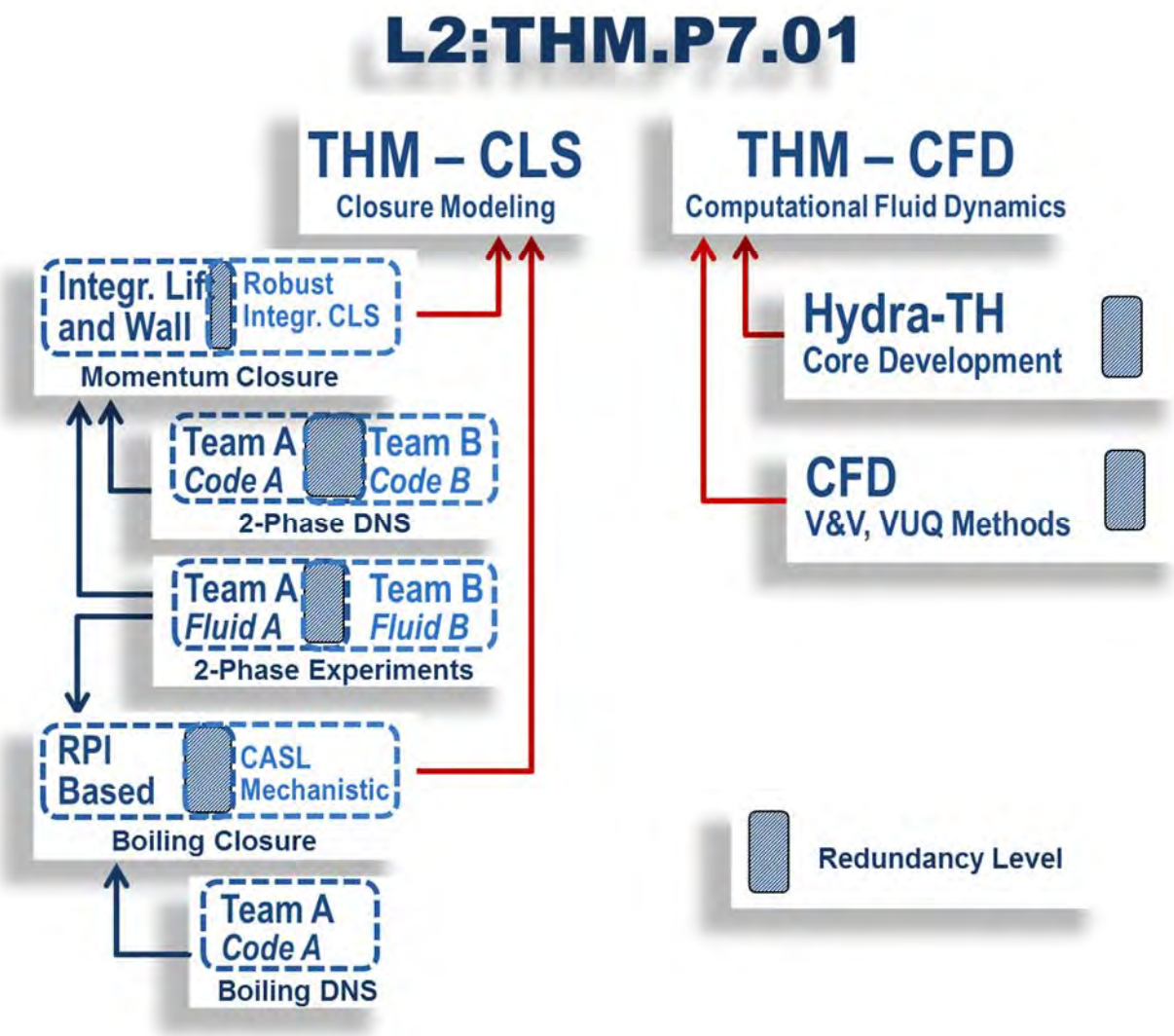

Figure 2: Flowchart of milestone implementation.

On the left side of Figure 2 the Closure Modeling activities are represented. The structure is immediately evident, indicating where all activities are defined and assigned to separate teams. As mentioned this is necessary to allow sufficient agility and to permit the teams to make progress independently. The Closure Modeling work is explicitly subdivided into 2 interdependent modeling activities: the momentum closure and the boiling closure work. Both

these teams interact with the DNS and the Experimental teams in order to provide specifications for supporting data and to leverage the physical insights in their modeling work. These interactions will be made clearer in the later sections where the work is described in detail.

Figure 2 further shows how most activities rely on the effort of multiple teams. This is a key aspect to address 2 of the previously listed points. Firstly the timeline requires that for each model 2 subsequent Generations of models are delivered. The Gen-1 models represent the improvement of existing conceptual closure based on the newly available, and dedicated, experimental and DNS work. Gen-1 represents the baseline model to be implemented in the Hydra-TH code, and should leverage the existing experience and validation facilitating timely software delivery. At the same time the experimental and DNS activities have provided fundamentally new physical understanding that has allowed the construction of new mechanistic approaches which will represent the Gen-2 delivery and will be benchmarked and evaluated versus the robust Gen-1 results. For each activity the flowchart in Fig. 2 also shows different levels of redundancy. Such redundancy represents a built in acceleration and mitigation strategy. While the separate teams conduct independent work covering the broadest technical coverage, the redundancy allows for leveraging of expertise, methods and results for cross-validation, and in the extreme case of failure of one of the activities guarantees that the minimal capability is still delivered for the success of the overall project.

1.2 Working Group

The milestone relies on the coordinated effort from all the listed individuals, which bring together a unique set of skills and experience in collaborative research projects. A deeper look at the team members would allow appreciating a unique balance of expertise, and very importantly a “generational” balance that has proven to be a key tool for acceleration of the project. Figure 3 provides a more complete view of the milestone contributors and their interaction.

Name	Subtask	Affiliated Organization
Jacopo Buongiorno	2-Phase Experiments	MIT
Yassin Hassan	2-Phase Experiments	TAMU
Masahiro Kawaji	2-Phase Experiments	CCNY
Gretar Tryggvason	2-Phase DNS	ND
Igor Bolotnov	2-Phase DNS	NCSU
Annalisa Manera	Gen-1 Closure	U-Michigan
Victor Petrov	Gen-1 Closure	U-Michigan
Michael Z. Podowski	Gen-1 Closure	RPI
Sreekanth Pannala	Momentum Closure	ORNL
Jozsef Bakosi	Hydra-TH	LANL
Lori Pritchett-Sheats	Hydra-TH	LANL
Robert Nourgaliev	Hydra-TH	INL

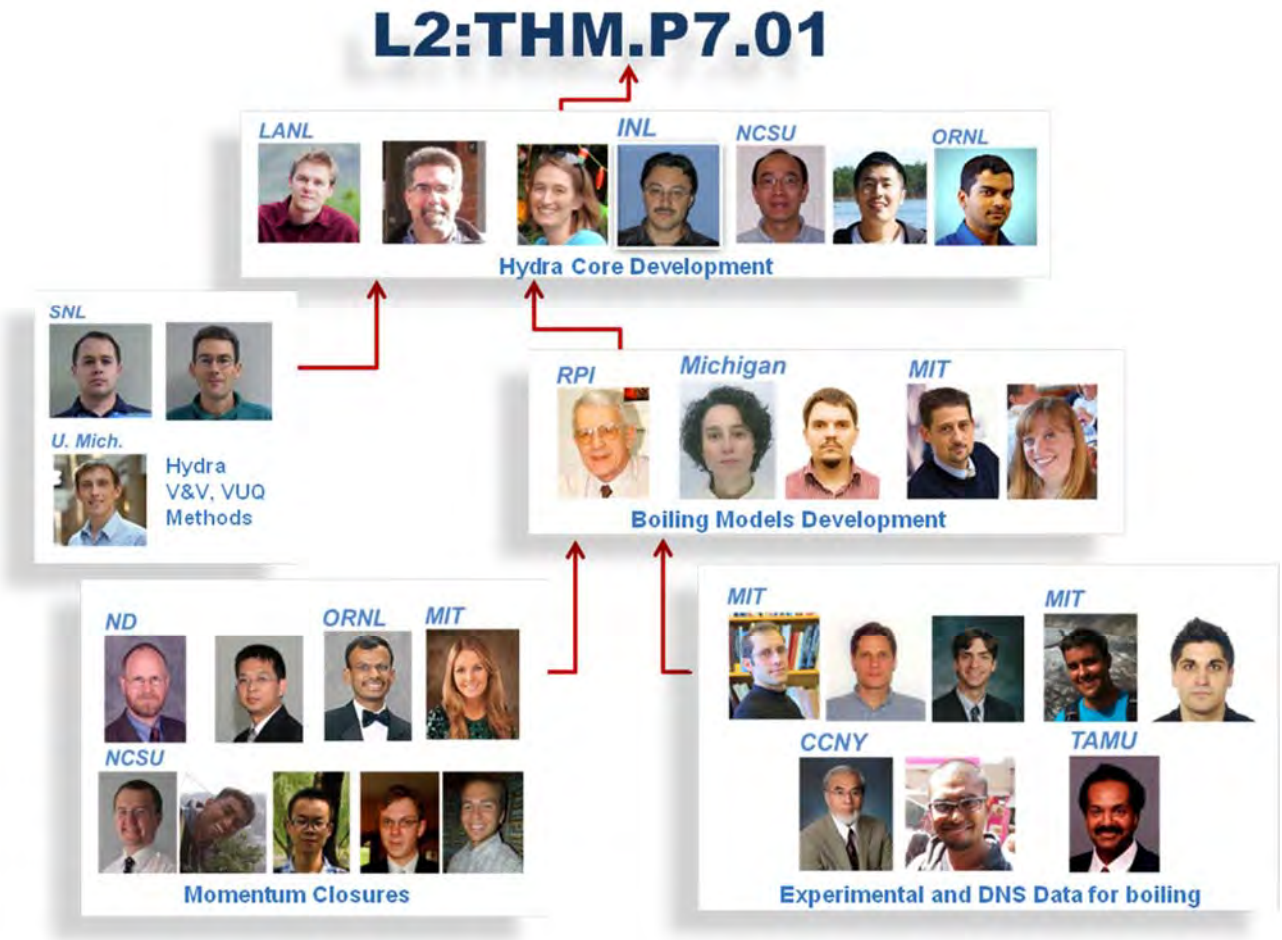

Figure 3: Flowchart of milestone contributors.

2. BASELINE CLOSURE

2.1 General Description

The target of this activity was to deliver a robust M-CFD closure as a baseline for future implementation in Hydra-TH. The reasoning adopted in the baseline model construction was to leverage the experience gained from the international benchmark activities [2-4] and the relative current state-of-the-art methods, and to enhance these methods by collecting dedicated experimental datasets and 2-phase DNS results.

Figure 4 provides a very basic but significant graphical representation of the importance and lessons learned in M-CFD applications to reactor core simulation. While the BWR experience (BFBT, 2007) showed the complexity of modeling a wide range of flow regimes, the PWR experience (PSBT, 2010) evidenced how modeling the wall boiling and therefore the correct near wall temperature and near wall void fractions is at the same time the dominant factor towards accurate DNB predictions, and the most challenging component of the work.

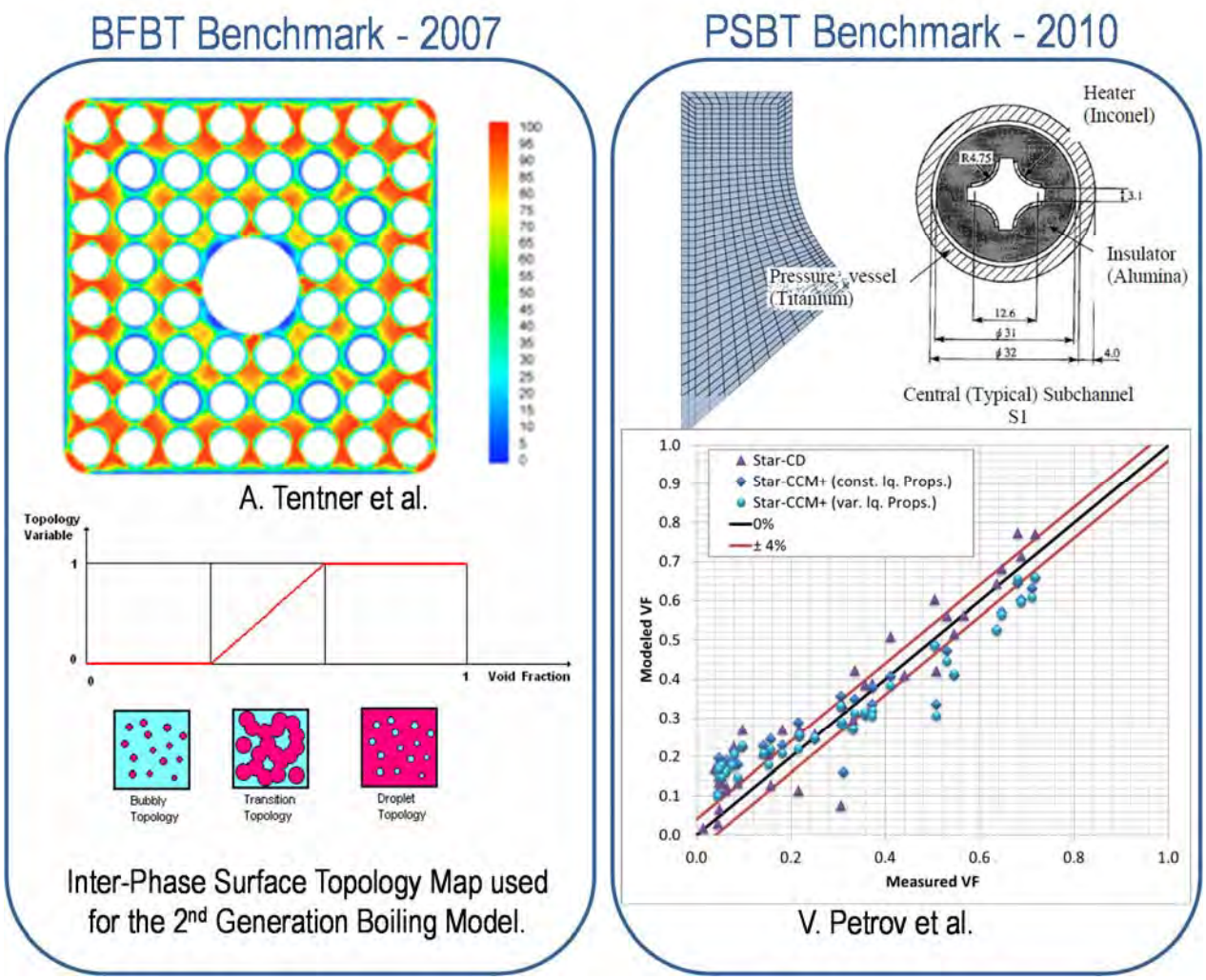

Figure 4: Graphical review of state-of-the- art M-CFD.

With this evidence in mind, the first step was to confirm and further understand the influence of the modeling terms in the M-CFD closure, and to better focus the effort of the experimental and DNS work. Early in the program a specific milestone (L3-THM-CFD-P3-01) was completed to provide a quantitative sensitivity of the M-CFD predictions to parameters in the boiling and multi-phase flow models. The code adopted for the sensitivity study was the commercially available STAR-CD code, which was consistent with the BFBT and PSBT applications. Results of the sensitivity clearly indicated that a better understanding of the wall boiling was of foremost importance, as the evaporative heat flux quantification, and especially the prediction of the bubble departure diameters during boiling have the greatest effect on the accuracy of the simulations.

The scope of the present work was therefore focused on improving the most limiting factors that had been identified by the L3-THM-CFD-P3-01 milestone work. The approach adopted was based on capturing the results in the model development and validation that had been performed by the group at RPI during the CASL project and to port it into the commercial tools STAR-CCM+ for verification and testing. Making the model available in STAR-CCM+ allows a direct comparison to the PSBT model and therefore to the existing state of the art. Further it will make an early deployment available to CASL partners while the VERA T/H tools complete their development.

2.2 RPI Closure Modeling Background

The contribution of the RPI group to THM has been specifically directed towards the continuous improvement of closure modeling for multiphase flows with sub-cooled boiling. A specific milestone (L3:THM.CLS.P6.02) was completed to support the current work and allow a timely delivery of a baseline closure.

The major achievements of the RPI activities, and which have been incorporated in the present work can be listed as follows (a complete literature survey of this work is available in References 4-10):

- A new improved local model for predicting the heated wall temperature in sub-cooled boiling has been formulated.
- Extensive work has been performed on testing the sensitivity of results to the assumptions used in the formulation of closure laws for the near wall combined evaporation and condensation phenomena.
- Multidimensional aspects of local interfacial heat transfer between vapor bubbles and sub-cooled liquid inside heated channels have been tested and analyzed.
- Model validation against selected experimental data has been carried out.
- The modeling framework has been formulated for the analysis of the effect of non-uniform power distribution on sub-cooled boiling in a section of PWR fuel assembly.

The work at RPI has provided a considerable advancement in the understanding of the wall boiling modeling behavior, and the testing has shown that considerable improvements in the robustness and generality of the overall closure could be obtained. The scope of this milestone

has therefore been to implement these findings in the commercial tool STAR-CCM+ and assess their efficiency in order to establish a robust baseline.

2.3 Derivation of a Reference Baseline Closure

While the basic equations of the Eulerian M-CFD are not included here for sake of brevity as they are later discussed in the CFD tool development section, the assembled reference closure is reported here as follows:

2.3.1 BUBBLE FORCES

Drag force

The drag force acting on the bubbles is given by:

$$\overrightarrow{F_D} = -\frac{3}{4}\frac{C_D}{D_b}\alpha\rho_l|\vec{u}_v - \vec{u}_l|(\vec{u}_v - \vec{u}_l) \qquad 2.1$$

where the drag coefficient used in most two-phase flow formulations is the one computed for a sphere:

$$C_D = \frac{24}{Re_b}\left(1 + 0.1Re_b{}^{0.75}\right) \qquad 2.2$$

With the bubble Reynolds number defined as:

$$Re_b = \frac{\rho_l|\vec{u}_v - \vec{u}_l|D_b}{\mu_b} \qquad 2.3$$

with D_b being the bubble diameter. The drag coefficient is modified in the RPI model according to the following correlation:

$$C_D = \frac{24}{Re_b}\left(1 + 0.092Re_b{}^{0.78}\right) \qquad 2.4$$

Lift force

The force acting on the bubbles is given by:

$$\overrightarrow{F_L} = -C_L\alpha\rho_l|\vec{u}_v - \vec{u}_l| \times \left(\vec{\nabla} \times \vec{u}_l\right) \qquad 2.5$$

where the lift coefficient C_L is case dependent. For the Bartolomei case included in the model assessment reported in the next chapters, a coefficient of $C_L = 0.03$ was used.

In the RPI model, the lift force is applied at a distance from the wall greater than one bubble diameter. For smaller distances, the calculations of void fraction based on force balance are invalid, so it is assumed that the lift coefficient is zero in that region. Alternative models reported in the literature do not assume the lift force to be zero close to the wall, but they do compensate with the so-called Antal's force, which pushes the bubbles away from the wall.

Turbulent dispersion force

$$\vec{F}_{TD} = -C_{TD}\alpha\rho_l\overline{\overline{k}}_l\nabla\alpha \qquad 2.6$$

where $\underline{\underline{k}}_l = \overline{(u'_{l,i}u'_{l,j})}\delta_{ij}$ for i,j=1,2,3, and δ_{ij} is the Kronecker delta.

$$\text{with } C_{TD} = 2/3 \qquad 2.7$$

Virtual mass

$$\vec{F}_{vm} = -C_{vm}\alpha\rho_l\left(\frac{D\vec{u}_v}{Dt} - \frac{D\vec{u}_l}{Dt}\right) \qquad 2.8$$

Where D/Dt represent the usual material derivative with $C_{vm} = 0.5$.

2.3.2 INTERFACIAL HEAT TRANSFER

In the current version of the model, bubbles are assumed to be spherical. Therefore, the interfacial area density is given by:

$$a_i = \frac{6\alpha}{D_b} \qquad 2.9$$

It is assumed that the temperature of the vapor-liquid interface is equal to saturation (T_{sat}). The heat transfer rate between interface and phase j is equal to:

$$q_j''' = N'''A_s h_j\left(T_{sat} - T_j\right) \qquad 2.10$$

with:

N''' = bubble number density → $N''' = \frac{\alpha}{V_b}$

A_s = bubble surface area = $\pi D_b^2/4$

h_j = heat transfer coefficient between interface and phase j

For the liquid phase, the heat transfer coefficient h_l is defined according to the following Nusselt number correlation:

$$Nu = C_{vol}\left[2 + \left(0.4Re_b^{0.5} + 0.06Re_b^{2/3}\right)\right]Pr_l^{0.4} = \frac{h_l D_b}{k_l} \qquad 2.11$$

where C_{vol} is a correction factor to take into account condensation (=1 for single sphere, > 1 because of bubble-induced turbulence). This correction will require further evaluation.

It is further assumed that the heat transfer coefficient between the gas-liquid interface and the gas phase is null.

2.3.3 WALL HEAT TRANSFER (HEAT PARTITIONING FOR FORCED CONVECTION SUB-COOLED BOILING)

The heat partitioning is decomposed into two components, a boiling component (which includes evaporation and quenching) and a single-phase component respectively:

$$q''_w = q''_b + q''_{1\phi} \qquad 2.12$$

The single-phase component is given by:

$$q''_{1\phi} = h_{1\phi}(1 - A''_b)(T_w - T_l) \qquad 2.13$$

with:

T_w = wall temperature

T_l = liquid temperature

A_b'' = fraction of heated surface exposed to boiling

$h_{1\phi}$ = boiling heat transfer coefficient

The boiling heat transfer coefficient is evaluated as:

$$h_{1\Phi} = \rho_l c_{p,l} St_l u_l \qquad 2.14$$

while the fraction of the heated surface exposed to boiling is expressed as:

$$A''_b = n''\varepsilon A_b \qquad 2.15$$

where

A_b = bubble cross-section → $A_b = \pi \frac{{D_b}^2}{4}$

ε = correction coefficient → $\varepsilon = \frac{2\rho_v h_{fg} D_b f}{3q''_w}$

where f is the nucleation frequency. The boiling component including evaporation and quenching is given by:

$$q''_b = A''_b \frac{h_{lg}}{h_{fg}} q''_w \qquad 2.16$$

It is interesting to notice that, substituting the expression 2.15 into Eq. 2.16, the boiling component becomes:

$$q_b'' = n'' f \frac{\pi D_b^3}{6} \rho_v h_{lg} \qquad 2.17$$

which is equivalent to the formulation of the original Kurul-Podowski model for the evaporative heat flux only. The nucleation site density n" is evaluated with the following correlation:

$$n'' = \kappa\left(T_w - T_w^{min}\right)^2 \qquad 2.18$$

where κ is a coefficient, and:

$T_w^{min} = T_{sat} + \Delta T_w^{min}$

ΔT_w^{min} = minimum wall superheat at the onset of nucleation

$$\Delta T_w^{min} = T_w^{min} - T_{sat} = 2\sqrt{\frac{2\sigma q_w'' v_{fg} T_{sat}}{k_l h_{fg}}}$$

2.4 Assessment of the Baseline

Before proceeding with the implementation of the new RPI model within the STAR-CCM+ platform, a comparison between the new RPI model as implemented in NPHASE and the reference model currently available in STAR-CCM+ has been performed, and their performance has been evaluated against the Bartolomei experiment.

It has to be pointed out that a variety of models are available within the STAR-CCM+ code and that users are left with the task of selecting the appropriate correlations for the given case under investigation. The following correlations were selected to assemble what here we refer to as the STAR-CCM+ reference model:

- the bubble hydrodynamics is computed by including lift, drag, virtual mass, and turbulent dispersion forces;
- the heat partitioning is computed according to the original Kurul-Podowski model, consisting of three separate components;
- the heat transfer coefficient from the gas-liquid interface to the liquid is evaluated according to the Ranz-Marshall correlation expressed as:

$$Nu = 2 + 0.6 Re_d^{0.5} Pr_c^{0.3} \qquad 2.19$$

- as in the case of the new RPI model, the heat transfer between the gas-liquid interface and the gas phase is assumed to be null;

- the bubble departure diameter is estimated with the Tolubinski Konstanchuk correlation, specifically developed for sub-cooled liquid:

$$d_w = d_0 \exp\left[-\frac{\Delta T_{sub}}{\Delta T_0}\right] \qquad 2.20$$

  where d_o is a reference diameter (default equal to 0.6 mm), ΔT_o is the reference subcooling (default equal to 45K), and ΔT_{sub} is the subcooling of the liquid next to the wall;
- the bubble departure frequency is given by the Cole's correlation:

$$f = \sqrt{\frac{4}{3}\frac{g(\rho_l - \rho_g)}{d_w \rho_l}} \qquad 2.21$$

  which is equivalent to taking a typical bubble rise velocity (estimated using unit drag coefficient as the velocity scale, over the bubble diameter as the length scale);
- the nucleation site density is given by the Lemmert-Chawla correlation:

$$\frac{n''}{[m^{-2}]} = (m\Delta T_{sup})^p \qquad 2.22$$

  where m is a calibration constant (equal to 185 K^{-1}), p is a superheat exponent (default equal to 1.805), ΔT_{sup} is the wall superheat given by $\Delta T_{sup} = T_w - T_{sat}$.

For the Bartolomei experiment, consistently with the new RPI-NPHASE model, it is further assumed that the bubble diameter is constant and equal to 0.75mm and that the lift coefficient C_L is equal to 0.03.

2.4.1 New RPI-NPHASE model vs. STAR-CCM+ reference model

The comparison of the new RPI-NPHASE model and the STAR-CCM+ reference model is reported in Figure 5 and Figure 6. The two models are evaluated against data measured by Bartolomei. In Figure 5 the cross-section averaged liquid temperature (left), the wall temperature T_W and the coolant center-line temperature T_{cl} (right) are reported along the test section vertical axis. In Figure 6 the cross-section averaged void fraction distribution along the test section vertical axis (left) and the void fraction radial distribution at the test section outlet (right) are reported.

Overall, both models seem to perform reasonably well against the Bartolomei experiment. The STAR-CCM+ reference model gives a better prediction of the center-line fluid temperature in the upper part of the test section.

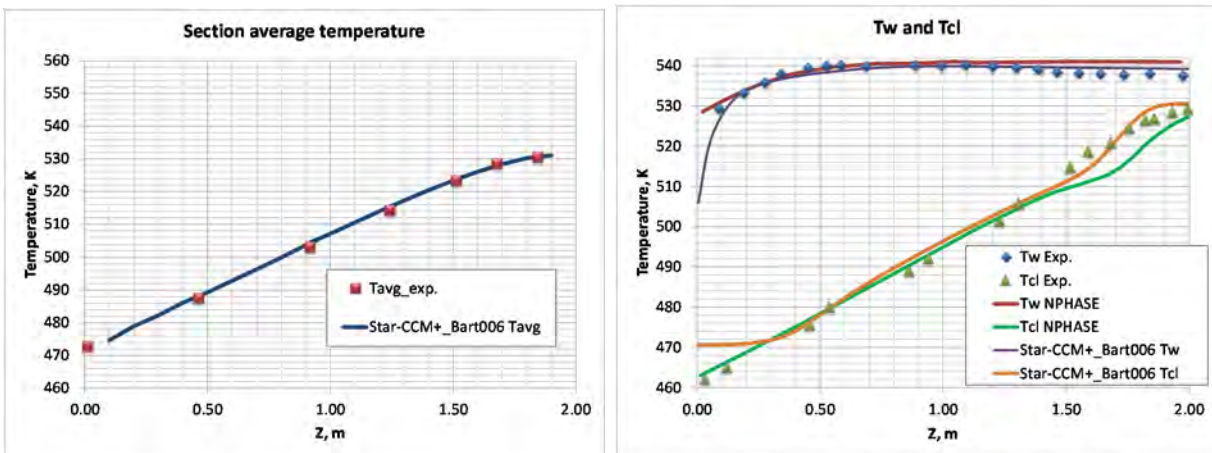

Figure 5: Performance of the new RPI model implemented in NPHASE and the reference STAR-CCM+ model against the Bartolomei experiment. Left: cross-section averaged liquid temperature as function of elevation; right: wall temperature (Tw) and liquid centerline temperature (Tcl) as function of elevation.

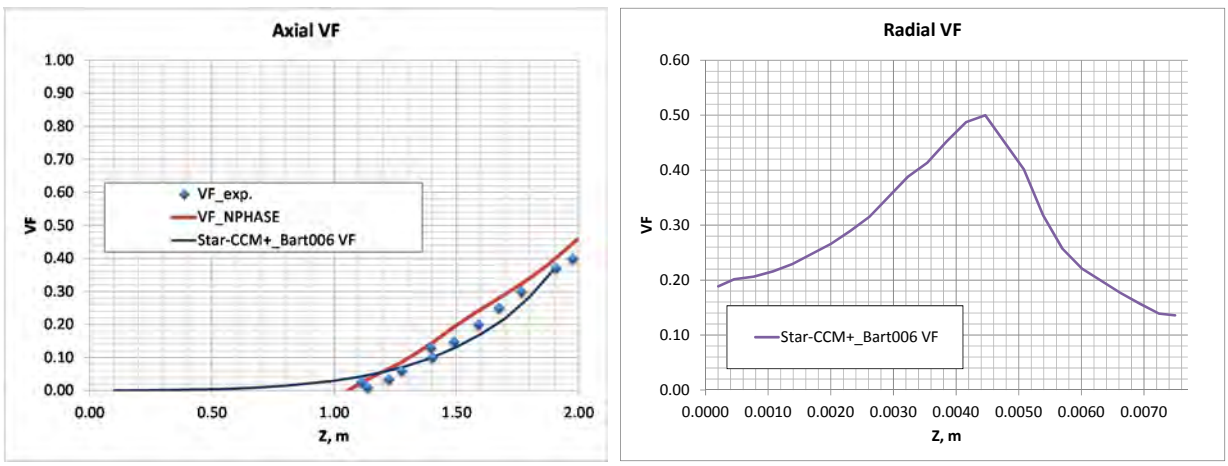

Figure 6: Performance of the new RPI model implemented in NPHASE and the reference STAR-CCM+ model against the Bartolomei experiment. Left: cross-section averaged void fraction as function of elevation; right: void fraction radial distribution at the test section outlet.

2.4.2 Implementation of the new RPI model in STAR-CCM+

In order to systematically investigate the impact of adopting the new RPI correlations on the overall model performance, the implementation of the new RPI model within STAR-CCM+ has been carried out by sequentially substituting the STAR-CCM+ reference model correlations with the ones proposed by RPI.

At first, the Ranz-Marshall correlation for the heat transfer from the gas-liquid interface to the liquid is replaced with eq. 2.11. A coefficient Cvol = 2 has been assumed. As can be seen in Figure 87 and Figure 8, the replacement of the heat transfer correlation has some minor effect on the cross-section averaged void fraction distribution and on the liquid center-line temperature, but the wall temperature seems to remain unaffected by the change.

The replacement of the bubble departure diameter correlation (see Figure 9 and Figure 10) is strongly affecting the radial void fraction distribution (for a given set of bubble forces correlations). The wall temperature was unaffected by the change, for this particular case.

The results obtained by replacing the heat-partitioning model, i.e. with the full implementation of the new RPI model in STAR-CCM+, are presented in Figure 11 and Figure 12. Overall the new model and the reference model perform equally well for the Bartolomei experiment. The wall temperature seems to be affected mainly by the bubble nucleation site density model. The only significant difference is found in the void fraction radial distribution for which no experimental data are available.

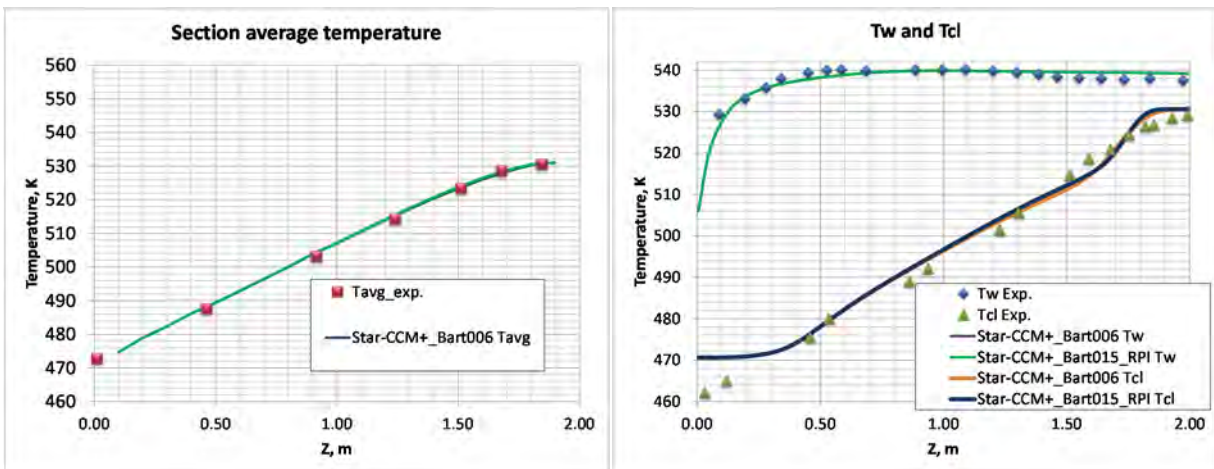

Figure 7: Performance of the new RPI model implemented in STAR-CCM+ and STAR-CCM+ model against the Bartolomei experiment - effect of gas-liquid interface to liquid heat transfer on liquid and wall temperatures.

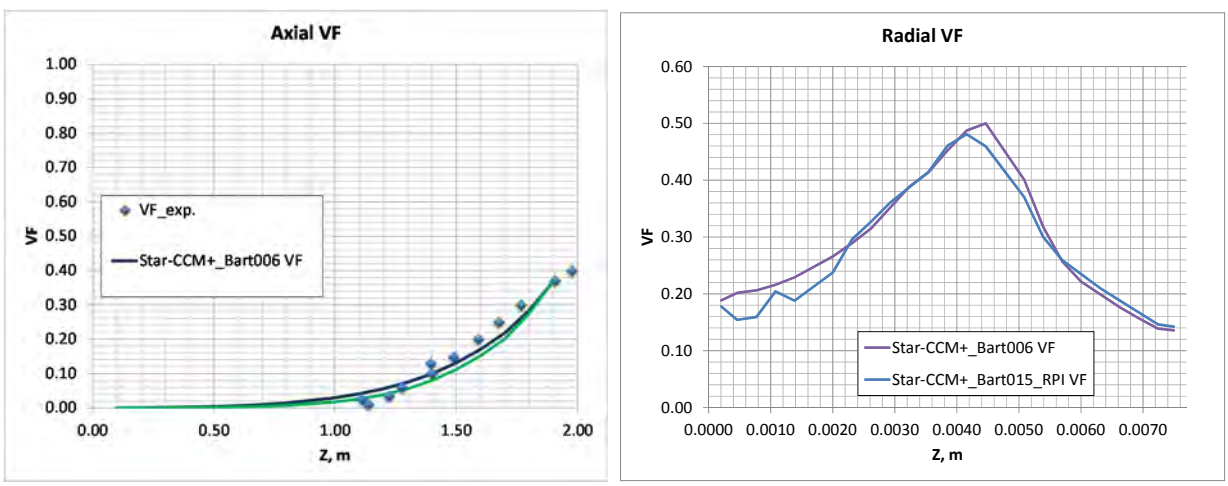

Figure 8: Performance of the new RPI model implemented in STAR-CCM+ and STAR-CCM+ model against the Bartolomei experiment - effect of gas-liquid interface to liquid heat transfer on the void fraction.

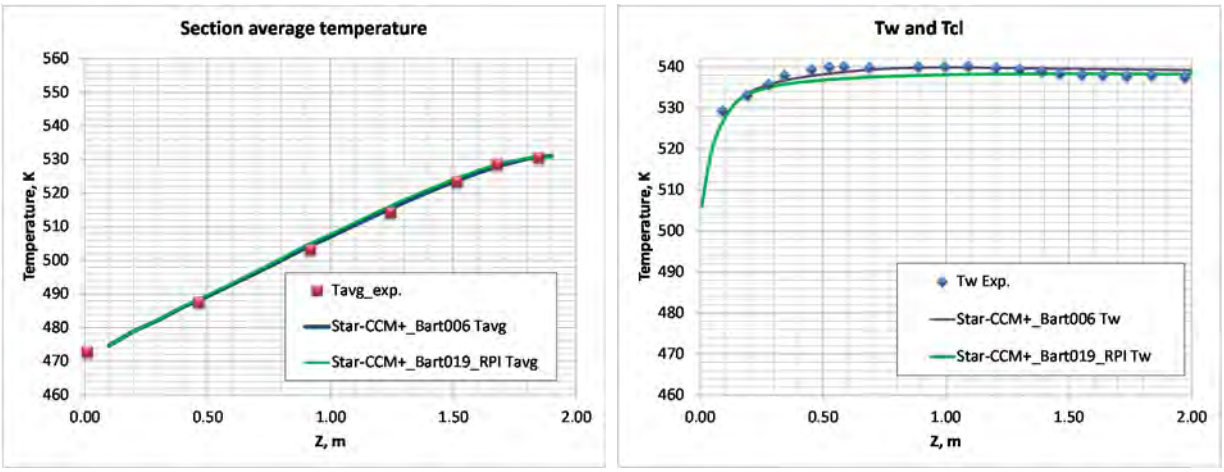

Figure 9: Performance of the new RPI model implemented in STAR-CCM+ and STAR-CCM+ model against the Bartolomei experiment - effect of bubble departure diameter on liquid and wall temperatures.

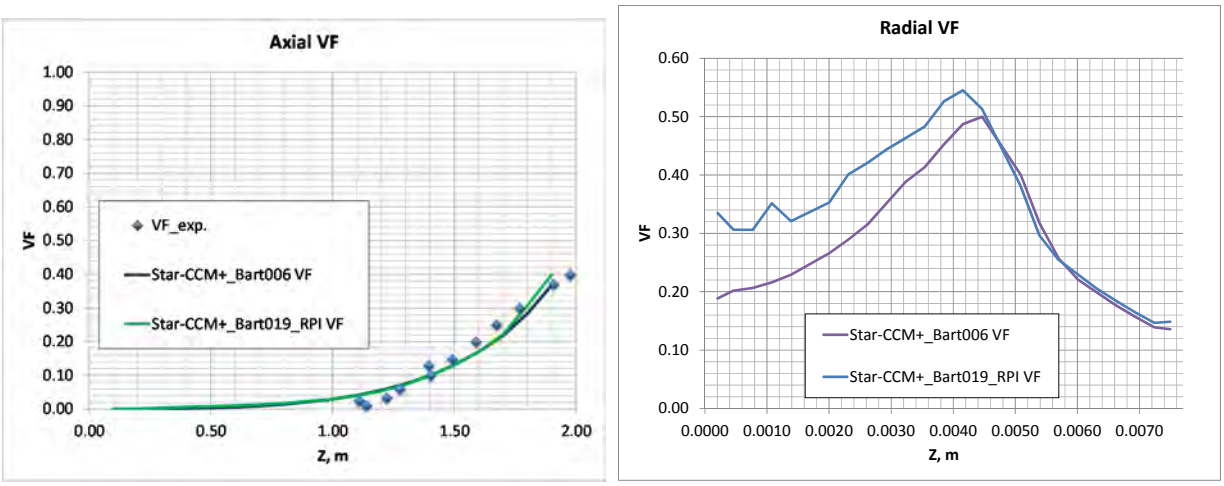

Figure 10: Performance of the new RPI model implemented in STAR-CCM+ and STAR-CCM+ model against the Bartolomei experiment - effect of bubble departure diameter on the void fraction.

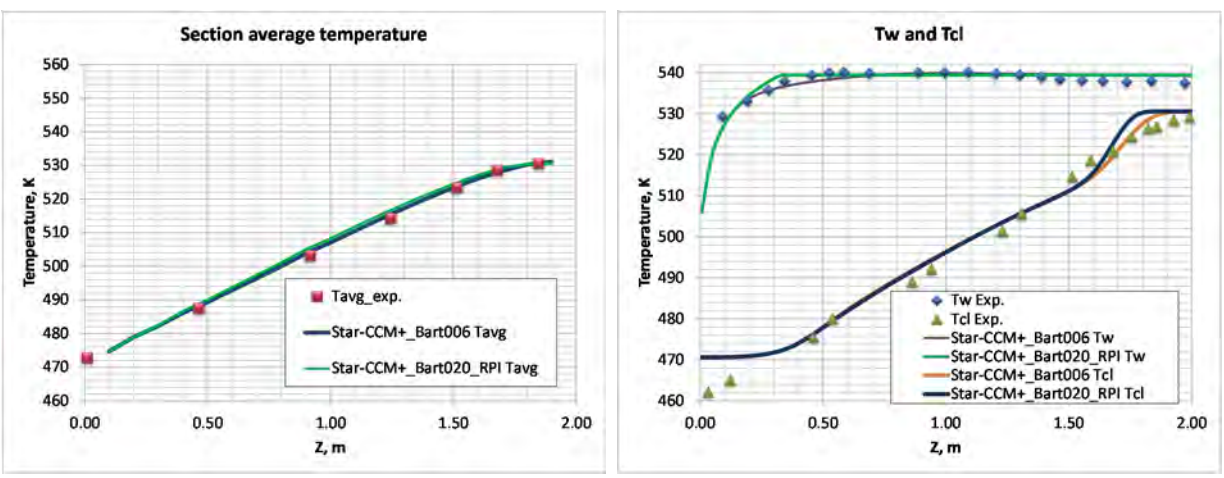

Figure 11: Performance of the new RPI model implemented in STAR-CCM+ and STAR-CCM+ model against the Bartolomei experiment - effect of heat partitioning on liquid and wall temperatures.

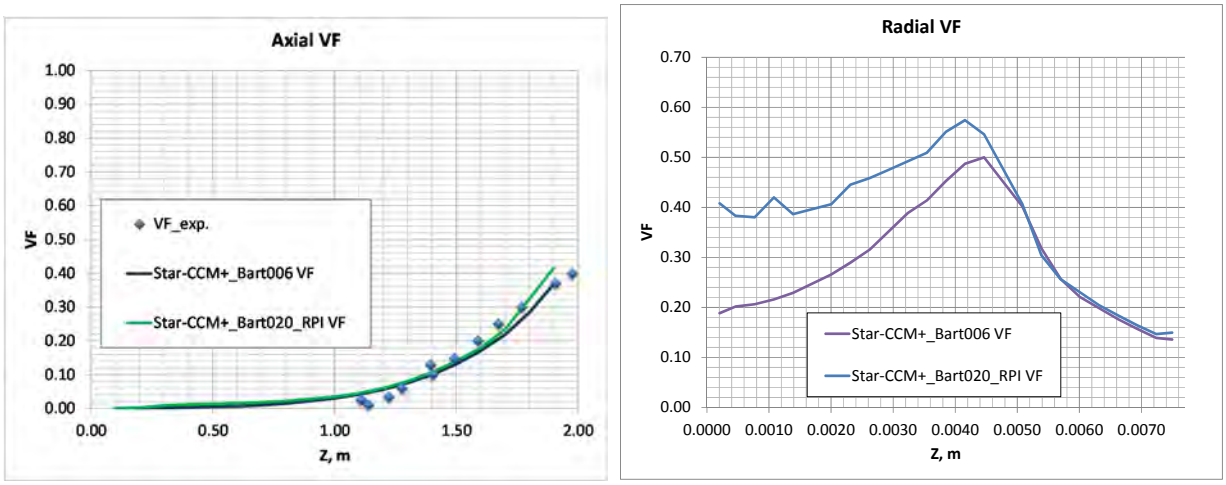

Figure 12: Performance of the new RPI model implemented in STAR-CCM+ and STAR-CCM+ model against the Bartolomei experiment - effect of heat partitioning on the void fraction.

2.5 Conclusions and Future Work

It can be concluded that:

- the model shows a reasonable level of maturity and is ready for implementation in the VERA T/H tools, namely Hydra-TH;
- the evaluation of the model has confirmed the expected sensitivity on model parameters and further improvements are to be expected during the V&V phase;
- the comparison with the STAR-CCM+ reference closure against the Bartolomei experiment presented here and the previous work on PSBT and DEBORA experiments confirm that we have a robust base for the VERA tools;
- the work has clearly been limited to PWR targeted application and there is still work to do to extend it outside of this area;
- last but not of least importance, the comparison of model results against Bartolomei, DEBORA and PSBT experiments have highlighted a serious drawback of the experiments currently available in the open literature. While some experiments (e.g. Bartolomei) provide good data for the wall temperature but lack detailed void-fraction distributions, other experiments (e.g. DEBORA, PSBT) provide detailed void fraction distributions, but no wall temperatures. A sound model validation would require knowledge of both quantities.

3. ADVANCED BOILING CLOSURE

This section is dedicated to describing the work that has been performed in order to support the delivery of an advanced boiling closure. The work has been driven by the new physical understanding derived from the innovative experimental techniques used in the THM research program. The new findings are described first, as they drive the model development and assessment. The new boiling closure formulation is then introduced providing also a graphical exemplification of the modeling ideas.

The status of the momentum closure is also introduced focusing in particular on the innovative work on including wall effects into the formulation. The ITM/DNS methods adopted for deriving the momentum closure parameters are further shown. Finally some preliminary shakedown of the advanced closure is shown and discussed.

3.1 Modeling a New Physical Understanding

To more accurately describe sub-cooled boiling flow in M-CFD, and in order to be able to extend the modeling to critical heat flux, a complete understanding of the complex boiling phenomena and boiling mechanisms needs to be assembled. Flow boiling facilities have been made available to CASL at MIT, TAMU and CCNY for this purpose, where non-intrusive techniques are used to capture new and unique sub-cooled flow boiling data on multiple parameters simultaneously. The data produced by the MIT facility, using water, have been widely used during the model design and to support the derivation of all closure terms. The TAMU data are currently being finalized and will provide a validation database for the model where refrigerant was used to simulate scaled conditions closer to PWR prototypical conditions.

3.1.1 MIT Flow Boiling Facility

The physics of sub-cooled flow boiling of water were investigated at the MIT flow boiling facility using high-speed video (HSV), and infrared (IR) thermography. HSV allowed measurement of the bubble departure diameter, and IR thermography allowed measurement of wall superheat (both the local distribution and the surface-averaged value), heat transfer coefficient, nucleation site density, and bubble departure frequency.

The test section is composed of a quartz rectangular channel with nominal dimensions of 10 mm x 30 mm and a length of 220 mm. The quartz section allows for excellent visualization from various angles for HSV images. The test section has over 6 L/D values of quartz upstream and downstream of the heater recess. On the inlet side the cell is mated with a stainless steel conduit that has the same dimensions as the quartz flow channel and is over 64 L/D long to provide for fully developed flow entering the quartz test section. The quartz section is shown in Figure 13.

The heater cartridge consists of two graphite electrodes and two Macor insulators that are epoxied and bolted together. The heater cartridge is machined to fit, and to sit flush with the inside face of the channel. The small gap between the heater and the cartridge is filled with a hydrophilic sealant to minimize the nucleation sites at the interface. The gap between the heater

cartridge and the flow channel is only heated by conduction, and has a small enough heat flux that nucleation does not occur at this interface. The gap is also sized such that it closes via thermal expansion when the section is at temperature. The sapphire heater is 1-mm thick with filleted edges on the ends, and is coated with an Indium-Tin Oxide (ITO) layer, ~700 nm thick, which is the active heating element. The ITO is laid down by Diamond Coatings on sapphire with scratch dig specifications of 40-20, has a nominal sheet resistance of 2.5 Ω/square, and a nominal composition of 90 wt% In_2O_3 and 10 wt% SnO_2. The ITO acts as the boiling surface and has a static contact angle of 100-110° at room temperature. The ITO layer transmits almost no infrared waves in the 3-5 µm range that the IR camera is sensitive to, while the sapphire transmits almost all of it, so the signal received by the IR camera is that of the surface and can be calibrated to the surface temperature. The ITO wraps around the filleted edges onto the back of the sapphire where 2.5 mm silver pads are laid on top of the ITO to make the electrical connections to the heater. The sapphire heater is epoxied into the heater cartridge flush with the face of the cartridge. The active heater area is 20 mm x 10 mm with the 20-mm direction being in the direction of the flow. Typical bubble size at the conditions of interest is <0.5 mm, so edge effects can be neglected. The channel and heater positioning is shown in Figure 13.

The Phantom V12.1 high speed video (HSV) camera is oriented parallel to the plane of the heater, and with its associated optics is configured to have a spatial resolution of better than 15 µm. 90 degrees from the Phantom camera, and looking at the plane of the heater is the FLIR SC6000 high speed infrared (IR) camera capturing at 1000 Hz and configured to have a spatial resolution of 90 µm. Some tests were also performed with a faster IR Camera IRC806HS configured with a 36 µm spatial resolution and capturing at 1250 Hz. The IR camera images the ITO surface, to measure the 2D temperature distribution on the surface.

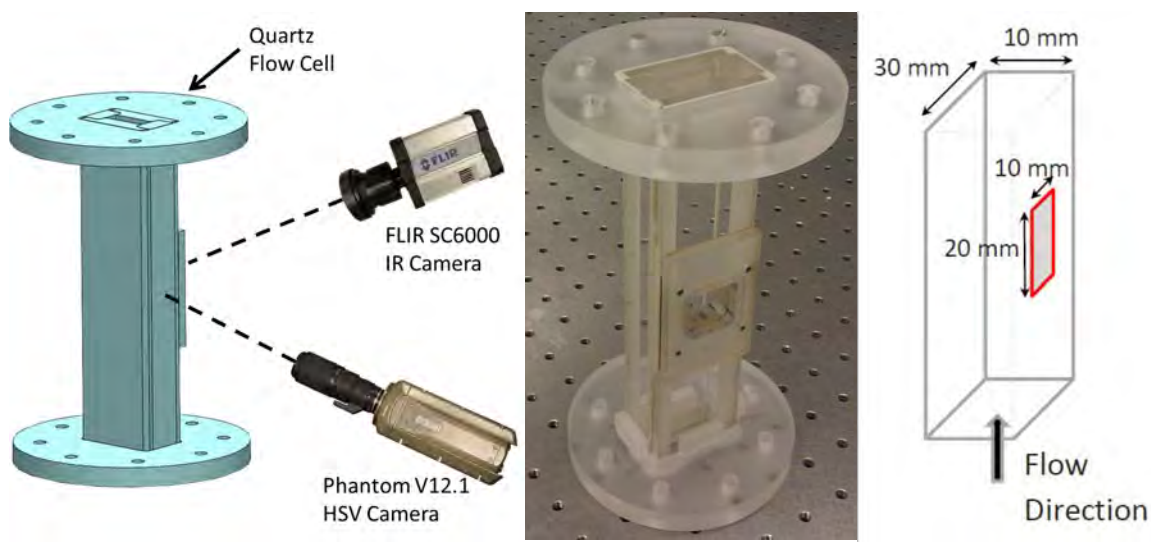

Figure 13: Experimental setup for HSV and IR thermography (left), picture of the quartz section (middle), and diagram of flow channel with the heated area shown in red.

The complete heat flux/mass flux test matrix explored in the MIT study is shown in Table 1; the matrix was repeated for 1.05 and 1.5 bar, and for subcoolings of 5, 10, and 15ºC.

Table 1- Test matrix performed for 1.05 and 1.5 bar, and for subcoolings of 5, 10, and 15ºC.

	Mass Flux (kg/m²/s)					
Heat Flux (kW/m²)	150	250	500	750	100	1250
ONB	x	x	x	x	x	x
100	x	x	x	x	x	x
200	x	x	x	x	x	x
300	x	x	x	x	x	x
400	x	x	x	x	x	x
500	x	x	x	x	x	x
600	x	x	x	x	x	x
700	x	x	x	x	x	x
800	x	x	x	x	x	x
1000	x	x	x	x	x	x
1200	x	x	x	x	x	x
1400			x	x	x	x
1600					x	x

A comparison of the range of conditions of the experiment to those of a PWR is shown Table 2. The Reactor Prototypicality Parameter (RPP) proposed by Dinh [Ref. 11] is used to judge the magnitude of the distortions introduced by the differences between the experiment and the actual application. The RPP is defined for dimensionless quantities and is a simple ratio of their values at PWR conditions and experimental conditions, respectively:

$$RPP = \frac{[SC_{Mod_k}]_{EXP}}{[SC_{Mod_k}]_{APP}}$$

where $[SC_{Mod_k}]_{EXP}$ is the parameter value from the experiment and $[SC_{Mod_k}]_{APP}$ is the parameter value from the application (PWR conditions). If the RPP is within one order of magnitude (a value of 0.1 to 10), the scaling of the experiment is considered adequate. All the parameters scale well except for pressure and density ratio. These are difficult parameters to match experimentally due to the component high cost and complexity associated with operation at PWR pressure (155 bar). High pressures also make visualization of the boiling process a lot more challenging from a practical point of view because of the need for windows capable of withstanding high pressure and temperature, and the small spatial scale of the vapor bubbles at such pressures.

Table 2 - Comparison of potential experiment conditions to PWR conditions and associated RPP.

Parameter	Experiment Range	PWR Range	Typical RPP
Reynolds Number	$0\text{-}1\times10^5$	$2\times10^5\text{-}8\times10^5$	0.20
Prandtl Number	1.1-6.2	0.9-1.2	1.00
Froude Number	0-27	0-217	0.12
Boiling Number	0-10	0-0.25	1.00
Jakob Number	0-100	~20	1.00
Equilibrium Quality at Outlet	-0.24 to 0	-0.38 to 0.10	1.00
Water velocity (m/s)	0-2	2-6	0.20
Mass Flux (kg/m^{2}s)	0-1800	3000-5000	0.25
Temperature (°C)	25-150	286-324	--
Pressure (MPa)	0.1-0.4	15.5	0.03
Subcooling (°C)	0-75	21-58	1.00
Hydraulic Diameter (mm)	15	12	1.33
Wetted Perimeter (mm)	80	30	3.67
Heated Perimeter (mm)	10 or 15	30	0.33
Heat Flux (MW/m^2)	0-2	0.0-1.2	1.00
Channel Area (mm^2)	300	88	5.11
Density Ratio (ρ_f/ρ_g)	440-1620	6	73

3.1.2 A New Look at Flow Boiling

The data extracted from the MIT facility was specifically constructed to support advanced M-CFD model development and it provides a completely new look at the boiling phenomenon. The experimental measurements have provided clarification of shortcomings of current model approaches, and most importantly, are providing fundamental data to suggest new thinking that will ensure a more general and robust representation.

The capability of accurately tracking the local surface temperature at high heat fluxes is key to construction of an accurate physical picture of boiling. An example of the raw data (synchronized HSV and IR images) is shown in Figure 14. The temperature history of the nucleation site circled in red is shown in Figure 15. Four complete ebullition cycles are shown. The time during which the temperature rises represents the wait time, while the surface is heating up after the previous bubble formation. Then the bubble nucleates, grows and departs, which determines the fast drop in temperature, and the cycle repeats.

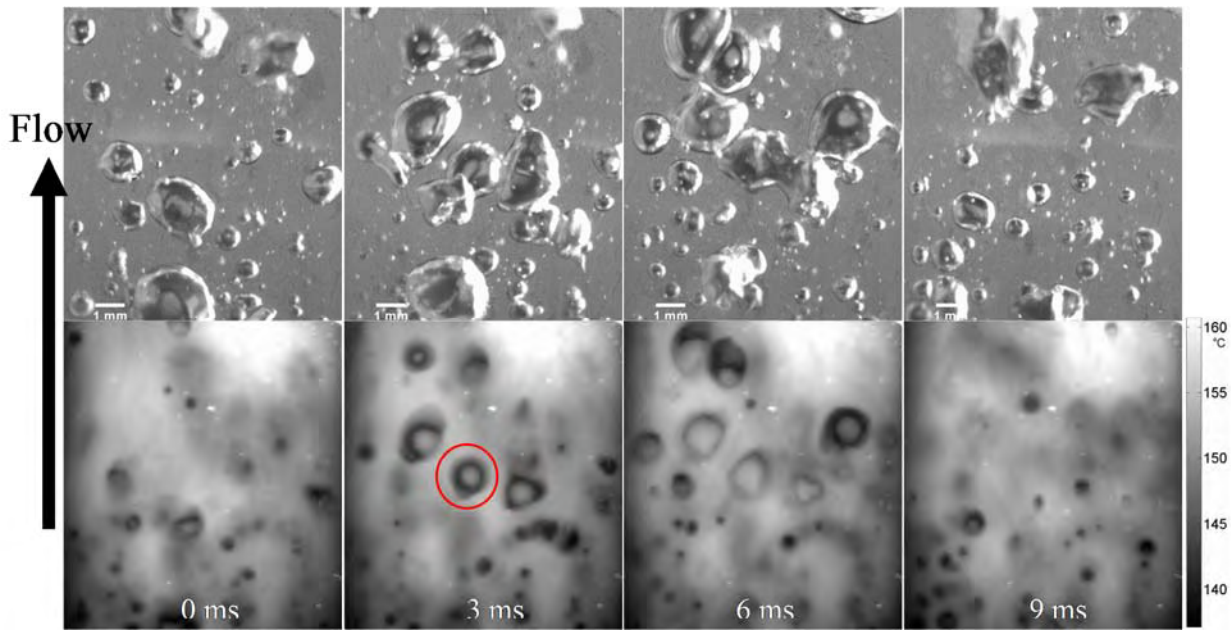

Figure 14: HSV (top) and IR (bottom) images for a high heat flux case. Heat flux: 600 kW/m^2-s, mass flux of 200 kg/m^2-s; subcooling: 9ºC; pressure:1.05 bar.

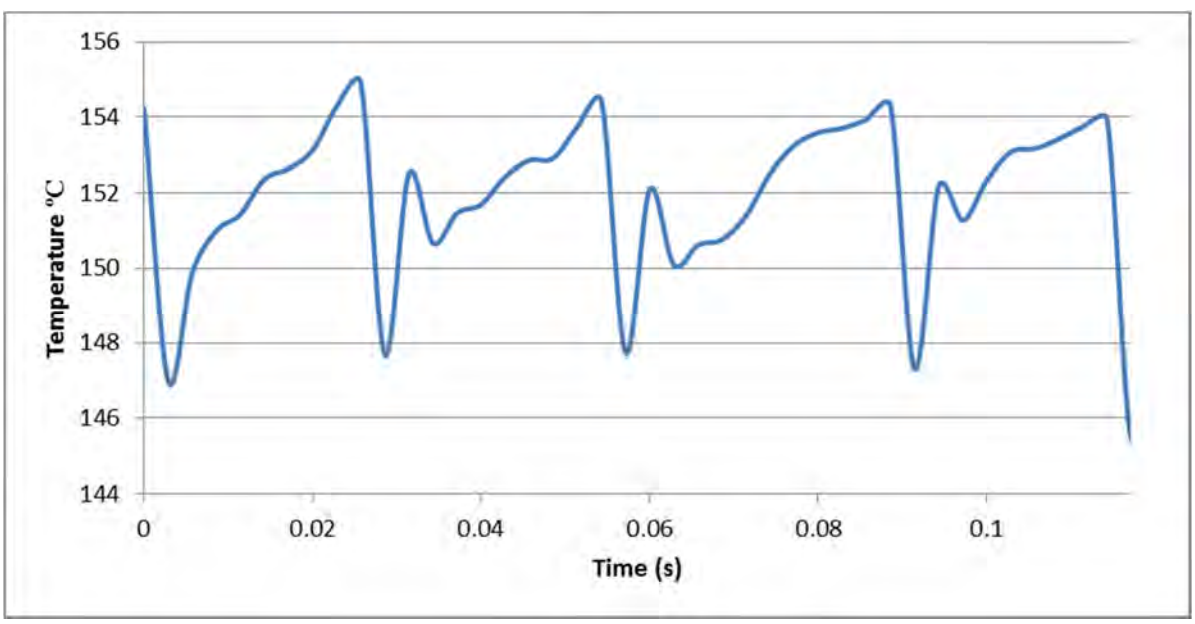

Figure 15: Surface temperature vs. time averaged over a 0.1-mm radius area on heater surface about the nucleation site circled in red in

It is clear from Figure 14 that at high heat fluxes the bubbles interact, thus the traditional RPI heat partitioning model cannot appropriately account for such behavior. A mechanistic representation of wall boiling must therefore include a more faithful representation of the bubble

presence on the wall and how they interact, and this has motivated the development of the new closure, which is discussed in the following section.

Another clear example of the importance of representing the bubble interaction in the model is given by the experimental measurements for sliding bubbles shown in Fig. 16.

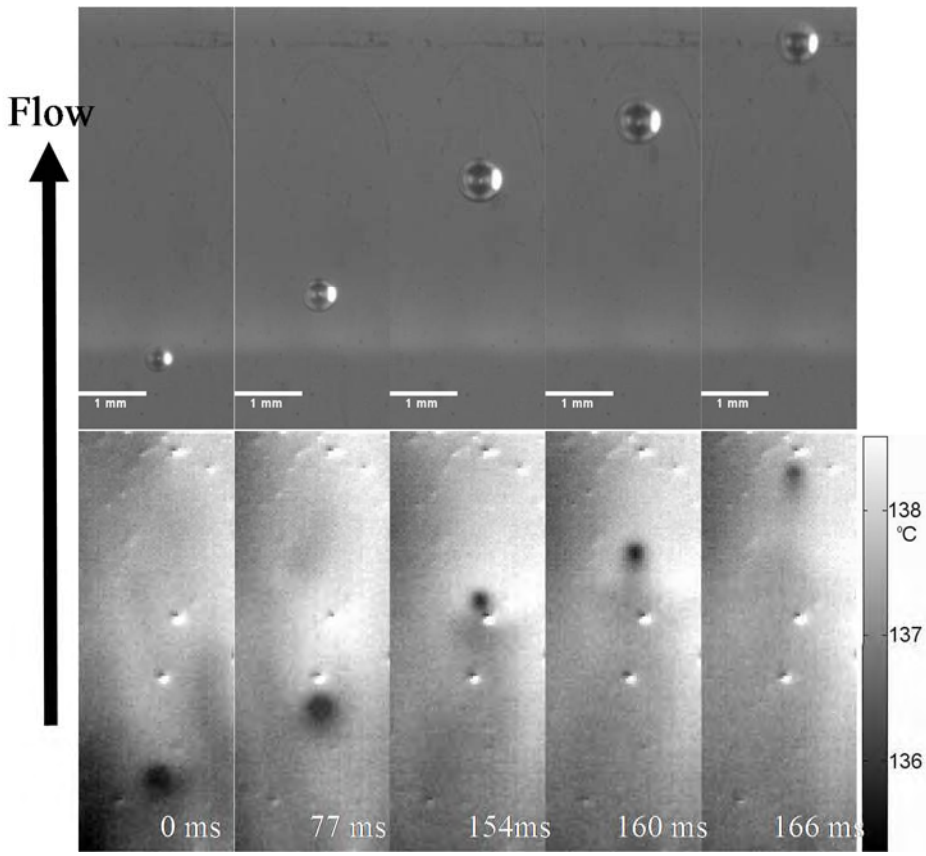

Figure 16: HSV (top) and IR (bottom) of a bubble from the onset of sliding (t=0 ms) to the edge of the frame (t=166 ms). Heat flux: 130 kW/m^2/s; mass flux: 200 kg/m^2/s; subcooling: 10ºC; pressure: 1.05 bar

The cooling underneath a bubble as it slides along the surface was measured for varius conditions as shown in Fig. 17. The cooling is evident and it will undoubtedly influence the activation of nucleation sites in the sliding area. Furthermore it constitutes a further contribution to heat removal, which is usually not accounted for in mechanistic models.

It is evident from the discussed example that the experimental findings have strongly driven the conceptual work on the mechanistic modeling discussed in the next section. Further the experiments have provided an extensive database that is being used to calibrate the model parameters where necessary. The complete set of data is available in the CASL repositories. Here we only provide a meaningful sample of the quantities of interest that have been measured.

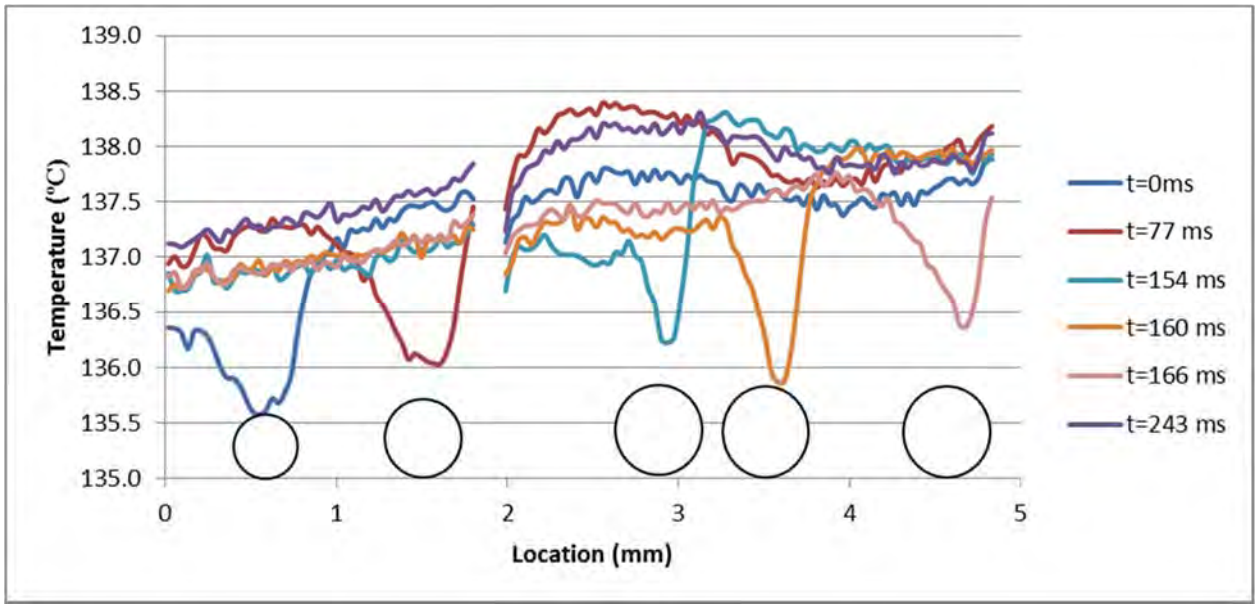

Figure 17: Temperature profile along the sliding bubble path at various time steps. t=0 is the onset of bubble sliding. The circles on the plot show the approximate position of the bubble at each time step. (The measurement uncertainty on temperature is ± 2.0°C; error bars not shown) Heat flux: 130 kW/m^2/s; mass flux: 200 kg/m^2/s; subcooling: 10ºC; pressure: 1.05 bar

Figures 18 shows a representative example of the bubble departure diameter data extracted from the MIT facility. As mentioned in the introduction the diameter of the departing bubbles during the ebullition cycle is a fundamental quantity in predicting the evaporative heat flux. Access to controlled and accurate measurements of this quantity is therefore fundamental and, as shown in the following sections, allows extending the model capabilities and supports the construction of more mechanistic closures.

The bubble departure diameter was measured in the test using HSV, the spatial resolution was 15 µm per pixel and an area of 1280x800 pixels was imaged at a rate of 1000-5000 Hz, as appropriate for the flow conditions, and a multiple of the IR camera acquisition frequency, so that the two cameras could be synchronized. The bubble departure diameter is defined here as the diameter of the bubble at the time of lift-off (detachment perpendicular to the wall) or slide (detachment parallel to the wall), whichever comes first. The diameter was only measured for flow regimes in which individual bubbles could be identified and were not greatly influenced by other bubbles during their growth (i.e. no bubble coalescence on the surface, and no bubbles passing a departing bubble). The bubbles were measured at the location of the onset of boiling on the heater surface.

The distribution of the bubble departure diameters was much larger than the measurement uncertainty of 15 µm, and the error bars on the plot in Fig. 19 represent the standard deviation of the distribution. Klausner's force-balance model [12] modified by Sugrue et al. [13] is shown as a comparison. This model tracks with the data very well, although it tends to slightly under predict the departure diameter at high mass fluxes. The data shows increasing departure diameters with increasing heat flux, decreasing mass flux, and decreasing subcooling as expected. These same trends were observed by Sugrue et al. [14].

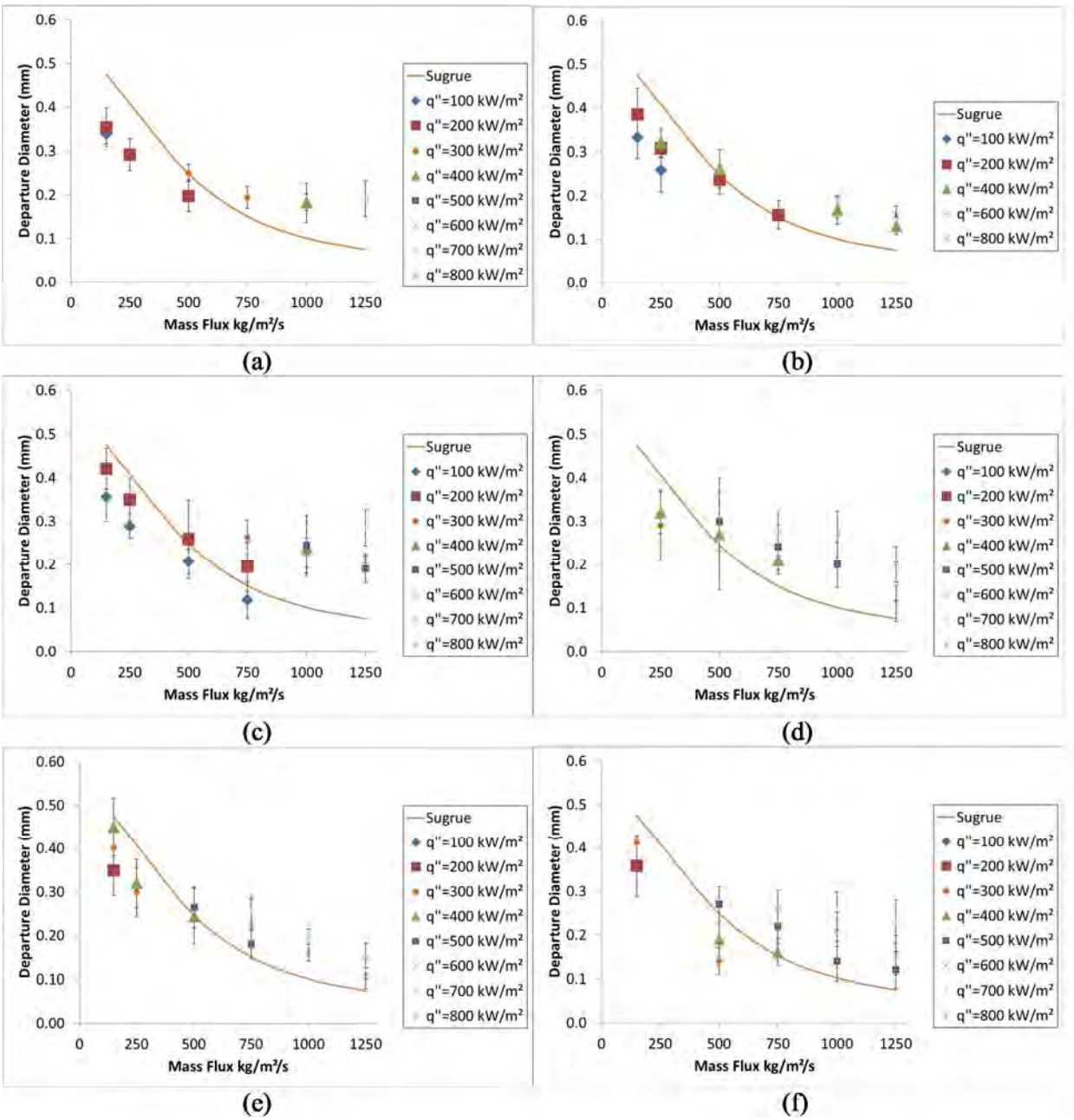

Figure 18: Bubble departure diameters vs. mass flux for 1.05 bar and 15ºC subcooling (a), 10°C subcooling (b), 5ºC subcooling (c). Bubble departure diameters vs. mass flux for 1.5 bar and 15ºC subcooling (d), 10°C subcooling (e), 5ºC subcooling (f).

Another fundamental quantity is the bubble frequency, which is determined from the bubble ebullition cycle. The cycle comprises the bubble growth time and wait time. The growth time is the time from bubble nucleation to bubble detachment from the surface. The wait time is defined as the time between bubble departure and nucleation of the next bubble. Effectively, it is a measure of the time required to reconstruct the thermal boundary layer following bubble

departure. Adding the growth and wait times together yields the bubble period, which is the inverse of the departure frequency. In the advanced closure formulation it is desirable to introduce a mechanistic representation of the departure cycle and the experimental findings provide a useful support to the model construction.

In the tests, the bubble departure period was determined from the IR thermography images, as a bubble nucleation is marked by a sharp drop in the wall temperature, while the wall temperature starts to rise again at bubble detachment. The temporal resolution of the IR images was between 0.8 and 1.0 ms. The bubble period was measured by using an automated routine that takes the sites identified by the nucleation site density routine, and then checks each site for the time between nucleation events. The distribution of the bubble period was much larger than the measurement uncertainty so the error bars represent the standard distribution of the sample. An example distribution is shown in Figure 19. The bubble periods are compared to a correlation by Basu [15], which is shown in the equation:

$$t_w = 139.1\left(\Delta T_w^{-4.1}\right) \;;\; \frac{D_d^2}{\alpha_l Ja_{\sup}} = 45\exp\left(-0.02 Ja_{sub}\right) \qquad 3.1$$

The wait time correlation is only dependent on the average wall superheat and assumes that there is no effect of subcooling, heat flux, heat transfer coefficient and heater thermal diffusivity, which are expected to be important. The growth time is dependent on D_d, the bubble departure diameter, α_l the liquid thermal diffusivity, $Ja_{\sup}$ and Ja_{sub}, the Jakob number based on the wall superheat and the subcooling respectively. Not surprisingly, the correlation cannot predict the experimental values accurately. The bubble periods are shown in Figure 20 for the various conditions. The period decreases with wall superheat as expected.

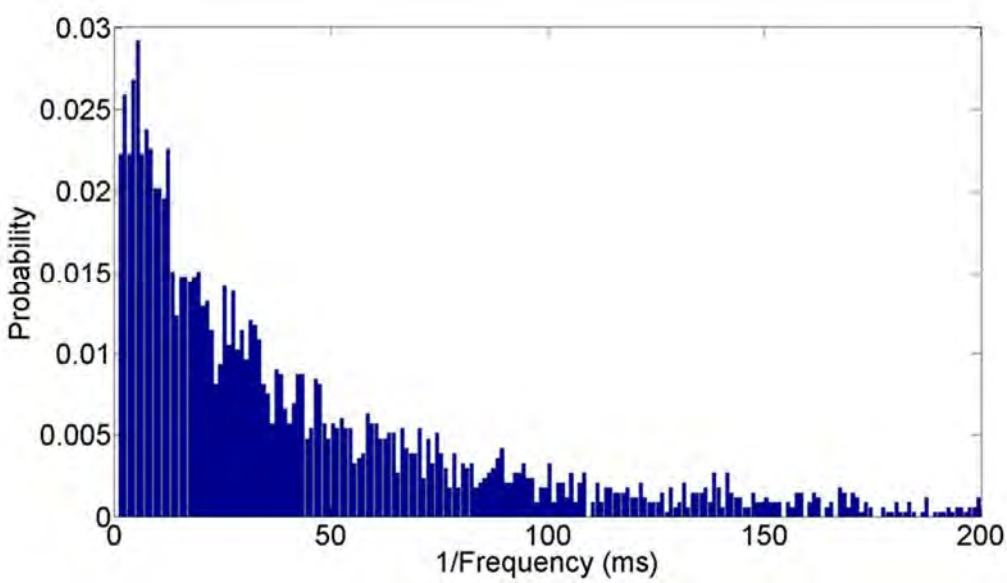

Figure 19: Example distribution of bubble periods.

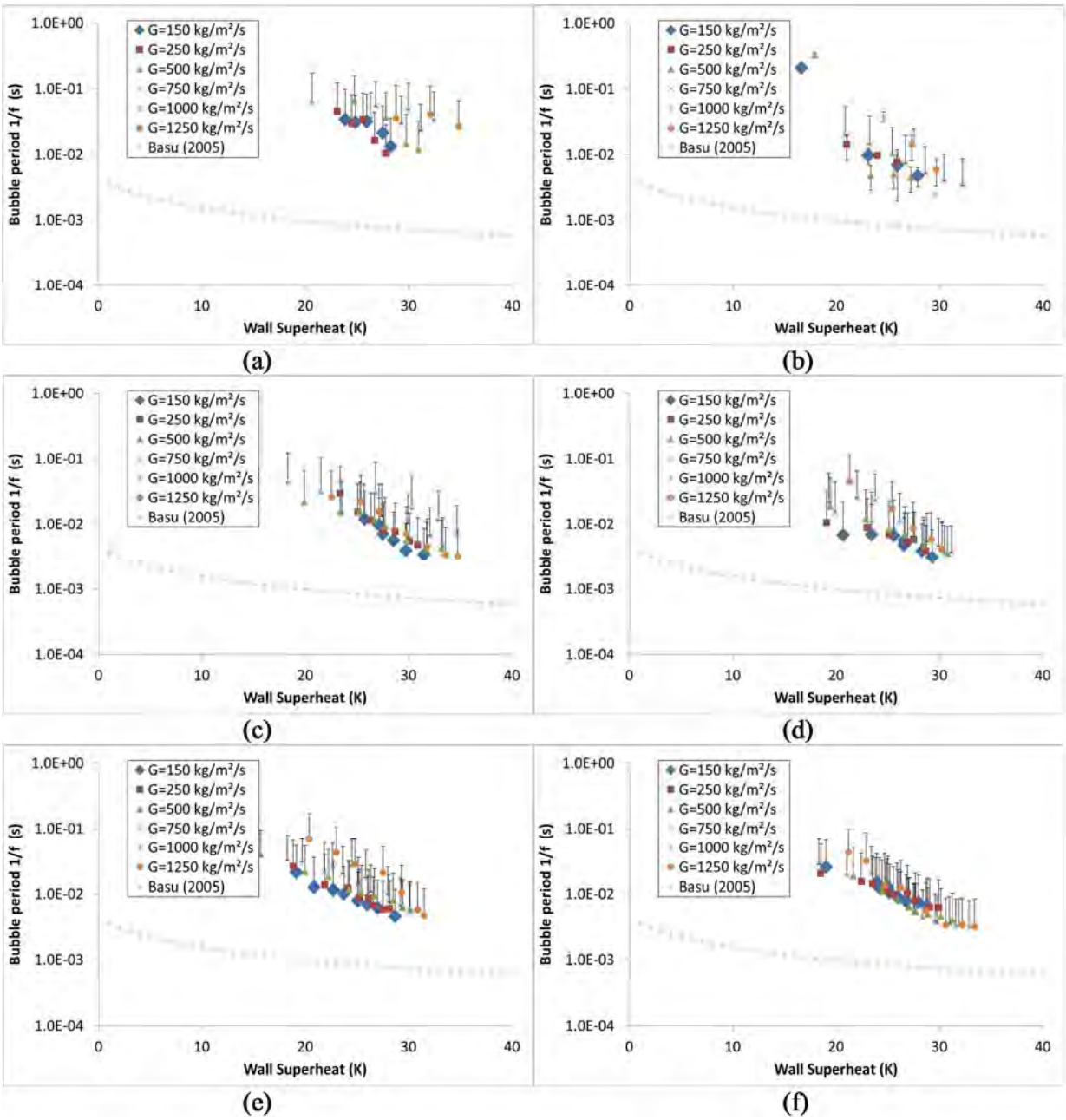

Figure 20: Bubble period vs. wall superheat for 1.05 bar and 15ºC subcooling (a), 10°C subcooling (b), 5ºC subcooling (c). Bubble period vs. wall superheat for 1.5 bar and 15ºC subcooling (d), 10°C subcooling (e), 5ºC subcooling (f).

.

3.2 Advanced Boiling Closure Formulation

3.2.1 GEN-I Heat Partitioning Limitations

As previously mentioned the new boiling closure leverages the understanding from the experiments in order to introduce a more mechanistic description of the wall boiling phenomena. The fundamental target of this work has been to introduce all necessary mechanisms to accurately predict the temperature and heat flux for sub-cooled flow boiling at the wall in CFD simulations. The improved closure not only aims at better representing onset of boiling and heat transfer predictions but particularly targets the capability of extending the modeling up to DNB predictions.

The classic heat partitioning concept introduced by Judd and Hwang (1976) and adapted by Kurul and Podowski (1990) introduces a simple approach:

$$q''_{tot} = q''_{fc} + q''_{q} + q''_{e} \qquad 3.2$$

Here the total heat flux (q''_{tot}) is partitioned into convection (q''_{fc}), quenching (q''_{q}), which captures the heat expended in the re-formation of the disrupted thermal boundary from bubble departure, and the latent heat of evaporation (q''_{e}) components. While the model has shown great flexibility and has been selected for the GEN-I delivery, it is clear that it is desirable to move towards a more physically based closure which could provide much wider generality and reduce the need for calibration.

In summary, some of the fundamental physical characteristics of boiling are not captured in the classic partitioning approach, and this can strongly limit the applicability and generality of the approach. Here we briefly discuss some of the limitations, which motivated the derivation of newer approach, while not fully comprehensive the discussion provides the key points and should allow appreciating the new model characteristics, which will be discussed next:

- The movement of bubbles on the heater surface prior to lift-off is not captured in this heat partitioning approach by Kurul and Podowski (1990) since it does not consider the effects of sliding bubbles along the wall [18] which has been shown to occur in sub-cooled flow boiling through experiments [19], [20]. In sub-cooled boiling, bubbles often slide along the heated wall after detaching from the nucleation site and before lifting off into the bulk of the liquid flow. These sliding bubbles can also merge and coalesce with other detached and nucleating bubbles downstream. The tendency for bubble sliding is high in sub-cooled flow boiling and as a result, efforts have been made to incorporate the transient conduction of sliding bubbles in the heat partitioning model [16], [18].
- Prior to the Onset of Significant Void (OSV) bubbles form and remain attached to the heated surface due to the flow conditions that form the thermal boundary. This prevents bubbles from reaching the bubble departure diameter and therefore they remain attached to the heater. Experiments have shown that the initial bubble growth

is rapid and condensation occurs at the top of the bubble. The evaporation term in the classic partitioning model, being based on the departure of bubbles does not predict any heat transfer enhancement. In brief the region before OSV is not represented in the GEN-I closure approach.

- The bubble departure mechanics of the GEN-I does not take into consideration the interaction of bubbles and nucleation sites and therefore will always overpredict the number of nucleation sites. In practice this is often remedied by the use of limiters in the nucleation site densities, but this requires recalibration of the model and does not provide generality and capability of modelling intermediate regimes or varying flow conditions.

3.2.2 GEN-II Heat Partitioning Model

This section describes the newly derived heat partitioning model. The ultimate focus of this work has been to introduce all necessary mechanisms to accurately predict the temperature and heat flux for sub-cooled flow boiling at the wall in CFD simulations. In order to help the understanding of the heat transfer mechanisms graphical representation are provided for each of the model components.

In order to include all necessary mechanisms, the total heat flux (q''_{tot}) is partitioned into 4 separate components:

$$q''_{tot} = q''_{fc} + q''_{e} + q''_{q} + q''_{sc} \qquad 3.3$$

where the four terms represent:

(1) Forced convection
(2) Evaporation
(3) Quenching
(4) Sliding conduction

as shown below in Figure 21.

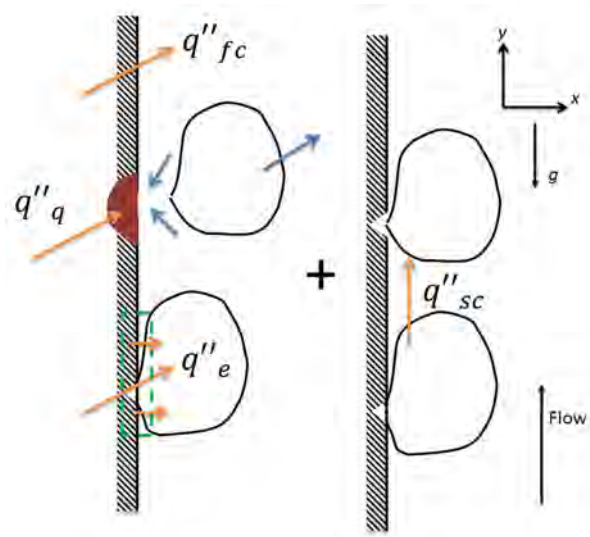

Figure 21: Depiction of the heat flux partitioning for sub-cooled flow boiling.

The addition of the sliding conduction term accounts for the increased heat transfer due to bubbles that slide along the heater wall before lift-off. This is largely due to the transient conduction that occurs from the disrupted thermal boundary layer. These four modes of heat transfer are discussed in detail in the following sections.

Forced Convection Heat Flux

This is calculated using the traditional method of single-phase forced convection on a heated surface. It differs from the base case model in that it also accounts for the addition of increased heat transfer due to the presence of bubbles. This is captured by increasing the surface roughness due to the bubbles on the heater and is done so by modifying the wall function for turbulent flows. The enhanced heat transfer is a function of the size and distribution of bubbles on the heater surface.

For a hydraulically smooth wall, the velocity profile near the wall is given by Eq. 3.4 for high-Reynolds number flows. The empirical coefficient (E) is usually set equal to 9.0 and is a constant from the rearrangement of the classic Eq. 3.5 to give $E = e^{KB}$, where K is the Von Karman constant. The definitions of the remaining variables are listed in Table 3.

$$u^+ = y^+ \qquad when\ y^+ \leq y_m^+ \tag{3.4}$$

$$u^+ = \frac{1}{K}\ln(Ey^+) \quad when\ y^+ > y_m^+$$

$$u^+ = \frac{1}{\kappa}\ln(y^+) + B \tag{3.5}$$

Table 3. Definition of variables used in the smooth wall function.

Variable	Definition
$\boldsymbol{u^+}$	$\frac{u}{u_\tau}$
$\boldsymbol{u_\tau}$	$\left(\frac{\tau_w}{\rho}\right)^{1/2}$
$\boldsymbol{y^+}$	$\frac{\rho u_\tau y}{\mu}$

To account for the added roughness caused by the bubbles on the heater wall, the rough wall model is employed. This model modifies the log-law coefficient E to make it a function of a roughness parameter given by R^+. This is shown in 3.6, where r is the equivalent sand-grain roughness height. The value for E is then modified by the roughness function, f, such that $E' = {}^{E}/_{f}$ which is placed in the classic equation for the velocity profile (3.4). The roughness function is dependent on the value of roughness and is shown in Eq. 3.7.

$$R^+ = \frac{r u_\tau \rho}{\mu} \tag{3.6}$$

$$f = 1 \qquad when\ R^+ \leq R^+_{smooth} \tag{3.7}$$

$$f = \left[B \left(\frac{R^+ - R^+_{smooth}}{R^+_{rough} - R^+_{smooth}} \right) + CR^+ \right]^a \qquad when\ R^+_{smooth} < R^+ < R^+_{rough}$$

$$f = B + CR^+ \qquad when\ R^+ > R^+_{rough}$$

In the intermediate range of wall roughness, where $R^+_{smooth} < R^+ < R^+_{rough}$, a is given by Eq. 3.8. Typically, the values for R^+_{smooth}, R^+_{rough}, $B, and\ C$ are 2.25, 90, 0, and 0.253 respectively [74].

$$a = \sin\left[\frac{\pi}{2} \frac{log\left({R^+}/{R^+_{smooth}} \right)}{log\left({R^+_{rough}}/{R^+_{smooth}} \right)} \right] \tag{3.8}$$

To be able to predict the added roughness due to the bubbles, the equivalent sand roughness is estimated and is dependent on both the size and distribution of bubbles on the heater surface. If the bubble sizes are extremely small and lie only in the purely viscous sublayer, when $R^+ \leq R^+_{smooth}$, the wall is treated as a smooth surface because it has no effect on the flow. If the bubbles project further into the flow, when $R^+ > R^+_{rough}$, then it can be treated as fully rough. Since experimental data are not available to back-calculate the equivalent sand-grain roughness from pressure drop data as is done traditionally [75], the value is estimated by calculating an average surface roughness due to the bubbles. This is shown in Eq. 3.9 where n is the number of measurements and y_i is the height for each measurement.

$$R_a = \frac{1}{n} \sum_{i=1}^{n} |y_i| \tag{3.9}$$

The surface of the heater is assumed to be completely smooth except for the area taken up by a bubble. Therefore, everywhere where a bubble is not present, the roughness height is zero. A unit cell is used to calculate the average surface roughness. The distance between bubbles is assumed constant and bubbles are distributed in a square lattice so that the bubble spacing is given by $s = \frac{1}{\sqrt{N''}}$. The average surface roughness is then calculated using an integral form of Eq. 3.9 and is shown in Eq. 3.10 where $A_{cell} = s^2 = {1}/{N''}$ and V_{tot} is the volume taken up by the bubble and is dependent on its size and shape. For spherical bubbles, the total volume is calculated by assuming the roughness height is taken at the highest point of the bubble and is shown in Eq. 3.11.

$$R_a = \frac{V_{tot}}{A_{cell}} \qquad 3.10$$

$$V_{tot} = {}^{4}/_{3}\,\pi r_b^3 \tfrac{1}{2} + \pi r_b^3 = \tfrac{5}{3}\pi r_b^3 \qquad 3.11$$

An example to illustrate the effectiveness of this method was completed by implementing the results from the ITM-1 study [22]. In this study, the effect of bubbles attached to a wall on both the near-wall turbulence and the friction factor were investigated using the code TransAT. Both Direct Numerical Simulation (DNS) and Large Eddy Simulation (LES) approaches were used to resolve the flow. The computational domain was a Cartesian box of dimensions $L_x = 2\pi h$, $L_y = 2h$, and $L_z = \pi h$ and shown in Figure 22, where h is the half-height of the channel and used as the characteristic length scale. The flow is in the +x direction and the domain has periodic boundary conditions in the streamwise (x) and spanwise (z) directions. There is a no-slip boundary at the wall (y). The bubbles were modeled as hemispherical solid obstacles of height k (equivalent to $y+ = 10$) on the walls of the simulation domain. They are spaced at a distance S_b equivalent to $y+ = 40$ and arranged on a square lattice. The simulation was completed using an imposed shear Reynolds number (Re_τ) of 400, a fixed density (ρ) of $1 kg/m^3$, and viscosity (μ) of Re_τ^{-1}.

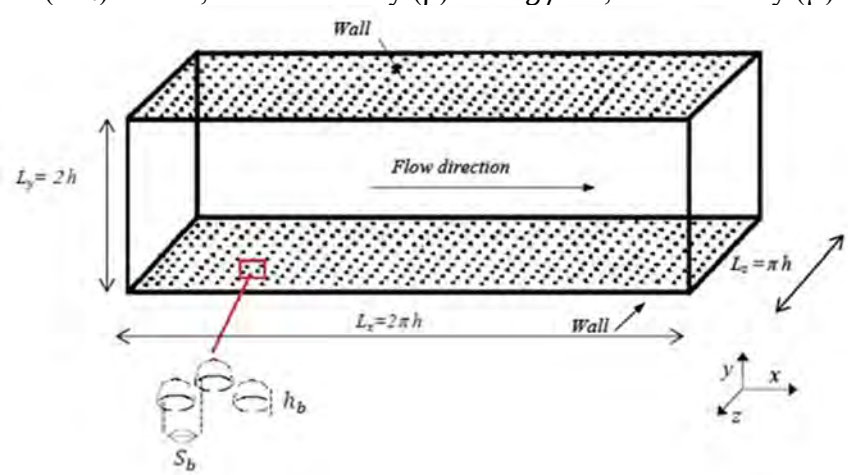

Figure 22: ITM Test Case 1 computational domain and illustration of the hemispherical obstacles [31].

The average surface roughness was calculated using the integral described previously. In this test case, the bubbles were modeled as hemispheres, so the $V_{tot} = {}^{2}/_{3}\,\pi r_b^3$. This provided $R_a = 0.00327m$. The rough wall model was implemented in STAR-CCM+ with an equivalent sand grain roughness value given by the average surface roughness value calculated. This is compared to the DNS data for a smooth wall case and the hemispherical case to illustrate the ability of this method to capture the roughness effects on the velocity profile of the flow and is shown in Figure 23. This is important for forced convective heat transfer because the temperature profile is then obtained from this velocity profile.

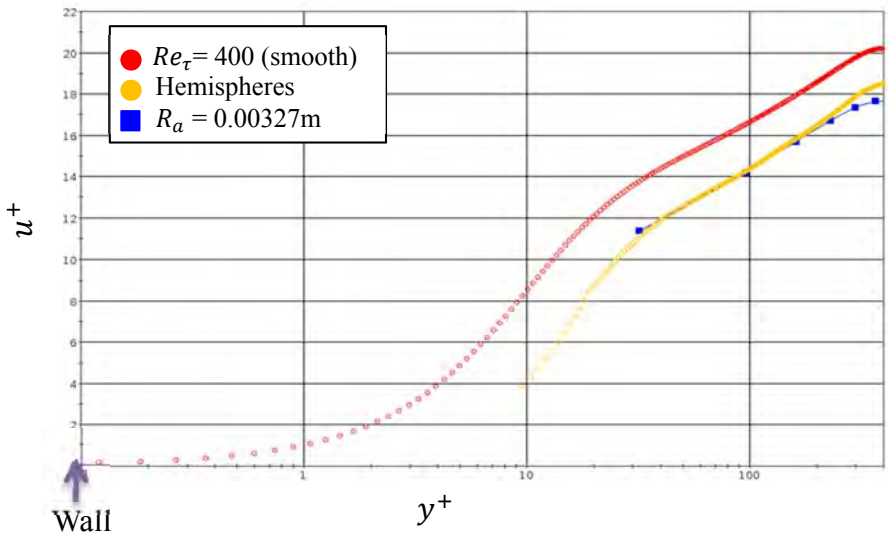

Figure 23: Velocity profile near the wall for a smooth surface and a surface with hemispherical obstacles.

The single-phase forced convection component is employed on all areas of the heater that is not under bubble influence. The calculation for the forced convection component is given by Eq. 3.12, where h_{fc} is the heat transfer coefficient that incorporates the increased heat transfer due to the presence of bubbles when wall boiling occurs.

$$q''_{fc} = h_{fc}(\Delta T_w + \Delta T_{sub}) \qquad 3.12$$

Evaporation Heat Flux

The evaporation term is calculated using the physical phenomena of the rapid initial bubble growth and the microlayer evaporation and is shown in Eq. 3.13. The initial bubble growth is calculated as shown in Eq. 3.14.The microlayer is a thin layer of liquid that becomes trapped between a quickly growing bubble and the superheated wall and is illustrated in Figure 24. The evaporation of the microlayer of liquid between the bubble and the wall has been studied through experiments using interferometry and high-speed cinematography [32], [33], [34]. These have illustrated that microlayer evaporation plays a significant role even in low subcooling conditions.

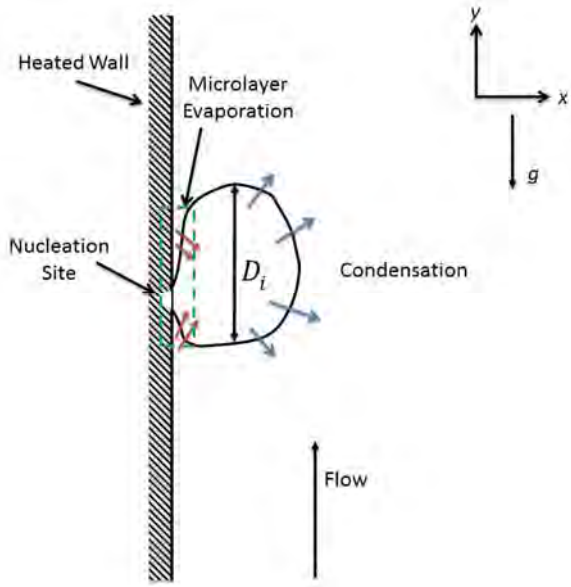

Figure 24: Illustration of microlayer evaporation and condensation on a bubble attached to a heated wall.

$$q''_e = q''_{e,init} + q''_{e,mL} \tag{3.13}$$

$$q''_{e,init} = V_{b,final}\rho_v h_{fg} f \mathrm{N}'' \tag{3.14}$$

The volume of the microlayer is illustrated in Figure 25 and is calculated by assuming the microlayer has a maximum thickness (δ_{max}) that decreases to zero at the center of the bubble. It is assumed that the entire microlayer evaporates for each bubble and is given in Eqs. 3.15 and 3.16. The value used for the radius of the microlayer is half the radius of the bubble and $\delta_{max} = 2\mu m$.

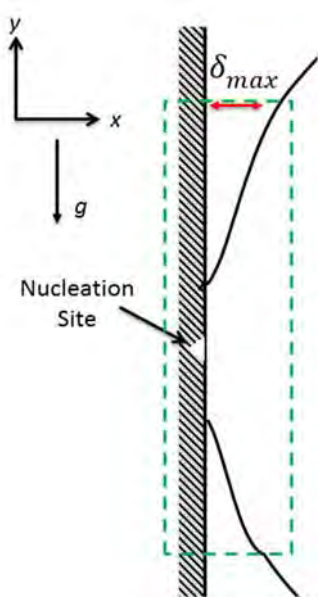

Figure 25: Depiction of the microlayer with the maximum thickness shown.

$$q''_{e,mL} = V_{mL}\rho_f h_{fg} f N'' \tag{3.15}$$

$$V_{mL} = \frac{2}{3}\pi\left(\frac{R}{2}\right)^2 \delta_{max} \tag{3.16}$$

Literature sources vary on the reported size of the influence area factor [16], [17] which consequently affects the number of bubbles that can fit on the heater surface. With changing operating conditions, preliminary experimental data shows that the influence area of the bubble stays relatively constant so the value is currently set as $F_A = 2$ [76]. The area of influence term takes into account that the bubble on the heater surface affects an area larger than the physical area of the bubble. It must also account for "crowding," which is when the number of bubbles on the heater surface begin to affect each other [77]. Since the current active nucleation site density models are highly dependent on the wall superheat and consequently can reach unrealistic values, a maximum value is enforced that is determined on the physical number of bubbles that can fit on the heater surface. On average, this maximum number is depicted in Figure 26 along with a magnified view showing the dry area, microlayer area, and the area of influence for a single bubble. Through this depiction, the effective area of a single bubble is calculated as is shown in Eq. 3.17, where D_m is the maximum bubble size reached before the bubble departs from the nucleation site.

$$a_{b,eff} = F_A \pi \left(\frac{D_m}{2}\right)^2 \tag{3.17}$$

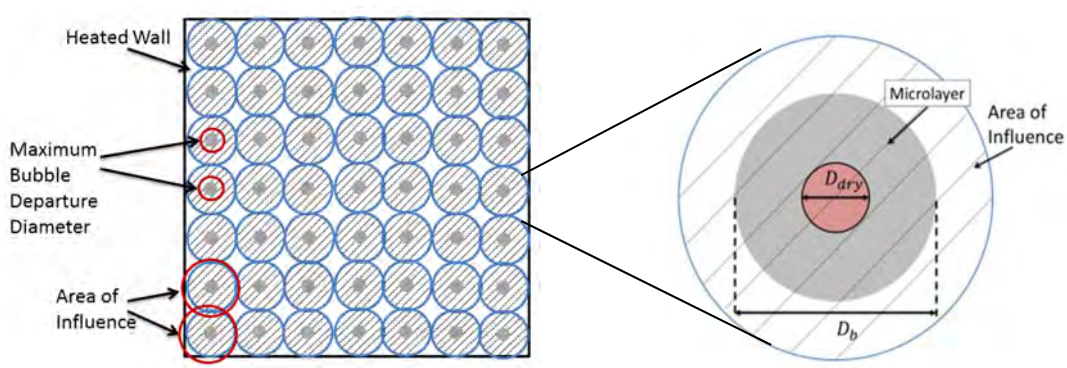

Figure 26: Illustration of the maximum number of active nucleation sites on a heated surface with a magnified view to show the dry area, microlayer area, and the area of influence for a single bubble.

The effective area of the bubbles is used to suppress the drastic increase in active nucleation site density at high wall superheat to prevent unphysical values. Current model implementation is depicted in Figure 27 where the maximum active nucleation site density is given by Eq. 3.18.

$$N''_{max} = \frac{1}{a_{b,eff}} \tag{3.18}$$

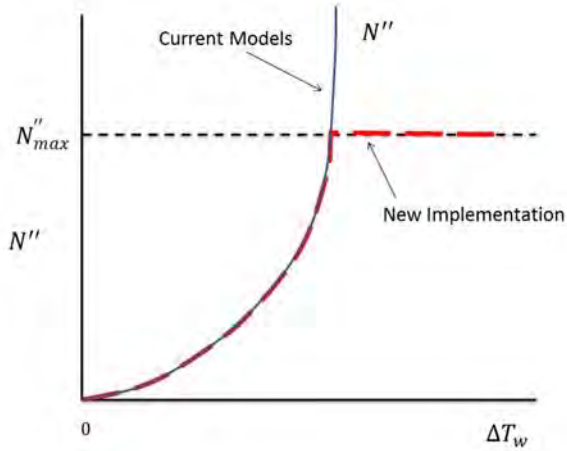

Figure 27: Illustration of the implementation of the maximum active nucleation site density.

Sliding Conduction

As experiments have illustrated, the effect of sliding bubbles on the heat transfer coefficient for sub-cooled flow boiling can be very high, even the dominant mode of heat transfer for particular flow regimes.

A mechanistic force balance model is used to predict when a bubble will begin to slide along the heated wall, in the same fashion as it is currently used to predict when the bubble will lift-off the surface. The original concept was proposed for both pool and flow boiling by Klausner et al. [12] and Zeng et al. [21] and it was recently adapted and modified by Yun et al. [23] for CFD application.

The bubble departure diameter, or bubble movement diameter (D_m), is defined as the diameter of the bubble when it moves from its inception point, or point of origin. This diameter is predicted by the force balance model developed by Sugrue et al. [13], which is a modified version of the recent work by Yun et al. At this size, the bubble may slide along the heater surface and lift-off when it reaches the lift-off diameter size (D_l). The lift-off diameter is also predicted by a force-balance model developed by Situ et al [24] and is illustrated in Figure 28. If the prediction of D_l is smaller thanD_m, then the bubble lifts off into the fluid flow without sliding.

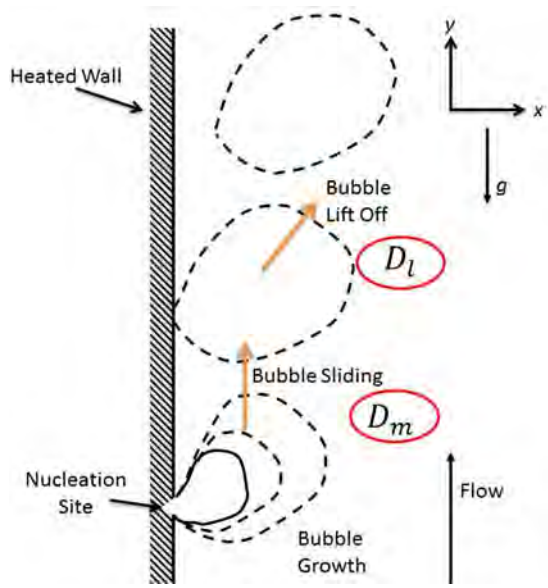

Figure 28: Illustration of bubble growth at a nucleation site until it departs from the site and slides and lifts-off the heater surface.

Bubble sliding increases heat transfer because of the disruption of the thermal boundary layer inducing transient conduction as the cold liquid comes in contact with the wall. This is modelled using the error function solution to the transient temperature profile for a 1-D transient heat conduction into a semi-infinite medium using the heater surface temperature as T_w and the liquid temperature as T_l and the wall heat flux is shown in Eq. 3.19. When the boundary layer is disrupted by a sliding bubble, the sliding conduction heat transfer mode occurs for a specific time interval while the thermal boundary layer is re-established which is given by t^*. This time interval is determined by the fraction of time the transient conduction heat transfer coefficient is greater than the forced convection term and is given in Eq. 3.20. By integrating the error function solution over this time, the sliding conduction term is given by Eq. 3.21.

$$q_w'' = \frac{k_l(T_w - T_l)}{\sqrt{\pi \alpha_l t}} \qquad 3.19$$

$$t^* = \left(\frac{k_l}{h_{fc}}\right)^2 \frac{1}{\pi \alpha_l} \qquad 3.20$$

$$q_{sc}'' = \frac{k_l(T_w - T_l)}{\sqrt{\pi \alpha_l t^*}} f a_{sl} t^* N'' \qquad 3.21$$

The sliding length and area influenced by the sliding bubbles (a_{sl}) is determined by the bubble growth while sliding and also the number of additional nucleation sites it may cross while sliding. The bubble is assumed to slide at the velocity of the liquid in its proximity and only in the direction of the flow. As in the forced convection term, the spacing between the bubbles,s, is calculated by assuming the bubbles are arranged in a square lattice arrangement. The distance a bubble slides is depicted in Figure 29, where l is the total distance a bubble slides. The

calculation of l is dependent on whether the bubble slides a distance greater or less than the spacing s.

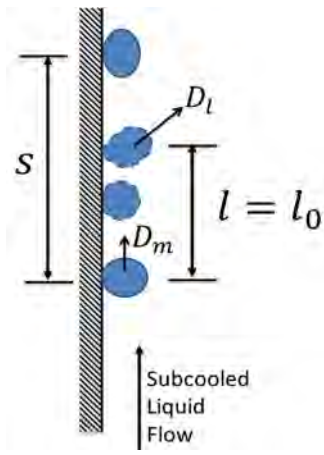

Figure 29: Illustration of a bubble sliding from its inception point and then departing from the heater after sliding a distance *l*.

The growth of the bubble while sliding is determined from a correlation against Maity's data [39] of a single bubble sliding in sub-cooled flow boiling and is given in Eq. 3.22 where D_{sl} is the bubble diameter after sliding a time t_{sl} and D_{in} is the diameter of the bubble when it begins sliding. Re_b is the Reynolds number of the bubble and Ja is the Jakob number given in Eqs. 3.23 and 3.24 respectively. U is the liquid velocity at the center of the bubble and ν_l is the kinematic viscosity of the liquid.

$$\frac{(D_{sl}^2 - D_{in}^2)}{t_{sl}\alpha_l Ja_{sup}} = \frac{1}{15(0.015 + 0.0023Re_b^{0.5})(0.04 + 0.023Ja_{sub}^{0.5})} \qquad 3.22$$

$$Re_b = \frac{2UR}{\nu_l} \qquad 3.23$$

$$Ja = \frac{\rho_l c_{pl} \Delta T}{\rho_v h_{fg}} \qquad 3.24$$

For example, if a bubble departs from its inception point and slides a distance s, then the time it takes to slide is given by Eq. 3.26 and $D_{in} = D_m$. The size after it slides (D_{sl}) can then be calculated. If the diameter after it slides is less than the lift-off diameter, then it will continue to slide and it also "absorbs" the bubble that was at the second nucleation site that the original bubble encountered. The addition of the volume of the bubble swept by the original sliding bubble is given by Eq. 3.25. Since most of the ebullition cycle is the wait time rather than the growth time, the additional volume added to the sweeping bubble is a fraction of the bubble departure diameter that uses the ratio of the growth time versus total time for an ebullition cycle.

$$D_{add} = t_g f D_m \qquad 3.25$$

The total distance a bubble slides can then be calculated as shown in Eq. 3.27 where N_{merged} is the number of bubbles the sliding bubble merged with on the heater and $l_{D_n - D_l}$ is the additional

length the sliding bubble travelled from the last bubble merger to lift-off. Using the average bubble size during sliding, as given in Eq. 3.28, the area affected by a sliding bubble is then $a_{sl} = D_{avg} l$.

$$t_{sl} = \frac{s}{v_b} \tag{3.26}$$

$$l = N_{merged} s + l_{D_n - D_l} \tag{3.27}$$

$$D_{avg} = D_m + 0.5(D_l - D_m) \tag{3.28}$$

To account for the bubbles that are "absorbed" by the sliding bubble as it passes over other active nucleation sites, the active nucleation site density is reduced. This is completed by employing a reduction factor when the sliding distance is greater than the spacing between bubbles that is given by Eq. 3.29. This provides a new active nucleation site density value that is shown in Eq. 3.30.

$$R_f = \frac{1}{l/s} = \frac{1}{l\sqrt{N''}} \tag{3.29}$$

$$N''^{*} = R_f N'' \tag{3.30}$$

The bubble departure and lift-off diameter force-balance models use a strong assumption that the departing bubbles are approximately spherical in shape. Once the bubbles begin to deviate from the spherical shape, the forces acting on the bubble can dramatically change. Most importantly is the shear lift force that causes more deformed bubbles to move away from the walls and into the bulk flow. To account for the effect of bubble deformability in bubble lift-off, the Eötvös (Eo) number is used and is shown in Eq. 3.31 where D is the bubble diameter and σ is the surface tension. The Eo is proportional to the ratio of the buoyancy force to the surface tension force. Therefore, at low Eo numbers, the surface tension is sufficient enough for the bubble to remain spherical in shape. Typically, the Eo number is also described with either the Morton (Mo) or Galileo (N) number to characterize the bubble shape in the surrounding fluid. The Mo number is a constant for a given fluid and given in Eq. 3.32. For low viscosity liquids, the Mo number is lower.

$$Eo = \frac{(\rho_l - \rho_v) g D^2}{\sigma} \tag{3.31}$$

$$Mo = \frac{(\rho_l - \rho_v) g \mu_l^4}{\rho_l^2 \sigma^3} \tag{3.32}$$

Since water is a low viscosity fluid, the Mo number is low. Therefore, when the Eo number is also low (for smaller bubbles), the bubbles are spherical in shape. As the Eo number increases, the bubbles become ellipsoidal in shape and "wobbly." They can eventually have a spherical cap shape if the Eo number becomes large enough. For high-Renyolds number flows, if the Eo number is at or below 0.1, the bubbles are essentially spherical.

A DNS study still under progress by Dabiri, et al. investigated the regime transitions in vertical channel upflow due to bubble deformability. The transition from low to high flow rate occurs because of the location of the bubbles in the channel at low Eo, the bubbles are spherical and

stay near the walls causing a lower flow rate than the single-phase solution. As Eo rises, the bubbles move to a more uniform distribution and the flow rate increases to the single-phase solution. This transition occurs rather abruptly at an Eo number of 2.5 and when Eo is greater than 3.5, there are no bubbles sliding along the walls. Therefore, when the Eo number is greater than 3.5, sliding bubbles are no longer considered as a mode of heat transfer.

Quenching

The quenching component in this new model is governed by the heated material because this heat transfer mode involves bringing the dry area of the bubble on the heater back to the wall superheat and temperature distribution prior bubble inception. In this method, the quenching term becomes a function of the material properties of the heated surface. It is employed when a bubble departs from its nucleation site and depicted in Figure 30. The quenching heat flux is shown in Eq. 3.33 where ρ_h is the density of the heater material, $c_{p,h}$ is the heat capacity, ΔT is the average temperature difference between the hot spot on the heater and the surrounding wall temperature in the bubble location (approximated as 2K), and V_q is the volume of the hot spot and given in Eq. 3.34 where volume is assumed to be a hemisphere of the same diameter as the dry area. The dry area is assumed to have half the radius of the bubble.

$$q_q'' = \rho_h c_{p,h} \Delta T V_q f N'' \tag{3.33}$$

$$V_q = \frac{4}{3}\pi\left(\frac{D_{dry}}{2}\right)^3 \frac{1}{2} = \frac{2}{3}\pi\left(\frac{D_{dry}}{2}\right)^3 \tag{3.34}$$

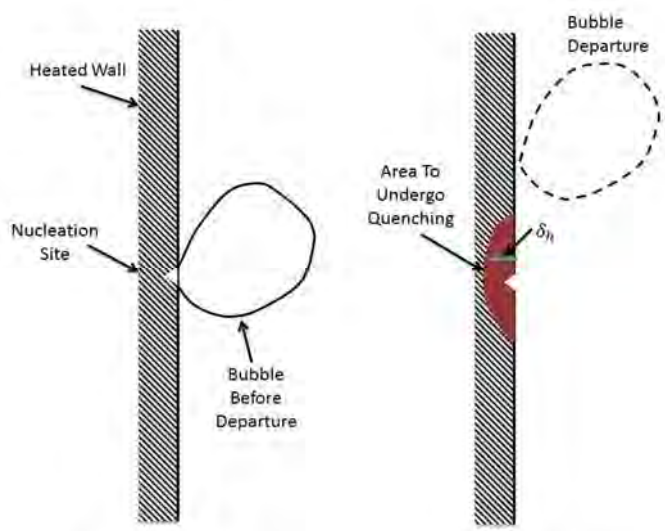

Figure 30: Illustration of bubble growth on a heater and the area in the influence of the bubble that is involved in the quenching heat flux.

3.3 Hardened Momentum Closure

The main objective of this work is to develop a set of general and robust momentum closure relations to work in combination with the discussed new heat partitioning model. While the specific application to PWR conditions focuses on small geometries and low void fractions, the model should possess generality in order to be extendable to all regimes that will be encountered during transient and accident analysis. In order to fulfill this challenging requirement an innovative approach will be employed, which considers local flow conditions on a cell-by-cell basis in order to apply the appropriate closure terms. Figure 22 shows a basic example of the CFD representation of a boiling channel. It is evident that hydrostatic forces will vary locally and the closure must include an approach capable of capturing this distinction.

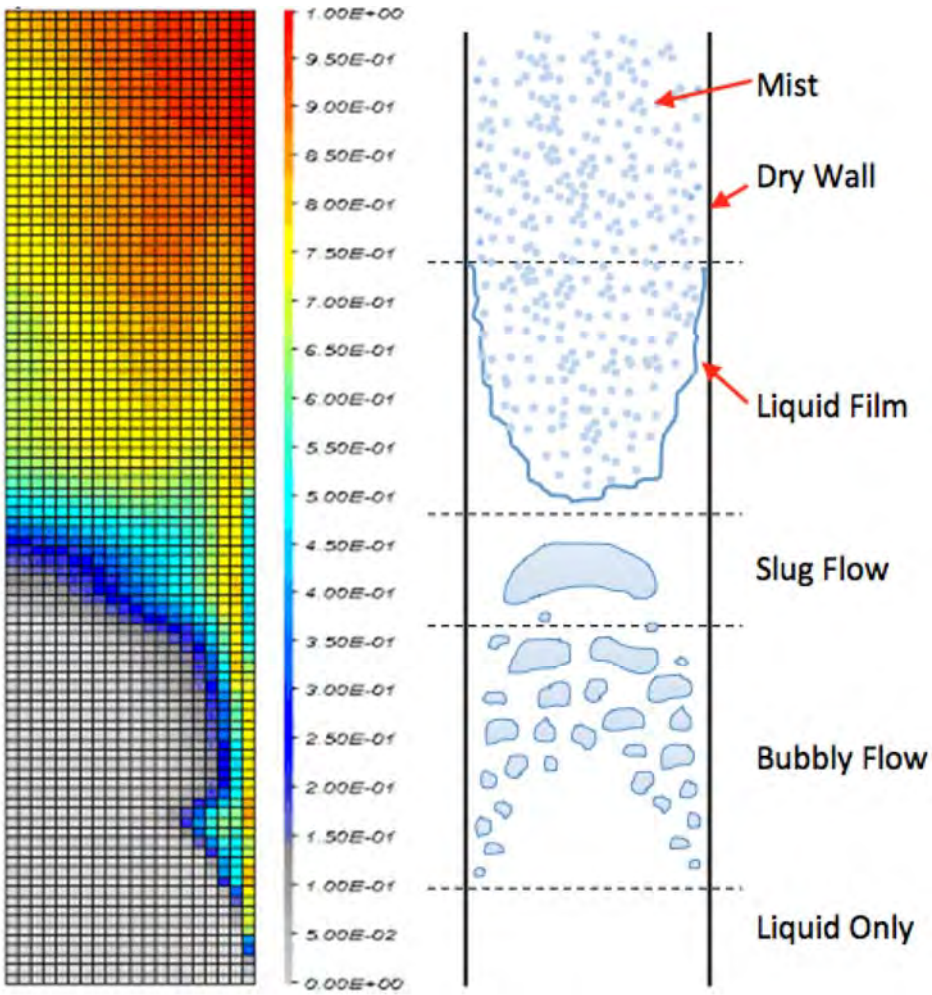

Figure 31: CFD representation of a boiling channel

The "local" closure approach is firstly necessary to make the model applicable to all flow conditions, but further has the great attractiveness of proving highly enhanced robustness during iterative solutions, as it naturally behaves as a form of "physical under-relaxation".

The closure relations that are considered in this work are drag, lift, and turbulence dispersion. For all these forces rather than applying a fixed closure relationship the selection of the

appropriate closure and interaction length scale is based on the local void fraction. Currently a simplified map is adopted where only 3 regions are described, as shown in Figure 23, the first one representing the bubbly region flow (below α_1), a dispersed flow region above α_2 and a transition region in between. While this simple map has shown to be sufficient for our PWR specific application, a more complex mapping will be necessary for a complete flow regimes description.

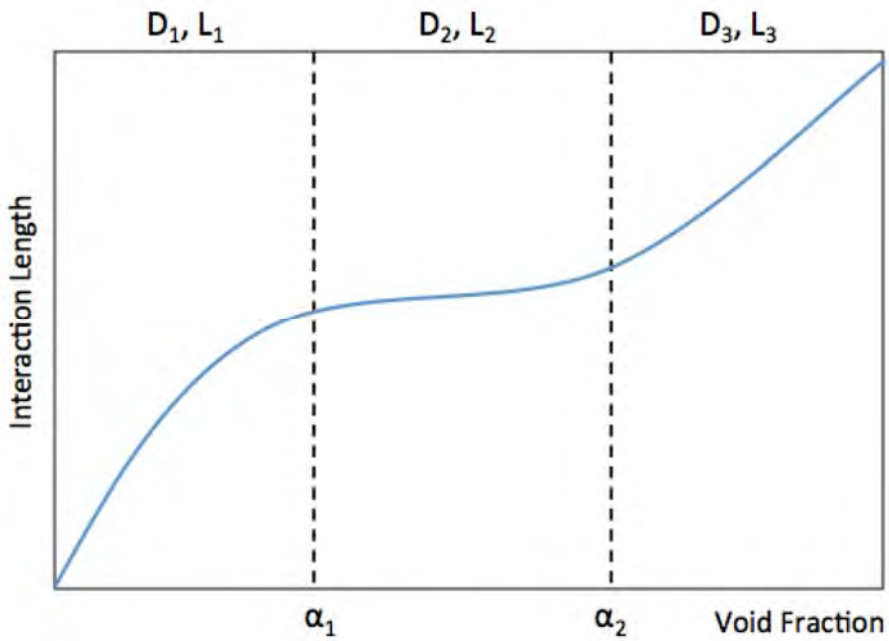

Figure 32: Local closure approach for PWR application.

3.3.1 Wall-Aware Lift Closure Formulation

Extensive testing both in the literature and in the early stage of this work have clearly shown the lift formulation to be the most challenging and influential component for PWR applications, where this transversal force drives the motion of bubbles in the narrow and long flow channels between the fuel rods, impacting heat transfer and neutron moderation. It is evident that efforts have therefore been concentrated on this aspect, and the results are discussed in this section.

The challenge in modeling the lift force, and in general the transverse forces acting on bubbles is that the limitations in measurement techniques have made them the lesser-understood components. Transverse forces are perpendicular to the relative velocity of the bubble with respect to the fluid and are commonly decomposed into lift and wall force in common M-CFD formulations. The lift force term is rightly motivated by the physics, while the wall force term is added as a correction in order to ensure that there is no gas (bubble) accumulation very close to the wall. In practice this creates stability issues in the flow solution, as both effects are of similar magnitude as one approaches the wall, yet have very different dependencies on the local properties. This compartmental view of the total transverse force is an over simplification which ignores the interplay between the two forces and the variation of the lift force as a function of

distance from the wall. Figure 24 shows how the currently implemented lift and wall forces increase in magnitude significantly near the wall.

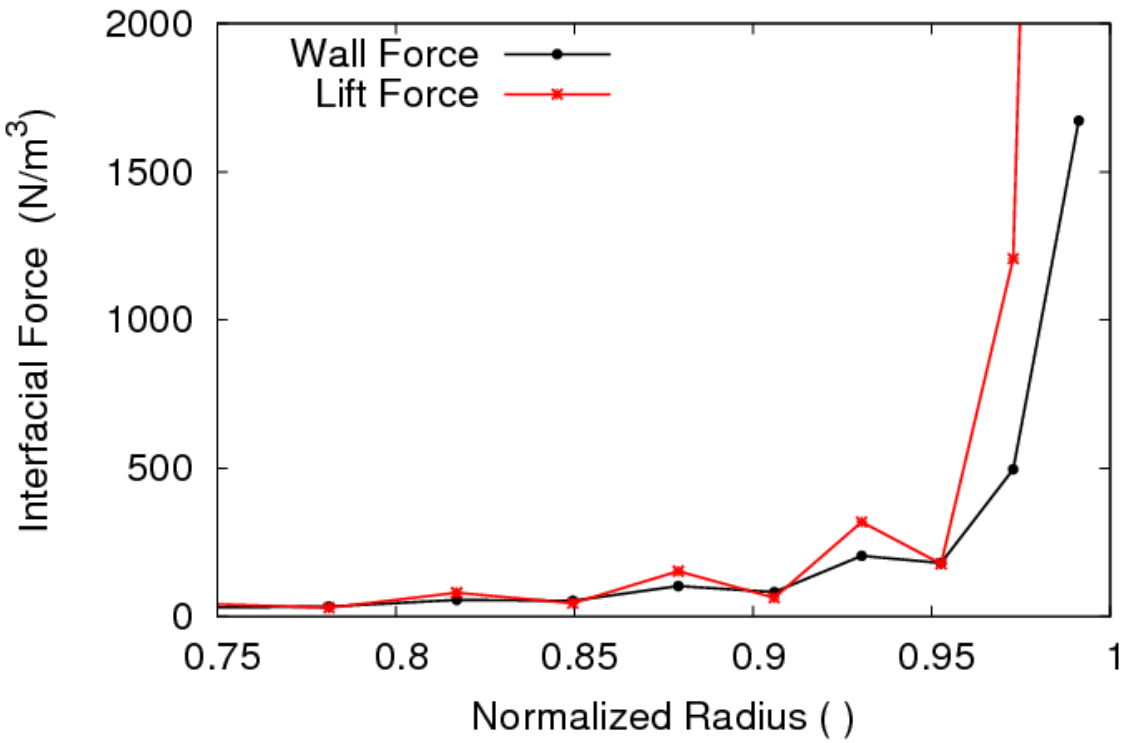

Figure 33: Lift/Wall forces near the wall of a bubbly pipe flow [23].

These large values for the lift force are unphysical, and in general the coefficients of the wall force are tweaked in order to cancel the shear lift force at the wall. The shear lift force itself is overpredicted as one moves toward the wall, because the assumptions that were used in its derivation become invalid.

After a review of the of the various options for lift and wall forces currently available in popular M-CFD codes, an analytical study combined to dedicated direct numerical simulations has been performed in order to eliminate the discussed limitation, and extend the closures to include more realistic scenarios. A new model has been derived for lift force in the presence of walls and its behavior has been tested and characterized using a turbulent pipe flow profile. The model proposed is a clever generalization and extension of the existing knowledge-base which leverages the advanced multiphase DNS capabilities of the CASL team. In order to allow accurate fitting of the lift coefficient a dedicated set of numerical experiments have been performed and are discussed in the next section.

While a full discussion of the model derivation is available in the THM.CLS.P7.06 milestone report, here we simply report the model and provide a graphical representation of the new wall dependence.

The Low Re model is taken from the original formulation of Legendre & Magnaudet [24]

- $$C_L^{low} = 6\frac{J(Sr, Re)}{\pi^2\sqrt{Re\,Sr}}, \text{ where } J(Sr,\ Re) = \frac{2.255}{(1+0.2\frac{Re}{Sr})^{3/2}} \qquad 3.35$$

The high Re model has been re-derived from least-squares fit of data away from wall

- $$C_L^{high} = \frac{\frac{1}{2}\left(1+\frac{310}{Re}-\frac{242}{Re^2}\right)}{1+\frac{176}{Re}+\frac{566}{Re^2}} \qquad 3.36$$

The combination of the 2 models give the all Re formulation

- $$C_L^{nowall} = \sqrt{C_L^{low^2} + C_L^{high^2}} \qquad 3.37$$

where the wall effects are included based on the DNS findings as

- $$C_L = C_L^{nowall}\left(\log_2\left(\frac{\mathrm{E}}{1-E}+2\right)\right)^{-2.3} \qquad 3.38$$

and E represents the inverse distance from wall expressed as ratio between bubble diameter *d* and distance from the wall *L*.

$$E = \frac{d}{2\,L} \qquad 3.39$$

which, as discussed, provides the correct limiting behavior, where the lift force decreases as bubbles approach the wall. The new closure is plotted in 3D so that one can see how it captures the variation of C_L as a function of E, Re, and Sr. The plots are shown in Figs. 25 and 26.

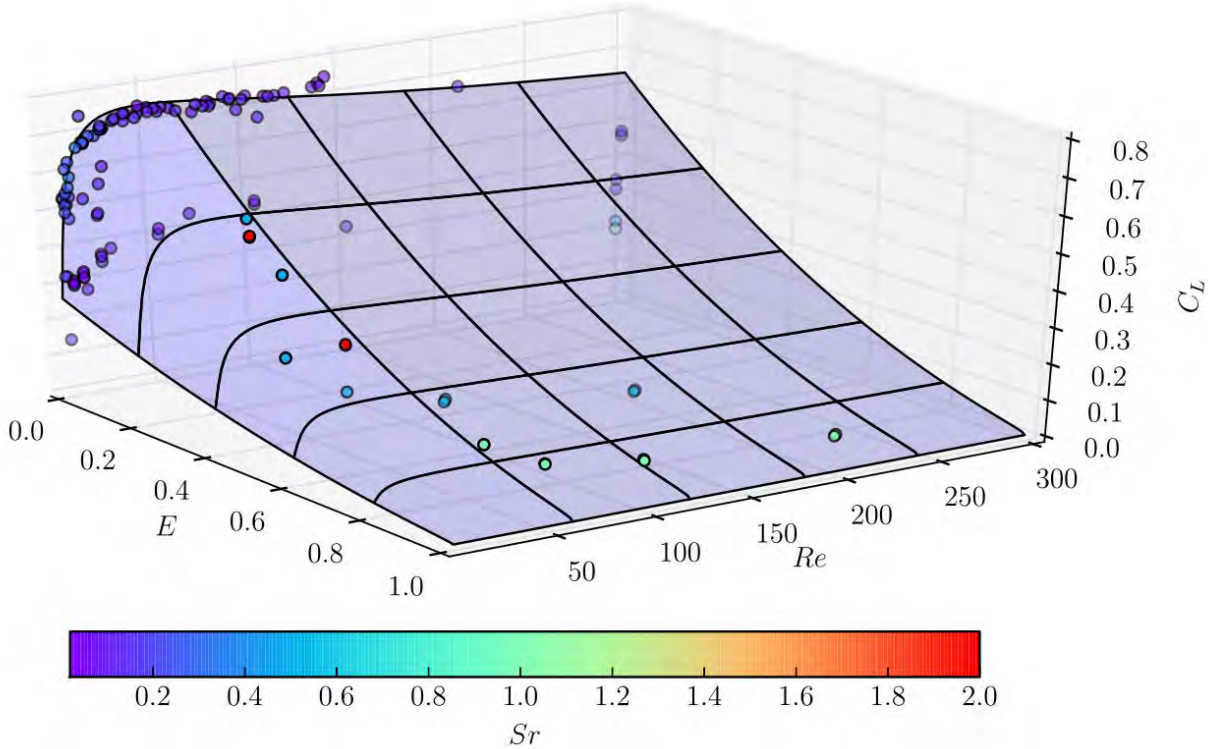

Figure 34: Surface plot of DRP model and pointwise data for Re > 2

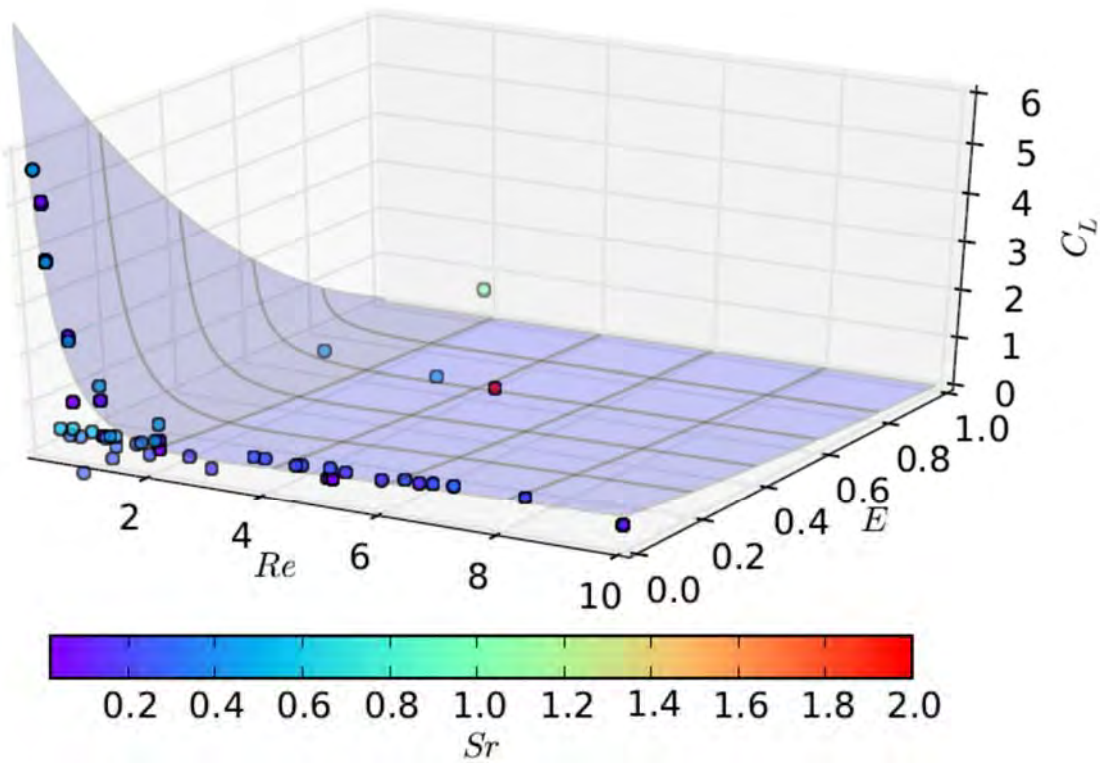

Figure 35: Surface plot of DRP model and pointwise data for Re ≤ 10

3.4 The role of ITM/DNS work

Interface tracking methods (ITM) offer a unique capability to provide a very consistent database for parameter optimization, where in the virtual approach all parameters can be perfectly controlled. ITM methods have been used in this work to examine the lift and drag on a single bubble in vertical shear flow. The effect of the flow parameters, including the shear, the deformability of the bubble, and the distance to the wall are shown and the reversal in lift force as deformability is increased and the distance to the wall is reduced. Results obtained using two different methods are in good agreement with each other as well as with experimental data from the literature. The results demonstrate that lift and drag can be obtained in a reliable way for a wide range of parameters, but strategies for examining a broader range of parameters are identified. The previous section has shown an application of this uniquely valuable set of data.

Description of ITM/DNS Codes

PHASTA

PHASTA is a parallel, hierarchic, higher-order accurate (from the 2nd to the 5th order accuracy, depending on function choice), adaptive, stabilized (finite element) transient analysis flow solver (both incompressible and compressible). This approach has been shown by (Jansen, 1999) and (Whiting & Jansen, 2001) to be an effective tool for bridging a broad range of length scales in turbulent (RANS, large-eddy simulation (LES), detached eddy simulation (DES), DNS) flows. PHASTA (and its predecessor, ENSA) was the first unstructured grid LES code (Jansen, 1993) and has been applied to turbulent flows ranging from validation benchmarks (channel flow, decay of isotropic turbulence) to complex flows (airfoils at maximum lift, flow over a cavity, near lip jet engine flows and fin-tube heat exchangers). The PHASTA code uses advanced anisotropic adaptive algorithms (Sahni, et al., 2006) and the most advanced LES/DES models (Tejada-Martinez & Jansen, 2005). Note that DES, LES, and DNS are computationally intensive even for single phase flows. This capability has been recently (Nagrath, et al., 2006) extended to two phase flows where we use the level set method to track the boundary between two immiscible fluids (either compressible - where we captured new instabilities in sonoluminescence, or incompressible – to study bubble coalescence and two-phase turbulence (Bolotnov, et al., 2011)). PHASTA uses anisotropically adapted unstructured grids and its highly scalable performance on massively parallel computers has already been demonstrated (the code has shown good scaling out to 288*1024 IBM Blue Gene processors, at JUGENE, BG/P (Germany, #12 in top500 as of June 2011)), (Zhou, et al., 2010).

PHASTA is an *open source* code. However, in the current setup, it uses commercial linear solver libraries from Acusim, Inc. A possible switch to open-source solvers is considered (e.g. Trilinos, PETSc). Meshing capabilities utilize tools from Simmetrix, Inc. Creating mesh converters from open-source tools to PHASTA format is also a possibility. PHASTA works with hexahedral, tetrahedral and mixed meshes.

Governing Equations

The spatial and temporal discretization of the Incompressible Navier-Stokes (INS) equations within the FEM code PHASTA has been described in (Whiting & Jansen, 2001) and (Nagrath,

et al., 2006). The strong form of the INS equations is given by:

Continuity: $$u_{i,i} = 0 \quad 3.40$$

Momentum: $$\rho u_{i,t} + \rho u_j u_{i,j} = -p_{,i} + \tau_{ij,j} + f_i \quad 3.41$$

For the incompressible flow of a Newtonian fluid, the viscous stress tensor is related to the fluid's viscosity and the strain rate tensor as:

$$\tau_{ij} = 2\mu S_{ij} = \mu(u_{i,j} + u_{j,i}) \quad 3.42$$

Using the Continuum Surface Tension (CST) model of (Brackbill, et al., 1992), the surface tension force is computed as a local interfacial force density, which is included in f_i.

Level Set Method

The level set method of Sussman [(Sussman & Fatemi, 1999), (Sussman & Smereka, 1997), (Sussman, et al., 1999), (Sussman, et al., 1998)] and (Sethian, 1999) involves modeling the interface as the zero-level set of a smooth function, φ, where φ is often called the first scalar and it represents the signed distance from the interface. Hence, the interface is defined by $\varphi = 0$. The scalar, φ, is convected within a moving fluid according to,

$$\frac{D\varphi}{dt} = \frac{\partial \varphi}{\partial t} + \underline{u} \cdot \nabla \varphi = 0 \quad 3.43$$

where $\underline{u}$ is the flow velocity vector. Phase-1, the liquid phase, is indicated by a positive level set, $\varphi > 0$, and phase-2, the gas, by a negative level set, $\varphi < 0$. Since evaluating the jump in physical properties using a step change across the interface leads to poor computational results, the properties near an interface were defined using a smoothed Heaviside kernel function, H_ε, given by (Sussman, et al., 1999):

$$H_\varepsilon(\varphi) = \begin{cases} 0 & ,\varphi < -\varepsilon \\ \frac{1}{2}\left[1 + \frac{\varphi}{\varepsilon} + \frac{1}{\pi}\sin\left(\frac{\pi\varphi}{\varepsilon}\right)\right] & ,|\varphi| < \varepsilon \\ 1 & ,\varphi > \varepsilon \end{cases} \quad 3.44$$

The fluid properties are then defined as:

$$\rho(\varphi) = \rho_1 H_\varepsilon(\varphi) + \rho_2(1 - H_\varepsilon(\varphi)) \quad 3.45$$

$$\mu(\varphi) = \mu_1 H_\varepsilon(\varphi) + \mu_2(1 - H_\varepsilon(\varphi)) \quad 3.46$$

Although the solution may be reasonably good in the immediate vicinity of the interface, the distance field may not be correct throughout the domain since the varying fluid velocities throughout the flow field distort the level set contours (especially in fully resolved turbulent flow simulations). Thus, the level set was corrected with a re-distancing operation by solving the following PDE (Sussman & Fatemi, 1999):

$$\frac{\partial d}{\partial \tau} = S(\varphi)\left[1 - |\nabla d|\right] \quad 3.47$$

where d is a scalar that represents the corrected distance field and τ is the pseudo time over which the PDE is solved to steady-state. This may be alternately expressed as the following transport equation:

$$\frac{\partial d}{\partial \tau} + \underline{w} \cdot \nabla d = S(\varphi) \quad 3.48$$

The so-called second scalar, d, is originally assigned the level set field, φ, and is convected with a pseudo velocity, $\underline{w}$, where,

$$\underline{w} = S(\varphi)\frac{\nabla d}{|\nabla d|} \qquad 3.49$$

and $S(\varphi)$ is defined as:

$$S(\varphi) = \begin{cases} -1 & ,\varphi < -\varepsilon_d \\ \left[\dfrac{\varphi}{\varepsilon_d} + \dfrac{1}{\pi}\sin\left(\dfrac{\pi\varphi}{\varepsilon_d}\right)\right] & ,|\varphi| < \varepsilon_d \\ 1 & ,\varphi > \varepsilon_d \end{cases} \qquad 3.50$$

where ε_d is the distance field interface half-thickness which, in general, may be different from ε used in Eq. 5. Note that the zeroth level set, or interface, $\varphi = 0$, does not move since its convecting velocity, $\underline{w}$, is zero. Solving the second scalar to steady-state restores the distance field to $\nabla d = \pm 1$ but does not alter the location of the interface. The first scalar, φ, is then updated using the steady solution of the second scalar, d.

FTC3D

FTC3D is a specialized code for direct numerical simulations of multiphase flows. The "one-fluid" Navier-Stokes equations for incompressible flows, where a single set of equations is used for the whole flow domain, are solved on a regular structured staggered grid using an explicit projection method. Time integration is done by a second order predictor-corrector method, the viscous terms are discretized by second-order centered differences and the advection terms are approximated using a QUICK scheme. The pressure equation is solved using a multigrid method or a Krylov scheme (BiCGStab).

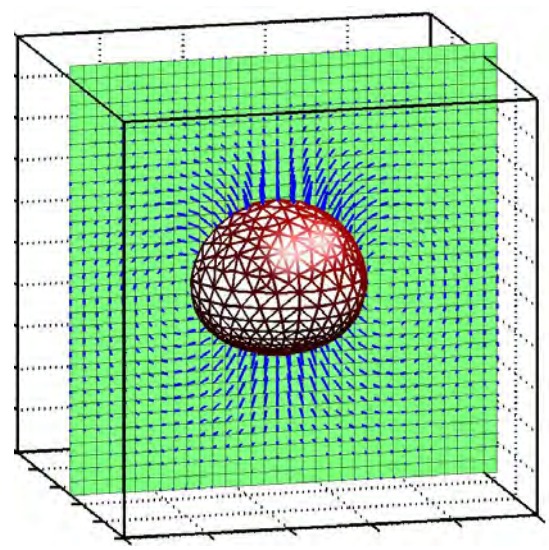

Figure 36: The front tracking code uses a fixed structured grid for the solution of the fluids equation and an unstructured surface grid to track the interface between the different fluids.

The interface between the different fluids is tracked by connected marker points that are advected with the flow. The interface, or the "front," consists of points and triangular elements that connect the points. Once the marker points have been advected, a marker function is constructed from the new interface location. The front is also used to compute surface tension, which is then smoothed onto the fluid grid and added to the discrete Navier-Stokes equations. In addition to the computation of the surface tension and the construction of the marker function, the chief challenge in front-tracking is the dynamic updating of the front, whereby marker points are added or deleted to maintain the point density needed to fully resolve the interface. This is done fully automatically as part of the front advection.

The method was introduced by Unverdi & Tryggvason (1992) and for description of the original method, as well as various improvements and refinements, see Tryggvason et al. (2001) and Tryggvason et al. (2011). The method has been used to simulate a large range of multiphase flows, including bubbly flows. See, Bunner & Tryggvason (2002a,b), Esmaeeli & Tryggvason (2005), and Biswas, Esmaeeli & Tryggvason (2005), for example. For other implementation of

similar ideas and applications to bubbly flows, see Dijkhuizen et al. (2010a,b); van Sint Annaland et al. (2006); Hao & Prosperetti (2004); Hua & Lou (2007); Muradoglu & Kayaalp (2006), for example.

ITM case design

In order to provide the lift coefficient estimate in clean uniform shear flow it was decided to use inflow/ouflow boundary conditions. This provides a better liquid flow field around the bubble compared to more conventional periodic boundary conditions in stream-wise direction. Uniform shear inflow avoids having the bubble traveling through its own wake and disturbing the measurements of lift/drag forces.

Figure 38 shows the slice of the computational domain (normal to z-axis) and provides a basic idea how the simulations were performed. To achieve the uniform shear flow around the bubble uniform velocity boundary condition was applied on each wall (in this particular case with values of 0.0375 on the top and 0.0125 on the bottom) along with uniform shear inflow boundary condition on the left. The domain width of 0.025 results in the shear rate of 1.0 s^{-1} for this case.
The following procedure has been used to obtain the results:

- the bubble is introduced in the level set method by specifying an analytical expression for a distance field:

$$\varphi_i = (x - x_j)^2 + (y - y_j)^2 + (z - z_j)^2 - R_j^2 \qquad 3.51$$

  where x_j, y_j, z_j are the coordinates of the bubble and R_j is the radius.
- two control forces (applied independently) in x and y directions were used to keep the bubble location nearly constant. After achieving steady-state results the x-direction force fully counter-acts the drag force the bubble experiencing due to upcoming flow and the y-direction force counter-acts the lift force.
- the simulation is carried out to acquire sufficient data for convergent results in control force evolution.

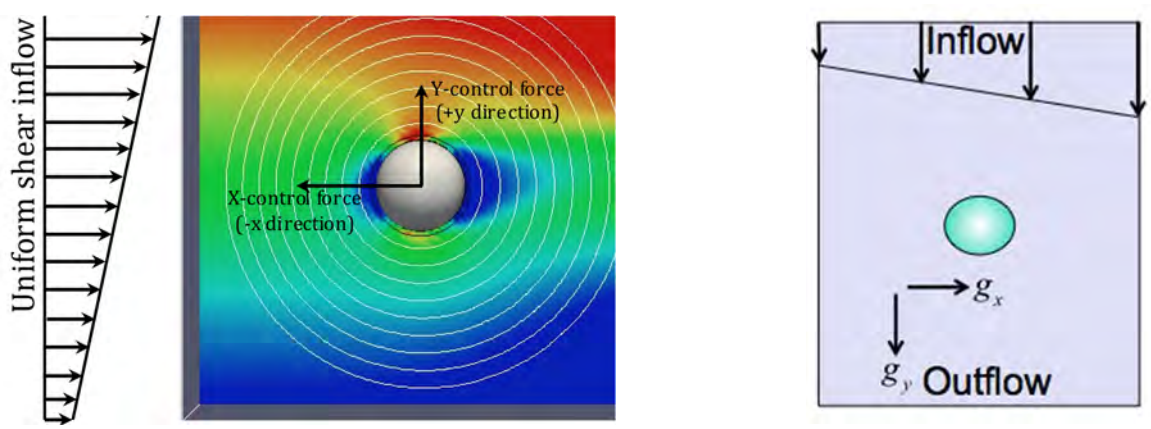

Figure 37: Simulation domain and control forces. Left: Setup and coordinates for the PHASTA runs. Right: Setup and coordinates for the FTC3D runs.

Data extraction and drag/lift force measurement approach

The computational domain used in the FTC3D runs is a rectangular channel where the inflow at the top is specified, the left and right boundaries are rigid no-slip walls with a given velocity and periodic boundary conditions are used in the spanwise direction. The computational domain, shown in Figure 37, is the same as used for the PHASTA simulations but the orientation and notation is slightly different.

To keep the bubble stationary, the gravity is adjusted by a PID (proportional-integral-derivative) controller that is based on the location and velocity of the bubble centroid. At every time step, the new values are found by:

$$\begin{aligned} g_x^{\alpha+1} &= g_x^{\alpha} - c_{Px}\left(x - x_0\right) - c_{Ix}\int\left(x - x_0\right)dt - c_{Dx}U_b \\ g_y^{\alpha+1} &= g_y^{\alpha} - c_{Py}\left(y - y_0\right) - c_{Iy}\int\left(y - y_0\right)dt - c_{Dx}V_b \end{aligned} \qquad 3.52$$

For most of the calculations reported in the section on FTC3D, we use the following control parameters:

$$\begin{aligned} c_{Px} &= 0.02;\ c_{Ix} = 0.01;\ c_{Dx} = 0.02 \\ c_{Py} &= 0.03;\ c_{Iy} = 0.02;\ c_{Dy} = 0.05 \end{aligned} \qquad 3.53$$

Once gravity acceleration has been determined, the lift and drag coefficients can be determined by balancing the buoyancy and lift or drag. PHASTA used the same approach, with slightly different coefficients for some cases.

For the FTC3D results we do so in the following way. The lift force is given by:

$$F_L = -C_L\rho\frac{\pi d^3}{6}\left(V_b - V_L\right)\times\Omega_L \text{ where } \left|\Omega_L\right| = \frac{\Delta V}{L} \qquad 3.54$$

The buoyancy force in the horizontal direction is:

$$F_B = \Delta\rho\frac{\pi d^3}{6}g_x$$

$$F_L = -C_L\rho\frac{\pi d^3}{6}\left(V_b - V_L\right)\times\Omega_L \text{ where } \left|\Omega_L\right| = \frac{\Delta V}{L} \qquad 3.55$$

and at steady state the buoyancy balances the lift, $F_B = F_L$. We can isolate the lift coefficient, resulting in:

$$C_L = \frac{\Delta\rho g_x L}{\rho V_L \Delta V} \text{ where } \left|\Omega_L\right| = \frac{\Delta V}{L} \qquad 3.56$$

Similarly, the drag in the vertical direction is:

$$F_D = C_D\frac{\pi d^2}{8}\rho V_b^2 \qquad 3.57$$

which must be balanced by buoyancy in the vertical direction. Thus

$$C_D = \frac{4}{3}\frac{d\Delta\rho g_y}{\rho V_b^2} \qquad 3.58$$

The various non-dimensional numbers are defined as:

$$\mathrm{Re} = \frac{\rho d V_b}{\mu}; \quad Eo = \frac{\Delta\rho g d^2}{\sigma}; \quad M = \frac{\Delta\rho g \mu^4}{\rho^2 \sigma^3}; \quad G = \frac{\rho d^2}{\mu}\frac{\Delta V}{L}; \qquad 3.59$$

PHASTA

The value which is extracted by overall control forces in the PHASTA code is measured in [N/kg], and it is the corresponding buoyancy forces due to the 'control forces' that balance lift force and drag force. We use the following lift force formula (Tomiyama, et al., 2002):

$$F_{LF} = -C_{LF}\rho_L V_b \left(V_G - V_L\right) \times rotV_L \qquad 3.60$$

where

$$\left|rotV_L\right| = \left|\frac{dV_L}{dy}\right|, \ \left|v_r\right| = \left|V_G - V_L\right| \qquad 3.61$$

in our cases. The drag equation is given by

$$F_D = \frac{1}{2} C_D \rho_L v_r^2 A \qquad 3.62$$

The half thickness of the interface (applicable for level set method approach only) is determined in the following way

$$r = \frac{d}{\gamma_d} \cdot \varepsilon \qquad 3.63$$

where the d is the bubble diameter, γ_d is the resolution across bubble diameter and ε is the number of elements across the half interface.

The density distribution of the interface can be described by Eqs. 3.45 and 3.46. The average density within the blended level-set interface is:

$$\bar{\rho}_s = \frac{\rho_L + \rho_G}{2} \qquad 3.64$$

The volume of gas only region is

$$V_G = \frac{4}{3}\pi\left(R_b - r\right)^3 \qquad 3.65$$

and the volume of the interface region is

$$V_s = \frac{4}{3}\pi\left(R_b + r\right)^3 - \frac{4}{3}\pi\left(R_b - r\right)^3 \qquad 3.66$$

In the x direction (stream-wise), the force balance is given by

$$F_D = \left|g + xcf\right|\left[\left(\rho_L - \rho_G\right)V_G + \left(\rho_L - \bar{\rho}_s\right)V_s\right] = \frac{1}{2} C_D \rho_L v_r^2 A \qquad 3.67$$

And in y direction, the force balance is

$$F_{LF} = \left|ycf\right|\left[\left(\rho_L - \rho_G\right)V_G + \left(\rho_L - \bar{\rho}_s\right)V_s\right] = C_{LF}\rho_L V_b \left|v_r\right|\left|\frac{dv}{dy}\right| \qquad 3.68$$

After getting the *xcf* and *ycf*, we have calculated the corresponding coefficients based on the above equations. For instance, in the case for shear rate is 1.0 the average 'y control force' for timesteps 1000 to 3000 is *ycf*=0.0116; the lift coefficient calculated is 0.3441. The average 'x control force' from timestep 1000 to timestep 6000 is xcf=-0.0311; the drag coefficient calculated is 0.6105.

Results for PHASTA simulations and measurements

Table 4 summarizes the presented simulations done using the PHASTA-ITM code. We will overview selected cases to present more detailed results about the bubble behavior. 3 basic studies were performed to evaluate the influence of the shear rate; influence of relative velocity and influence of the wall presence on the estimates of the lift and drag coefficients.
Shear rate influence was evaluated using the "S" group of simulations: S1, S2, S5 and S10 representing the bubble in shear rates of 1, 2, 5 and 10. We have observed a decreased lift coefficient for higher shear rates. Note that S5 and S10 cases used partially negative inflow boundary conditions to obtain a combination of low relative velocity and high shear rates in a domain with fixed bubble position.

Relative velocity influence on both lift and drag was studied by increasing the velocity of both walls while maintaining the same shear rate. The set of cases designated by "R" was performed: R25; R50; R100.

The third study involved evaluating the influence of the wall on the lift force. For the specific set of conditions the wall proximity resulted in an increase of the lift coefficient since original direction of the lift force was away from the top wall (similar to downflow conditions). We have investigated both no-slip and free-slip walls (NSW and SW cases) to quantify the effect of the wall friction on the liquid "blockage" of the bubble and assist the development of the new closure laws for lift forces near solid boundaries.

Table 4. PHASTA mesh / simulation parameters

Case studies		Description	Results
Shear rate study	S1: $\frac{dv}{dy} = 1.0$	Uniform shear of 1.0; relative velocity of 0.025; bubble is located in the center of the domain. Domain width is 5 bubble diameters. Bubble diameter is 5mm	$C_{lift} = 0.3441$; $C_{drag} = 0.6105$
	S2: $\frac{dv}{dy} = 2.0$	Uniform shear of 2.0; relative velocity of 0.05	$C_{lift} = 0.3523$; $C_{drag} = 0.2089$
	S5: $\frac{dv}{dy} = 5.0$	Uniform shear of 5.0; relative velocity of 0.05	$C_{lift} = 0.2342$; $C_{drag} = 0.2057$
	S10: $\frac{dv}{dy} = 10.0$	Uniform shear of 10.0; relative velocity of 0.05	$C_{lift} = 0.2118$; $C_{drag} = 0.2322$
	S50: $\frac{dv}{dy} = 50.0$	Uniform shear of 50.0; relative velocity of 0.05. Bubble of 0.1 mm.	*in progress*
Relative velocity studies ($\frac{dv}{dy} = 1.0$)	R25: $V_r = 0.025$	Identical to S1	$C_{lift} = 0.3441$; $C_{drag} = 0.6105$
	R50: $V_r = 0.050$	Uniform shear of 1.0; relative velocity of 0.05	$C_{lift} = 0.3248$; $C_{drag} = 0.1932$
	R100: $V_r = 0.100$	Uniform shear of 1.0; relative velocity of 0.1	$C_{lift} = 0.5021$; $C_{drag} = 0.1013$
No-slip wall effect study	NSW1:	"No Slip Wall" study. Uniform shear of 2.0; Bubble is located at 1 radius distance (measured from the top bubble surface towards the top wall); relative velocity of 0.065	$C_{lift} = 0.3016$; $C_{drag} = 0.1411$
	SW1:	"Slip Wall" case. Uniform shear of 2.0; relative velocity of 0.065. The top wall is free slip boundary condition to allow free flow of liquid in the blockage region between the bubble and the wall.	$C_{lift} = 0.2952$; $C_{drag} = 0.1396$
	NSW0.5:	Reduced distance between the bubble and the wall compared to NSW1 (half the radius). Relative velocity in this case: 0.0675	$C_{lift} = 0.4888$; $C_{drag} = 0.1440$
	SW0.5:	Reduced distance between the bubble and the wall compared to SW1 (half the radius). Relative velocity in this case: 0.0675	$C_{lift} = 0.4544$; $C_{drag} = 0.1374$
	NSW0.25:	Reduced distance between the bubble and the wall compared to NSW1 (quarter the radius). Relative velocity in this case: 0.06875	$C_{lift} = 0.7733$; $C_{drag} = 0.1754$
	ONSW1:	Uniform shear of 2.0; Bubble is located at 1 radius distance (measured from the bottom bubble surface towards the opposite/bottom wall); relative velocity of 0.065 (wall velocities: 0.055, 0.105)	$C_{lift} = 0.1938$; $C_{drag} = 0.1756$
	ONSW0.5:	Reduced distance between the bubble and the wall compared to ONSW1 (half the radius). Relative velocity in this case: 0.0675 (wall velocities: 0.06, 0.11)	$C_{lift} = 0.0192$; $C_{drag} = 0.1258$
	ONSW0.25:	Reduced distance between the bubble and the wall compared to ONSW1 (quarter the radius). Relative velocity in this case: 0.06875 (wall velocities: 0.0625, 0.1125)	$C_{lift} = -0.1697$; $C_{drag} = 0.0803$

Case S1/R25: The detailed information for each case will be summarized in a table.

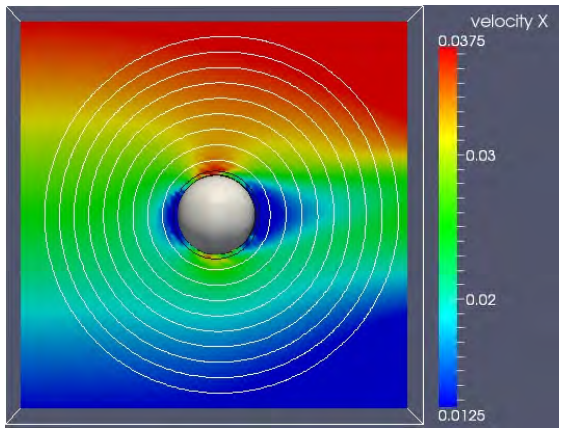

Shear rate: 1.0 s^{-1}
Relative velocity: 0.025 m/s
Density: 996.5/1.161 (kg/m^3)
Viscosity: 8.5439E-04 (liquid); 1.858E-05 (gas)
Bubble diameter: 5 mm
Eo/Bo number: 0.0782
Force estimate is over timestep range of: 1000 - 3000
Drag control force: 0.0689 N/kg
Lift control force: 0.0116 N/kg
Drag coefficient: 0.6105
Lift coefficient: 0.3441

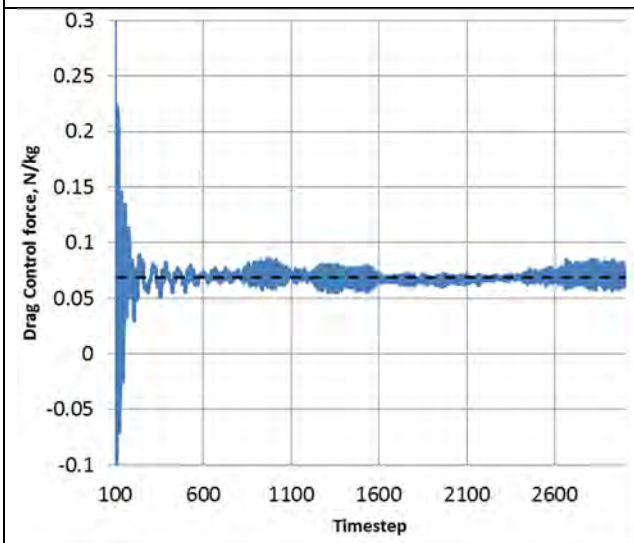

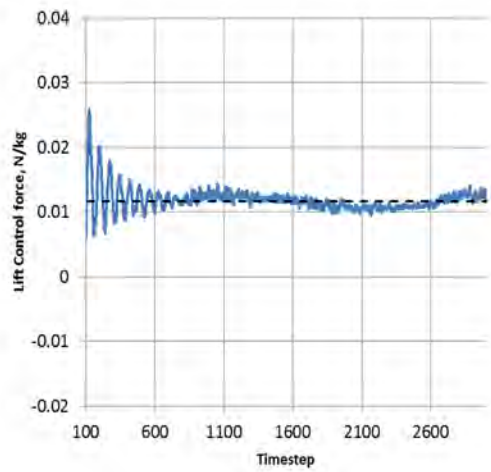

Figure 38. Summary of the S1/R25 case with uniform shear of 1.0. Top left shows sample of velocity distribution around the bubble, bottom left and right: control force evolution in horizontal and vertical directions, respectively. Top right shows basic case parameters and lift/drag coefficient evaluation results.

Case S5:

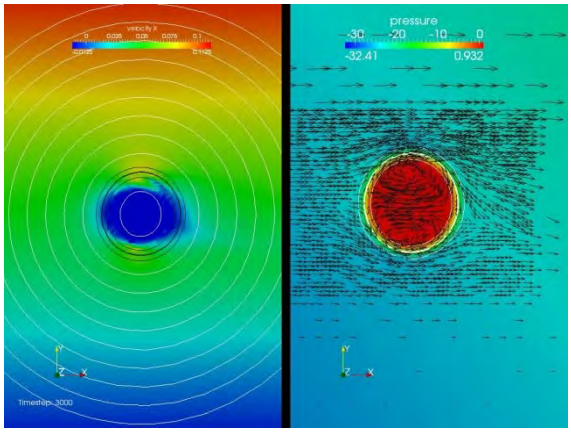

Shear rate: 5.0 s^{-1}
Relative velocity: 0.050 m/s
Density: 996.5/1.161 (kg/m^3)
Viscosity: 8.5439E-04 (liquid); 1.858E-05 (gas)
Bubble diameter: 5 mm
Eo/Bo number: 0.1077
Force estimate is over timestep range of: 1000 - 3000
Drag control force: 0.0919 N/kg
Lift control force: 0.0775 N/kg
Drag coefficient: 0.2057
Lift coefficient: 0.2342

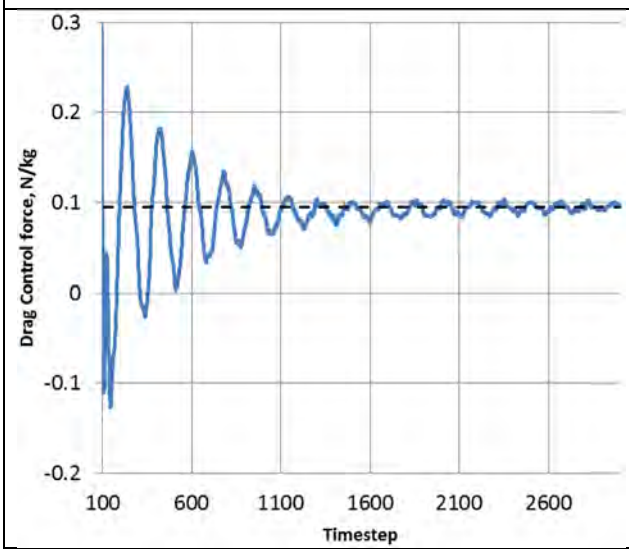

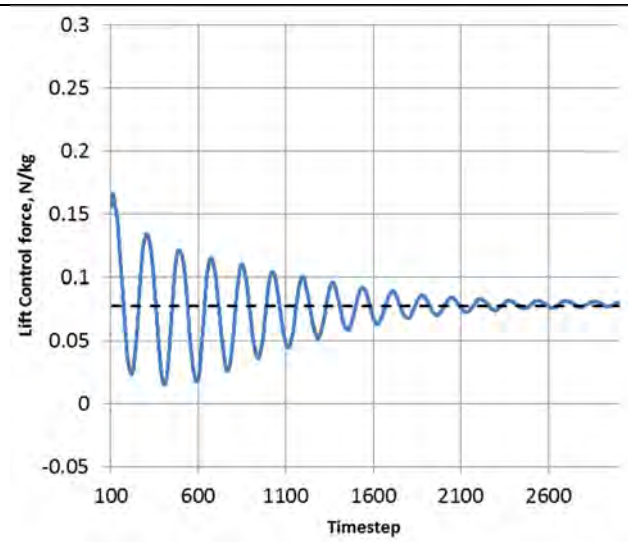

Figure 39. Summary of the S5 case with uniform shear of 5.0.

Case S10:

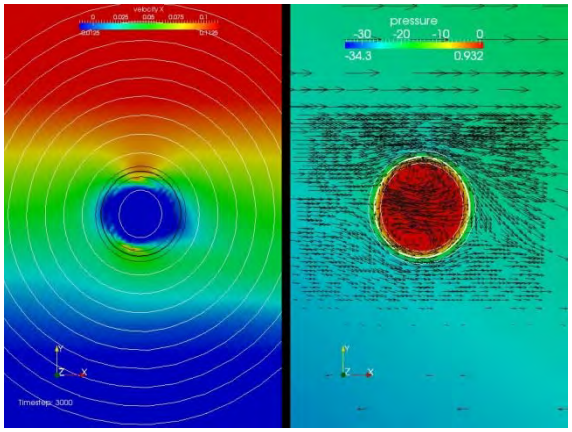

Shear rate: 10.0 s^{-1}
Relative velocity: 0.050 m/s
Density: 996.5/1.161 (kg/m^3)
Viscosity: 8.5439E-04 (liquid); 1.858E-05 (gas)
Bubble diameter: 5 mm
Eo/Bo number: 0.1519
Force estimate is over timestep range of: 1000 - 3000
Drag control force: 0.1038 N/kg
Lift control force: 0.1402 N/kg
Drag coefficient: 0.2322
Lift coefficient: 0.2118

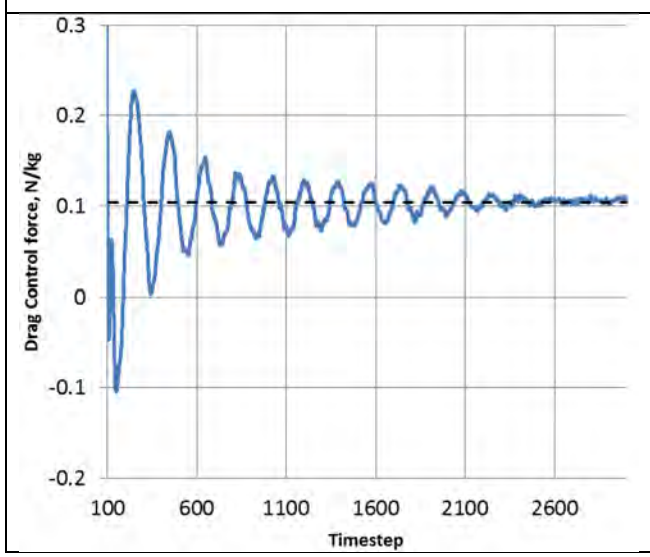

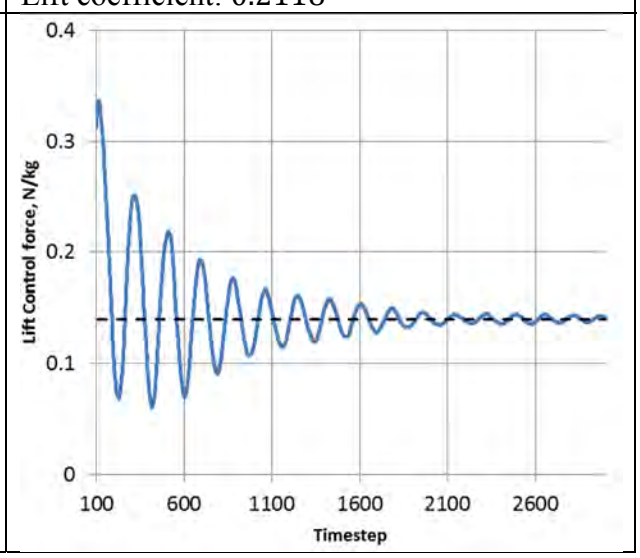

Figure 40. Summary of the S10 case with uniform shear of 10.0.

Figure 41 demonstrated the ITM capabilities of resolving the high shear rate flows (still laminar at this time) with low relative velocity. In LWR conditions we expect similar behavior since the relative velocity of the bubble is controlled by the balance of drag and buoyancy forces and will be fairly small (case S50 is performed for 0.1mm bubble). However, the shear rate is expected to reach values of 1000 or more. The tested capability as part of this effort demonstrated that applying fixed velocity boundary conditions for both "inflow" and "outflow" with negative portions in each outlet is possible without any adverse effects on code convergence. Note the velocity field shown with vectors in Figure 41.

Case S50: Shear rate study.

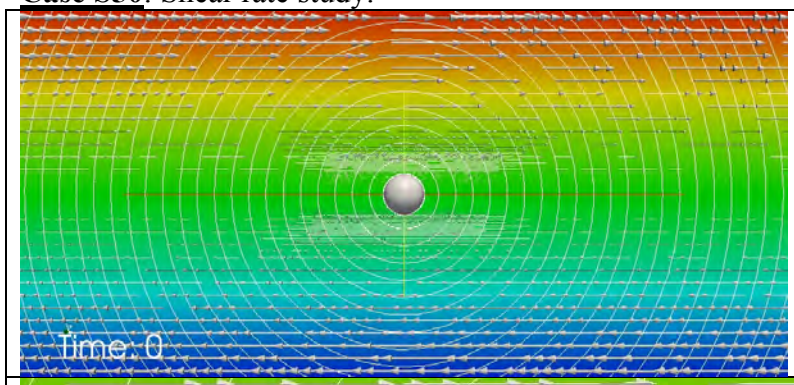

Shear rate: 50.0 s^{-1}
Relative velocity: 0.0005 m/s
Density: 712.136/46.1678 (kg/m^3)
Viscosity: 8.58961E-05 (liquid); 1.96512E-05 (gas)
Bubble diameter: 0.1 mm
Channel Width: 1.0 mm

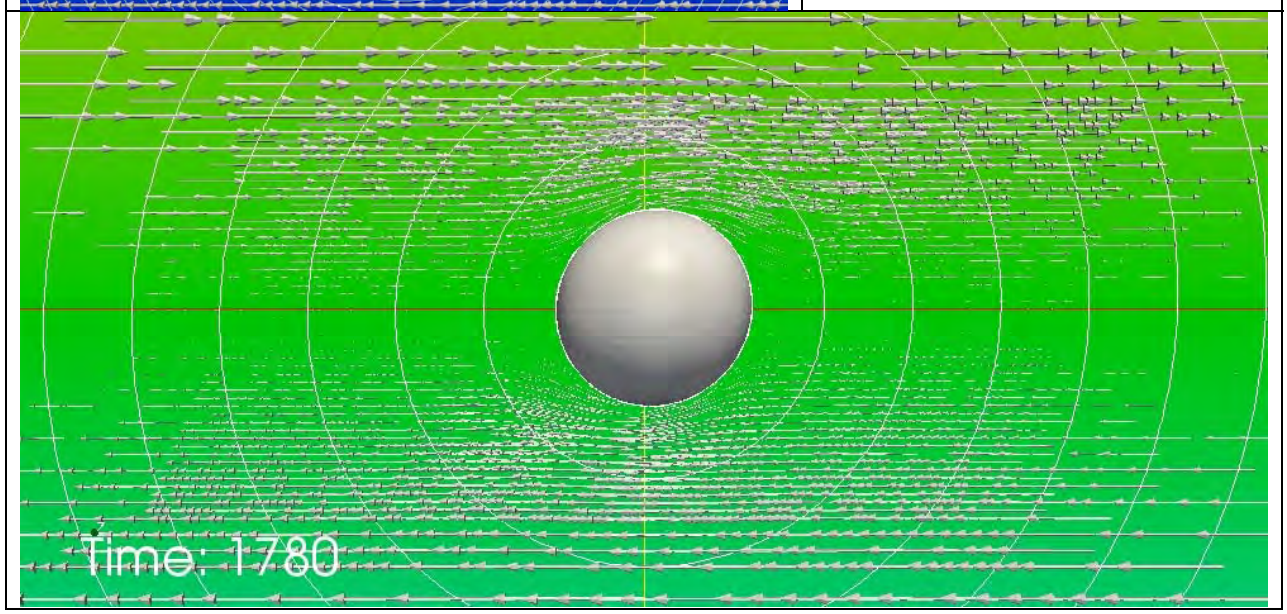

Figure 41. Summary of the S50 case with uniform shear of 50.0.

Case R50: Relative velocity study.

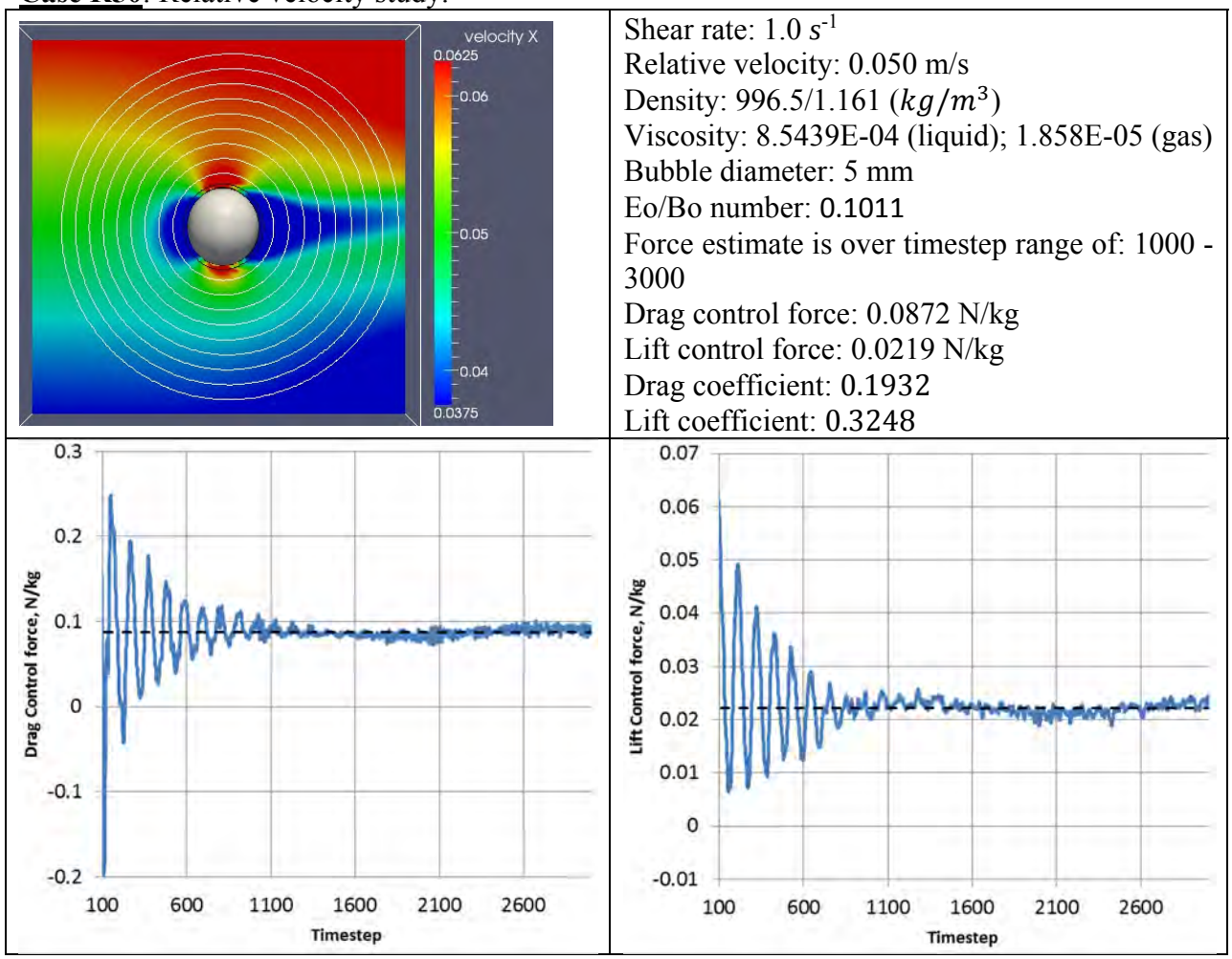

Figure 42. Summary of the R50 case with uniform shear of 1.0 with increase relative velocity.

Case NSW0.5: The detailed information for this case is summarized in the following table.

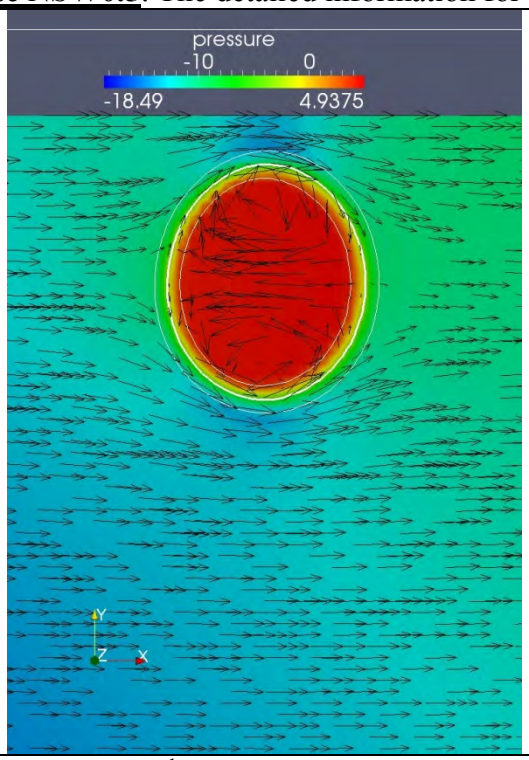

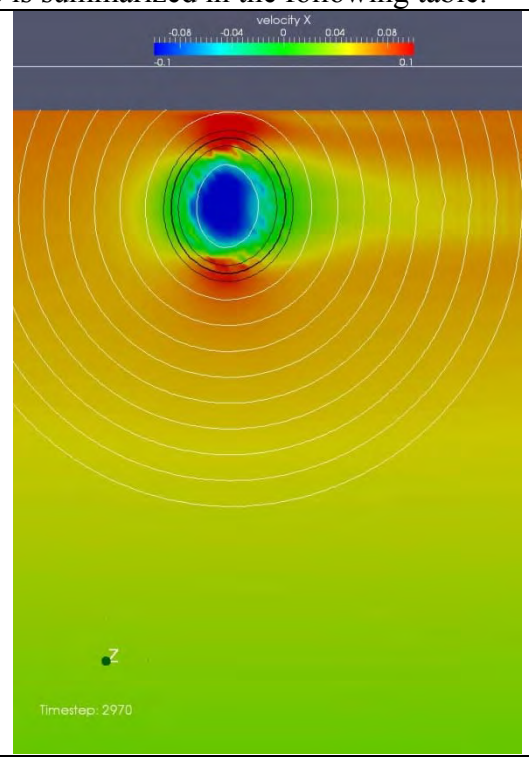

Shear rate: 2.0 s^{-1}
Relative velocity: 0.0675 m/s
Density: 996.5/1.161 (kg/m^3)
Viscosity: 8.5439E-04 (liquid); 1.858E-05 (gas)
Bubble diameter: 5 mm

Force estimate is over timestep range of: 1000 - 3000
Drag control force: 0.11850 N/kg
Lift control force: 0.08897 N/kg
Drag coefficient: 0.1440
Lift coefficient: 0.4888

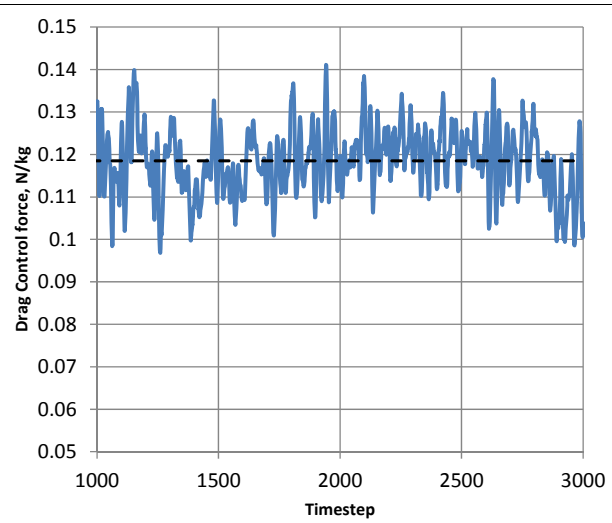

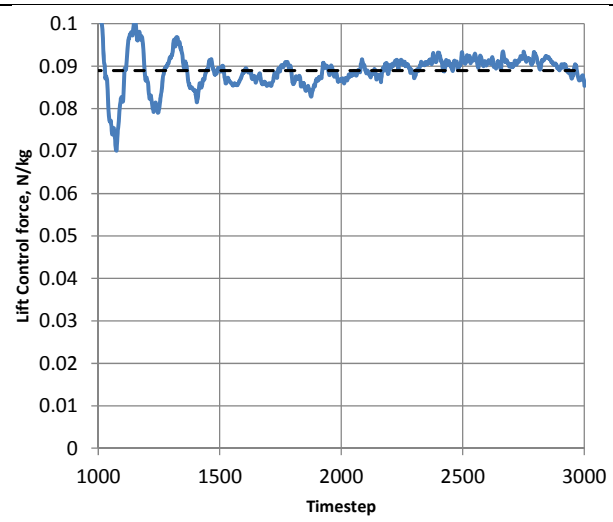

Figure 43. Summary of the NSW0.5 case with uniform shear of 2.0. Bubble is located half the radius from the top no-slip wall.

Case SW0.5: The detailed information for this case is summarized in the following table.

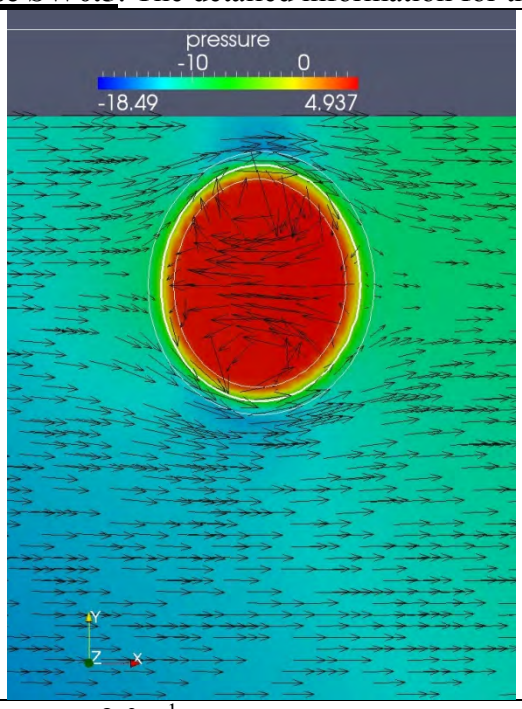

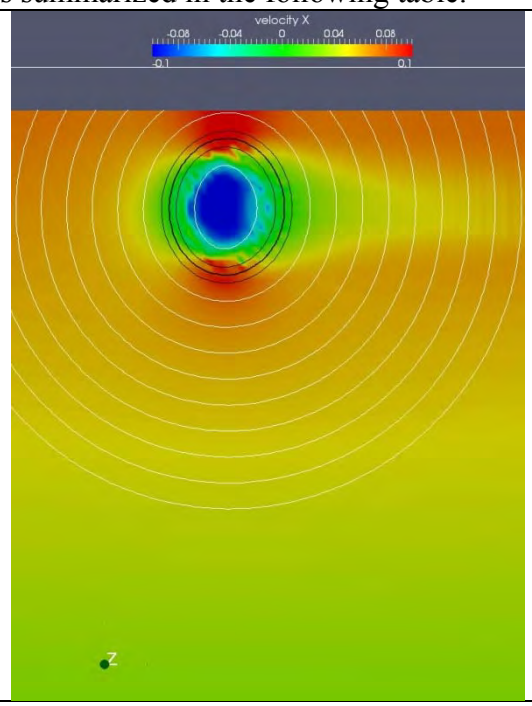

Shear rate: 2.0 s^{-1}
Relative velocity: 0.03375 m/s
Density: 996.5/1.161 (kg/m^3)
Viscosity: 8.5439E-04 (liquid); 1.858E-05 (gas)
Bubble diameter: 5 mm

Force estimate is over timestep range of: 1000 - 3000
Drag control force: 0.11308 N/kg
Lift control force: 0.08271 N/kg
Drag coefficient: 0.1374
Lift coefficient: 0.4544

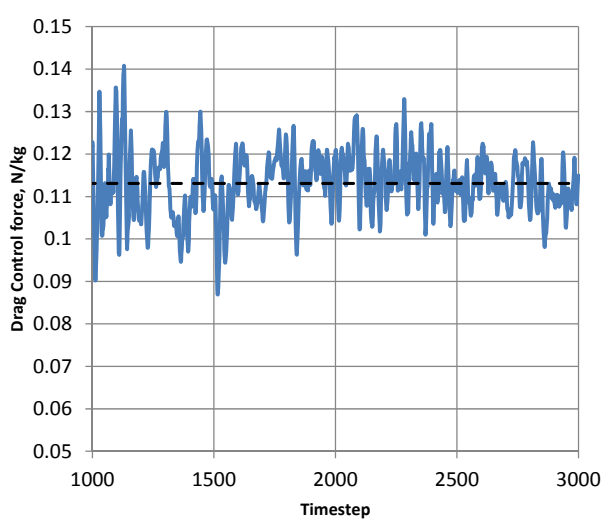

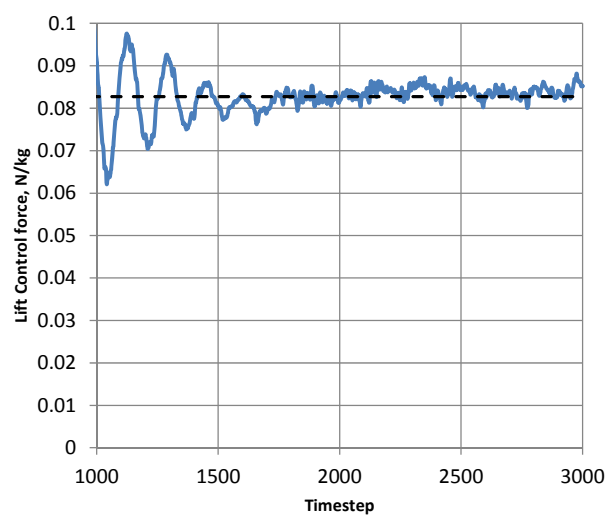

Figure 44. Summary of the SW0.5 case with uniform shear of 2.0. Bubble is located half the radius from the top free-slip wall.

Case ONSW0.5: The detailed information for this case is summarized in the following table.

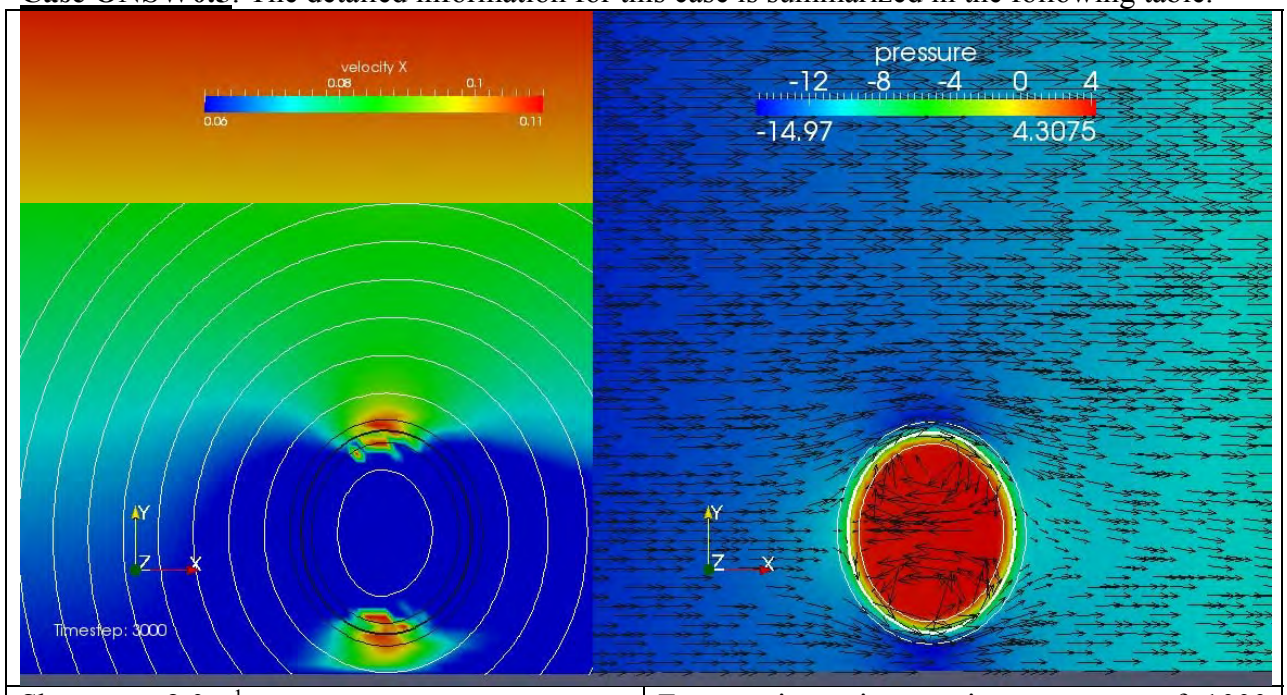

Shear rate: 2.0 s^{-1} Relative velocity: 0.0675 m/s Density: 996.5/1.161 (kg/m^3) Viscosity: 8.5439E-04 (liquid); 1.858E-05 (gas) Bubble diameter: 5 mm	Force estimate is over timestep range of: 1000 - 3000 Drag control force: 0.10350 N/kg Lift control force: 0.00350 N/kg Drag coefficient: 0.1258 Lift coefficient: 0.0192

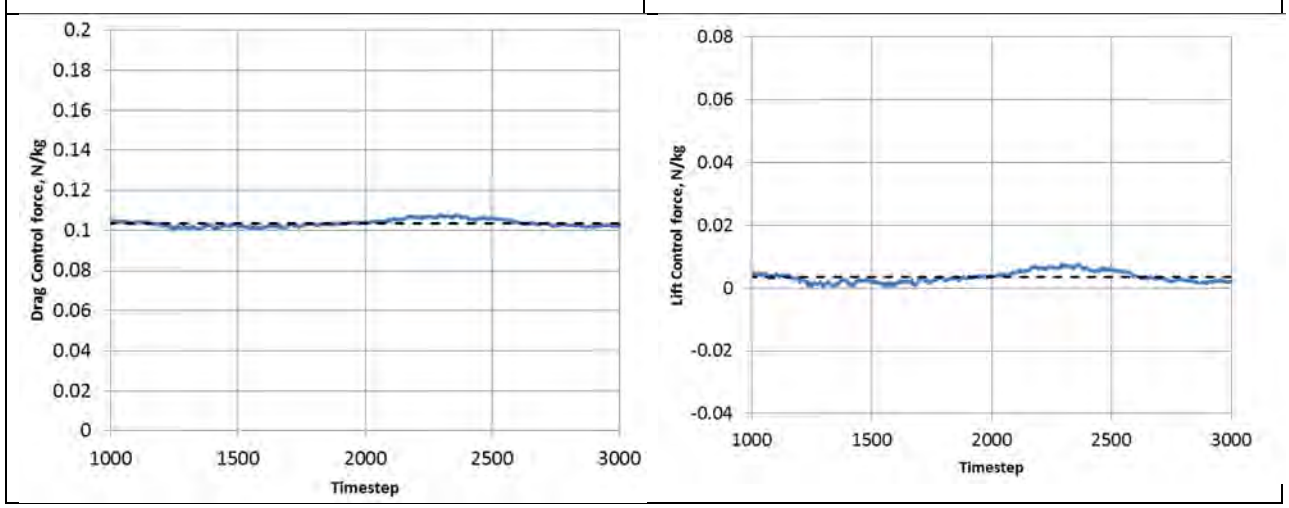

Figure 45. Summary of the ONSW0.5 case with uniform shear of 2.0. Bubble is located half the radius from the bottom no-slip wall.

By combining the results for the lift coefficient in the cases SW and NSW series, we can obtain the effect of the wall dependence, which is presented in Figure 46. Note, that the PHASTA case set-up effectively represents the downflow pattern, and thus the lift force pushes the bubble away from the "top" (faster moving) wall. This way as the bubble approaches the wall, the effect of wall proximity only increases the lift coefficient.

On the other side of the domain, the bubble experience the opposite effect (see cases "Opposite No-Slip Wall (ONSW)" – 1, 0.5 and 0.25. See Figure 45 for 0.5 distance example). We have summarized the observed lift coefficients as a function of the distance from the top wall in Figure 46. Note that the lift coefficient changes sign from positive to negative when the distance to the bottom wall goes from ½ bubble radius to ¼ radius. For the conditions under consideration, one can interpolate that the wall effect balances the lift force due to uniform shear at 3/8 bubble radius distance from the wall (e.g. the average lateral control force is expected to be near zero at this location). As can be seen from Figure 44, the control force demonstrates unstable behaviors, which represents bubble fluctuation near the wall. Note that there is a significant relative velocity of the bubble in our near wall simulations compared to those performed using FTC3D code (below).

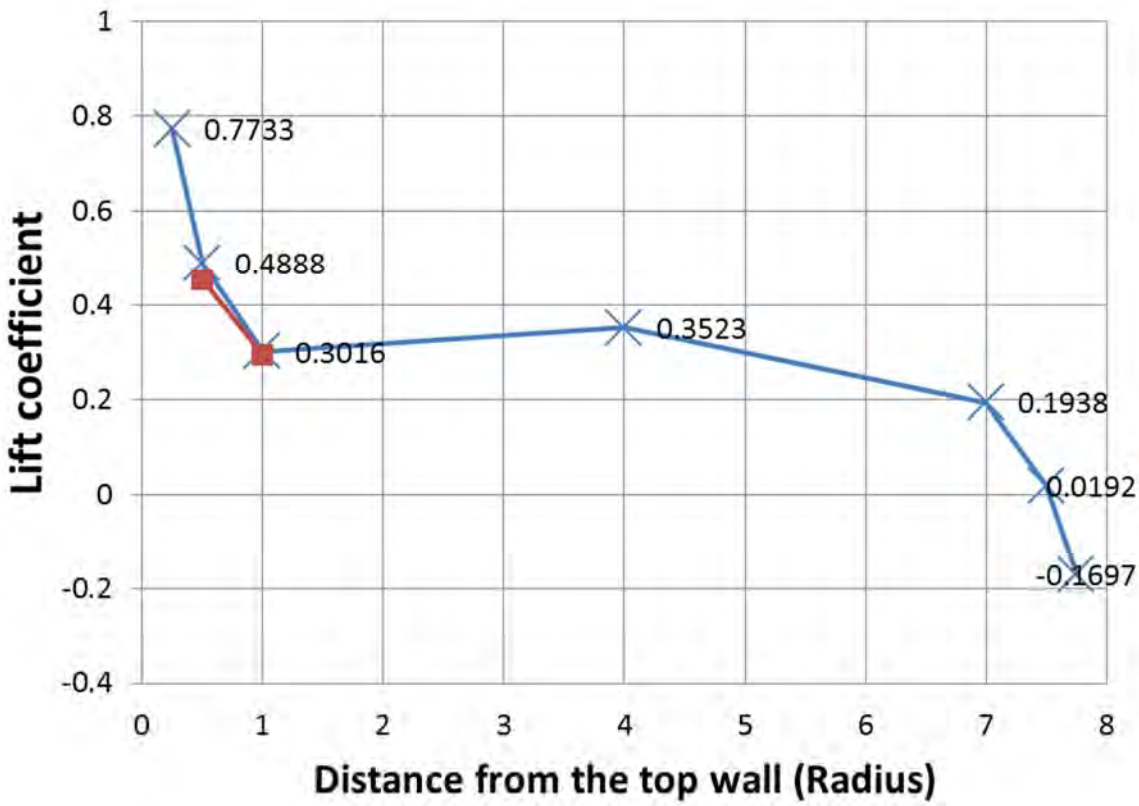

Figure 46. Lift coefficient dependence on the distance from the wall (measured in bubble radii from the closest point of the interface to the wall). Red line shows the slip-wall condition option.

Results for FTC3D simulations and measurements

Most of the computations done using the FTC3D code used a computational domain of size 0.5 x 0.5 x 0.25 resolved by a uniform grid of 80 x 80 x 40 points. Tests with larger domains and on finer grids, showed relatively minor changes as the domain size was increased. As discussed above, the inflow and the physical properties of the gas and the liquid were specified and the gravity acceleration in both the vertical and the horizontal direction adjusted using a PID controller to keep the bubble steady. The simulations have been run using "computational units," usually selected to be relatively close to unity. The results are then presented in dimensionless form, allowing for comparisons with physical variables. While several cases were examined, here we focus on those listed in Table 5. The deformability of the bubble was changed by changing the surface tension, the shear rate was changed by modifying the inlet and the vertical wall velocities. When the location of the bubble was changed, the inlet velocity was modified so that the slip velocity remained constant.

Figure 47 shows a nearly spherical bubble in a vertical shear flow after the flow has reached a steady state. The frame on the left shows a bubble in the middle of the channel and the frame on the right shows a bubble close to the right wall. The bubble and velocity field in a plane cutting through the bubble is shown by a quiver plot and the magnitude of the vertical velocity is shown by a color plot. In this case the surface tension is sufficiently high so the bubble remains nearly spherical. The outflow velocity is shown by arrows extending out of the domain at the bottom, where the wake of the bubble is clearly visible. The shear for the case with a bubble near the wall is smaller than for the case where the bubble is in the middle.

The gravity acceleration versus time, adjusted using a PID controller in such a way that the bubble remains stationary, is shown in Figure 48. The top frame shows the horizontal acceleration, which is balanced by the lift on the bubble, and the bottom frame shows the vertical acceleration which in balanced by the drag. By adjusting the gravity acceleration so that the bubble remains stationary, the slip velocity is determined by the velocity at the inlet, at the horizontal location of the bubble centroid. Both the vertical and horizontal acceleration initially overshoots its final value, but by adjusting the control parameters both components generally converge rapidly.

It is by now well known that the bubble deformability determines the lift force that acts on a bubble rising in vertical shear. A nearly spherical bubble rising near a wall in upflow is pushed toward the wall while a more deformable bubble is pushed away from it. This can have profound implications for the overall structure of the flow, affecting both the overall pressure drop and flow rate as well as the mixing that takes place. In Figure 49 we plot the lift and drag coefficients versus the Eotvos (Eo) number. While the drag coefficient increases rapidly with the deformability (increasing Eo), the lift coefficient decreases. The lift coefficient is positive for low Eo (lift toward the wall) and becomes negative as Eo increases. As Eo goes to zero, the lift coefficient levels off slightly and we would expect it, as well as the drag, to eventually become independent of the Eo. For the case examined the value for the lowest Eo is 0.365, which is slightly higher than the value reported by Tomiyama et al. (2002), but not by much. In general we find that as the bubbles become nearly spherical the lift coefficient is slightly above 0.3.
One of the key questions for bubbles in a shear flow is the dependency of the lift and drag coefficient on the shear rate. In Figure 50 the lift (a) and drag (b) coefficients are plotted versus

shear rate. For the shear rates examined here, the dependency is obviously weak. However, both fall off slightly as the shear rate increases, suggesting that it is important to examine higher values as well. For given physical parameters, stronger shear is likely to deform the bubbles more and that will reduce the lift and possibly the drag.

In Figure 51 we examine the effect of the distance to the wall on the lift (a) and drag (b) force on the bubbles. We show results for three sets of runs, where only difference is the value of the surface tension. The red curve is for the most deformable bubble and the black curve is for the least deformable one. When the bubbles are far from the wall they all experience a lift force pushing them to the wall, but as they come within about a diameter from the wall, the lift changes sign and pushes them away. As expected, the most deformable bubbles has the highest drag and lowest lift, when it is in the middle of the channel, but as it is moved closer to the wall the force pushing the deformable bubble is pushed away from the wall is higher. Notice that the deformable bubble "feels" the wall earlier than the more rigid ones. The drag force on the bubbles increases as they are moved to the wall but the deformable bubble continues to experience the largest drag.

The Reynolds number for the cases shown here have been relatively modest. We have also examined higher Reynolds numbers, both by changing the viscosity or the inflow velocity. As the Reynolds number increases the time to reach a steady state increases, but our results so far indicate that they will eventually settle down. It is also possible that the transient can be shortened by a different selection of the control parameters. Figure 52 shows the lift (a) and drag (b) force on the bubbles versus distance to the wall. While the results are similar to the lower Reynolds number case in Figure 51, here we see that the lift and the drag forces remains essentially constant until the bubble is very close to the wall. The drag coefficient is also lower, as expected.

Table 5. The various parameters used for the FTC3D baseline case.

Viscosity (Fluid/Bubble)	0.01 / 0.001
Wall Velocity	Vwest = -2.0 Veast = -3.0
Shear Reynolds Number G_R	2.0
Relative velocity of bubble	2.5
Bubble's Reynolds Number Re_b	**25.0**
Capillary Number Ca	0.004
Mean x-force	-1.45
Mean y-force	86.72
Froud Number Squared Fr^2	0.00461
Eotvos Number Eo	1.69
Morton Number M	6.76e-6
LogM	-5.17
Lift coefficient	**0.283**
Drag Coefficient	**1.803**

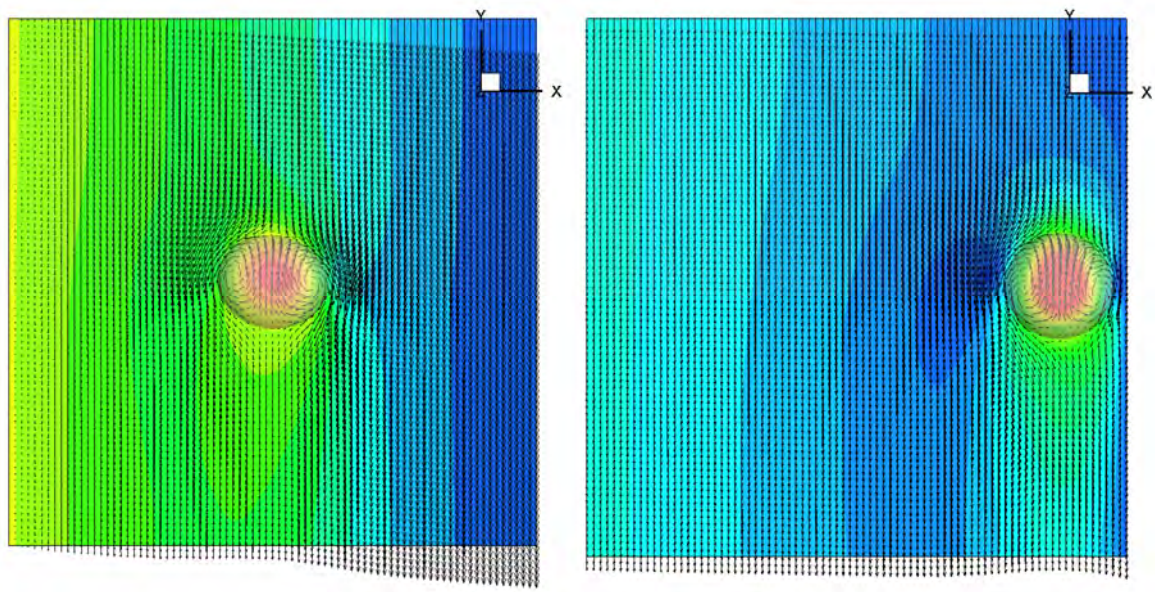

Figure 47. The bubble and the velocity field shown by a quiver plot. The color indicates the vertical velocity component. In the left frame the bubble is in the middle of the domain and in the right frame the bubble is close to the right wall.

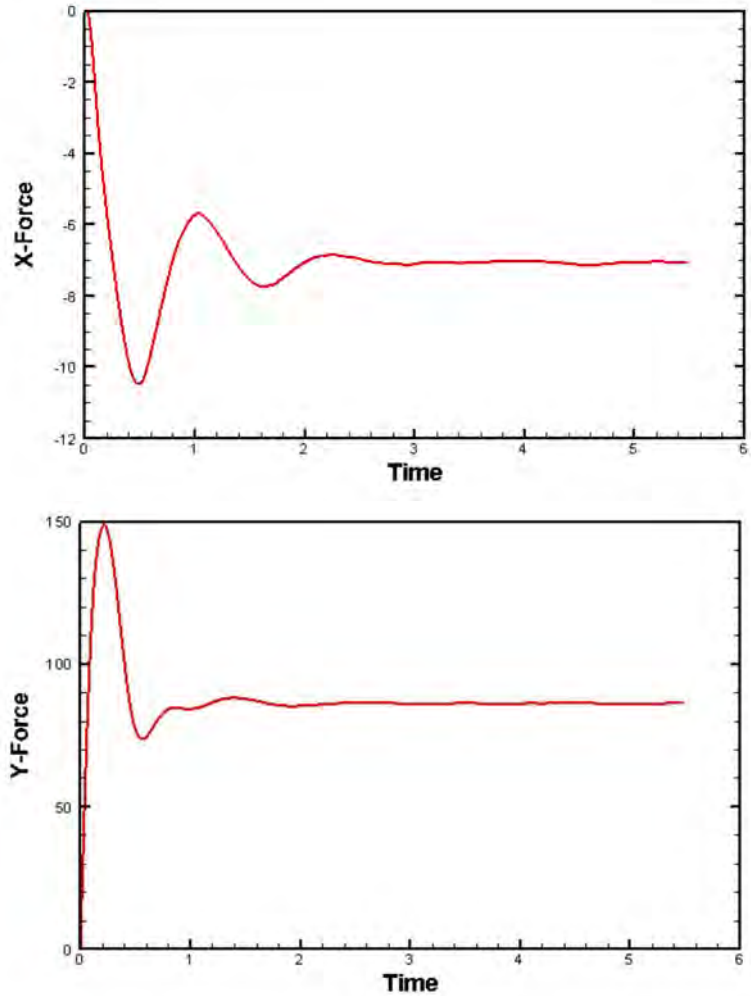

Figure 48. The horizontal (top) and the vertical (bottom) component of the gravitational acceleration versus time, as adjusted by the PID controllers to keep the bubble stationary.

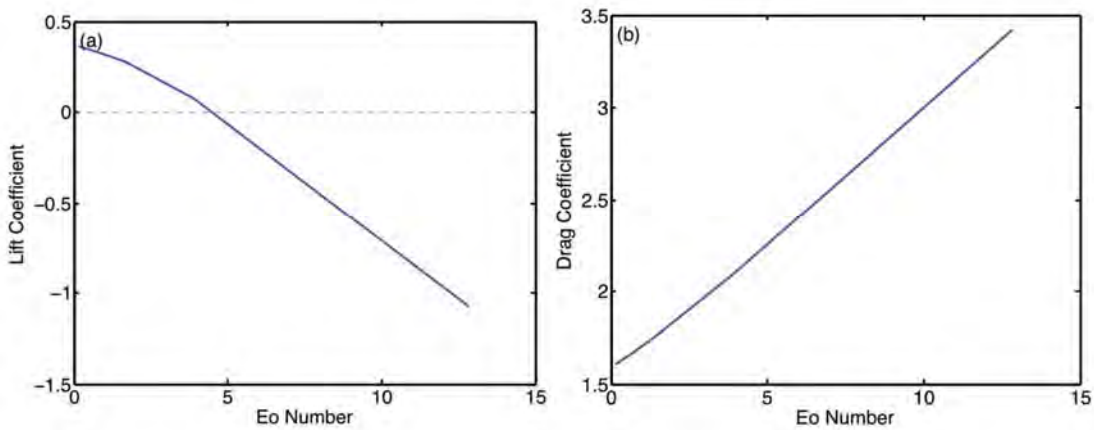

Figure 49. The lift and drag coefficients versus the Eotvos (Eo) number

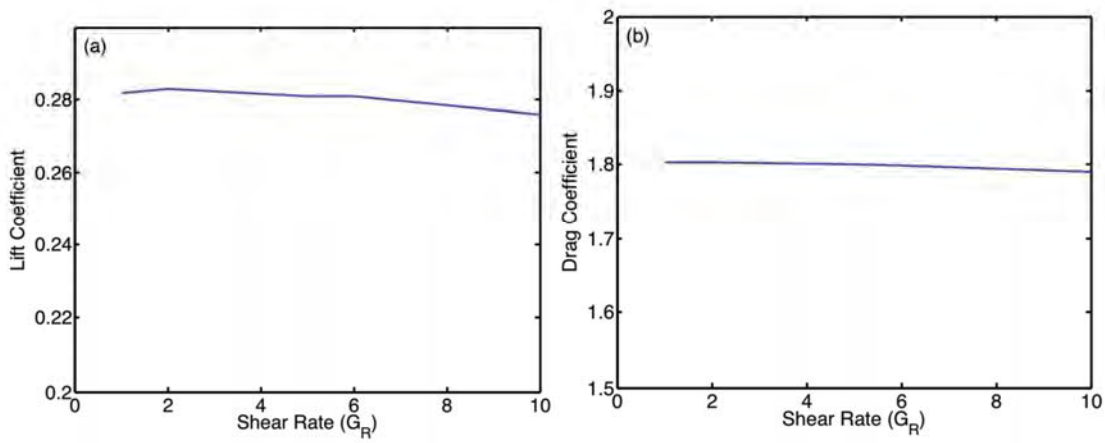

Figure 50. The lift (a) and drag (b) coefficient versus shear rate.

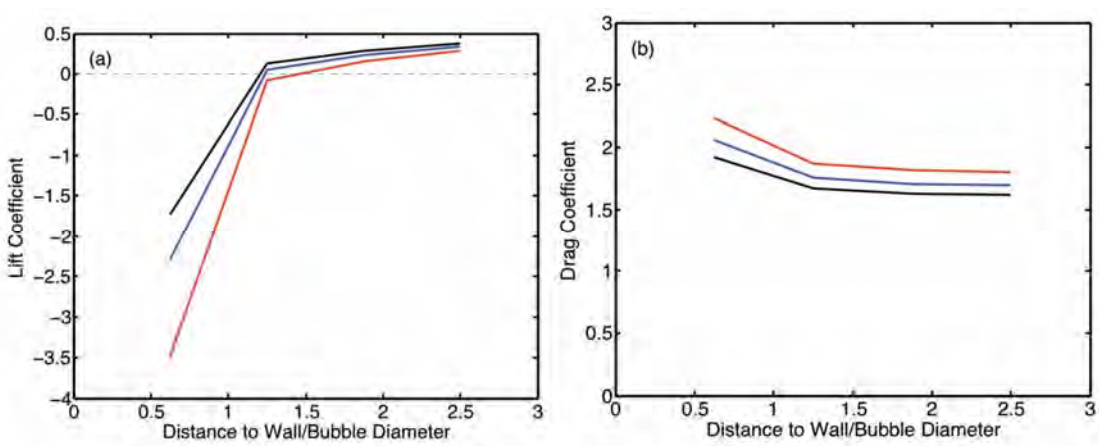

Figure 51. The effect of the distance to the wall on the lift (a) and drag (b) force on the bubbles.

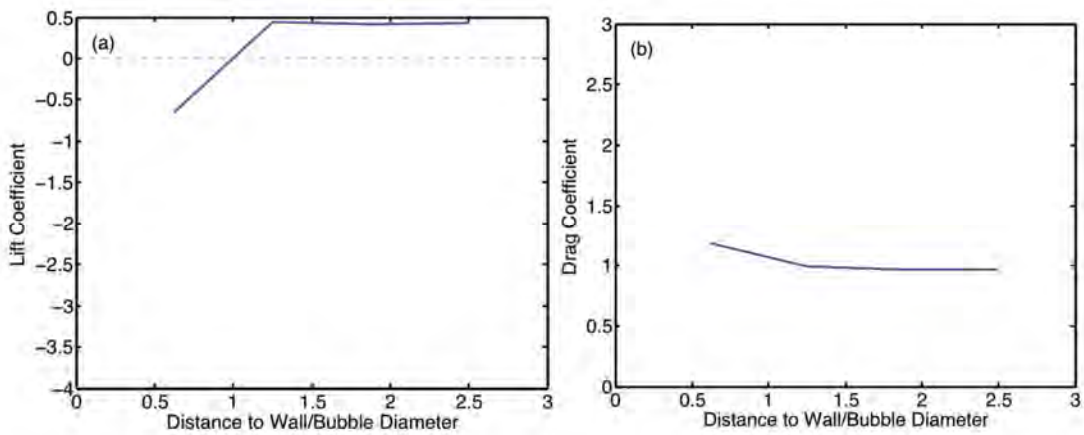

Figure 52. The effect of the distance to the wall on the lift (a) and drag (b) force on the bubbles for a bubble Reynolds number = 50.

Future Work

The results shown here suggest that the strategy used here to obtain the lift and drag on individual bubbles is reasonably effective. However, two issues have emerged that we expect to address in a follow-on study:

- The current setup, where the inflow is specified and we apply outflow boundary conditions at the bottom boundary, limits the amount of shear that we can examine, since the outflow boundary conditions are not designed for backflow thorough the outflow boundary. We believe that we can overcome this limitation by specifying the flow profile at the outflow boundary and using a longer computational domain to limit the effect of the boundary on the wake. This was demonstrated for some of the presented case using PHASTA code: SW5, SW10 and SW50 (including negative inflow velocity profile to maintain low relative velocity at high shear rate).
- The current approach to keep the vertical position of the bubble in the middle of the computational domain by adjusting the vertical gravitational acceleration results in a change in the various nondimensional numbers that control the flow when the horizontal location is changed. The Reynolds number is constant, but the more physical situation is if the Reynolds number varies but the Eotvos and the Morton number stay the same. We should be able to do so by using a sliding domain that moves with the bubble. That would allow us to fix the value of the vertical gravitational component and adjust only the horizontal one.

4. HYDRA-TH MULTIPHASE FLOW

This section summarizes the work performed under three supporting L3 milestones focused on developing a multiphase flow capability in Hydra-TH. These milestones include the development of the underlying code-infrastructure in Hydra-TH for handling multiple mass, momentum and energy equations (L3:THM.CFD.P6.01), and on-going work involving fully-implicit solution algorithms, and closures for interphase exchange (L3:THM.CFD.P8.01). In addition, work to develop a general-purpose steam-table library that will find broad application in the Thermal-Hydraulics Methods (THM) focus area is briefly described (L3:THM.CFD.P7.04). Finally, a series of computations are presented to demonstrate the existing multiphase flow capabilities as currently implemented in Hydra-TH.

4.1 The Multiphase Development Plan

Before embarking on the multiphase flow development in Hydra-TH, a comprehensive literature survey of existing research and commercial multiphase codes and their solution algorithms was conducted. The codes surveyed included NPHASE, NEPTUNE, CATHARE, STAR-CD, STAR-CCM+, FLUENT, CFX, MFIX, CFDLib, TRAC, TRACE, RELAP5, RETRAN, etc. Based on this work, a series of requirements for the multiphase flow solver have been developed as shown below.

Hydra-TH Multiphase Requirements and Design Principles:

- User-specified multi-(N)-fluid formulation
- (Discrete) mass, momentum and energy conservation
- Ability to treat all flow speeds, from nearly incompressible to fully compressible and stiff interphase coupling terms
- Ability to deal with numerical stiff fluid (water) equation of state
- Robust treatment of phase appearance and disappearance
- Ability to deal with boiling/condensation (tight coupling with energy conservation)
- In the limit of a single phase, the solution algorithm should reduce to the original Hydra-TH solution algorithm which has proven to be robust, efficient and accurate
- Address solvability, i.e., hyperbolicity and well-posedness
- Efficient for large-scale unstructured-mesh HPC applications, i.e., scalable
- Permit tight-coupling with next-generation system analysis codes

Based on the survey, it was determined that most of the existing multiphase flow solvers rely on a single-pressure approximation and are very similar in terms of the ensemble-averaged multiphase equations they are attempting to solve and the closure models they use. Essentially all use a “single-pressure” approximation with various “fix-up” strategies that include accounting for bulk-pressure differences, interface dynamic pressures, added mass, etc. At this time, most of the codes are based on some form of the SIMPLE (Semi-Implicit Pressure-Linked Equations) algorithm, although some like NPHASE combine a SIMPLE-like outer iteration with a coupled mass-momentum solution strategy. Based on our survey, these algorithms tend to exhibit relatively slow convergence properties (e.g., 100’s of iterations for small problems). In addition,

all current workhorse codes, e.g., RELAP5, TRAC, TRACE, CATHARE, RETRAN, use an operator-split algorithm.

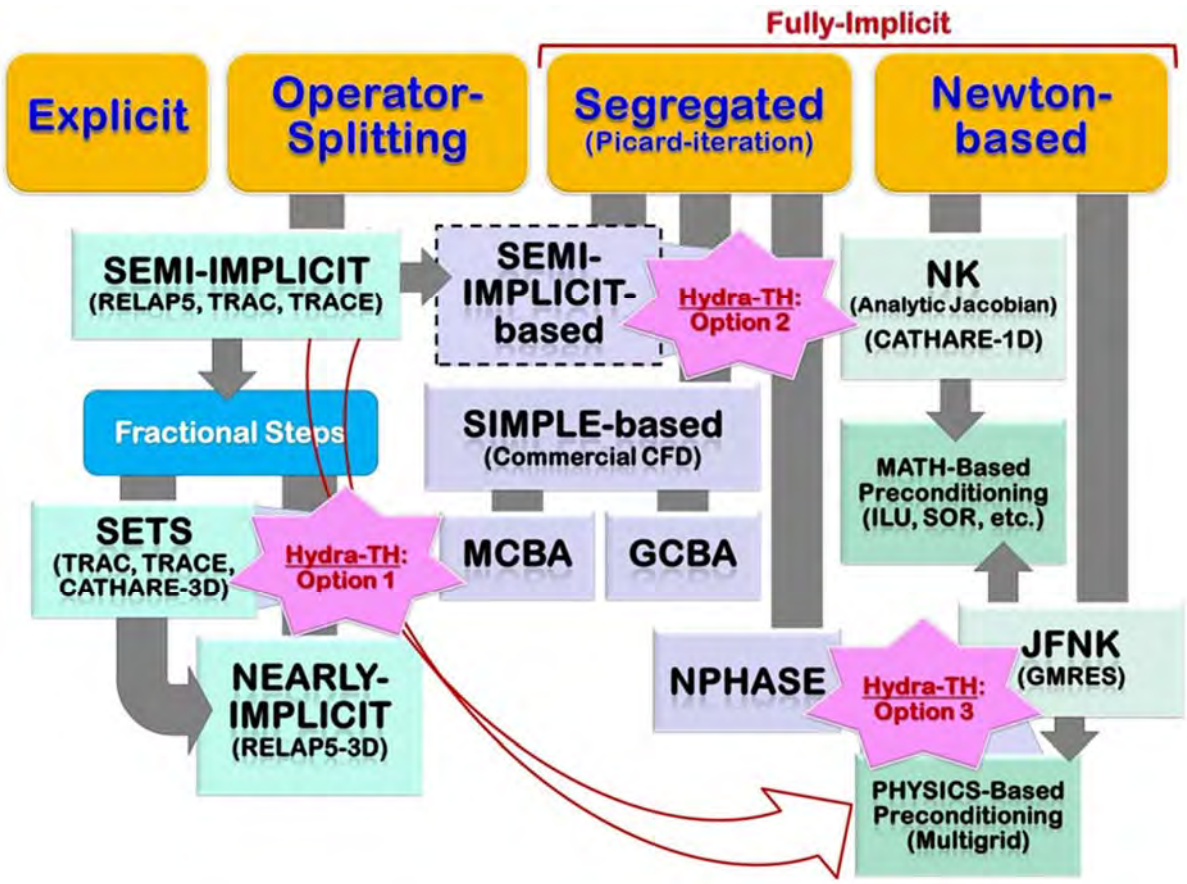

Figure 53: Diagram of codes, solution methods and Hydra-TH development stages.

Based on our survey, a staged implementation plan was adopted with increasing levels of complexity balanced with the development of the necessary code infrastructure for multiphase problems. This plan is reflected in Figure 53 as Hydra-TH Option-1, 2 and 3. A brief outline of the multiphase solution algorithm development associated with three options is presented below.

4.2 Multiphase Flow Algorithms

The initial phase of development has focused on an inelastic formulation ($\nabla \cdot \rho v = 0$) that admits weak compressibility in the overall multiphase mixture, e.g., compressibility due to the presence of bubbles. This algorithm has been implemented with the initial multiphase infrastructure in Hydra-TH and the details of this algorithm may be found in [60]. This algorithm is unique in that it admits the treatment of large density differences, e.g., 1000:1 for water and air, while retaining a simple form of the pressure-Poisson equation. This algorithm was chosen for its robustness, and the ability to recover the single-phase projection algorithm used in Hydra-TH. This formulation is being used essentially as a test-bed and platform for the

implementation/testing of various lift and drag force closures while the final work on the fully-implicit algorithms identified as "Option-2/Option-3" in Figure 53 progresses.

4.2.1 Fully-Implicit Algorithms

Development of the fully-implicit projection algorithm for single-phase flows has been carried out in parallel with the "Option-1" multiphase development. This effort is focused on two primary objectives: a fully-implicit steady-state/slow-transient capability, and the implementation of the Option-2/Option-3 multiphase solvers. The details of the fully-implicit solution algorithm may be found in [57, 58].

In order to illustrate the behavior of the fully-implicit solution strategy, a thermal-convective transient problem was selected. The problem consists of a square cavity with adiabatic walls on the top/bottom of the cavity, a fixed cold temperature on the right wall, and a time-dependent temperature boundary condition on the left wall as shown in Figure 54. The fluid is initially stationary with $Ra = 10^4, Pr = 0.71$. A mesh resolution of 320x320 cells was used.

Figure 55 shows the convergence history of the normalized global residual during a sequence of five time-steps in the simulation of the differentially-heated cavity. A reduction of about 8 decades is achieved in 8 non-linear iterations with convergence rates that are first-order for the fully-coupled system of equations. The temporal convergence rates for velocity (kinetic energy), temperature and the Lagrange multiplier, i.e., the pressure increment are shown in Figure 56. Second-order accuracy in temperature and velocity are observed with third-order accuracy in the Lagrange multiplier. While the Hydra-TH semi-implicit projection algorithm provides about a 10X increase in the time-step over traditional Godunov-Projection methods, the fully-implicit algorithm enjoys unconditional stability, albeit at the cost of non-linear iteration for each time step.

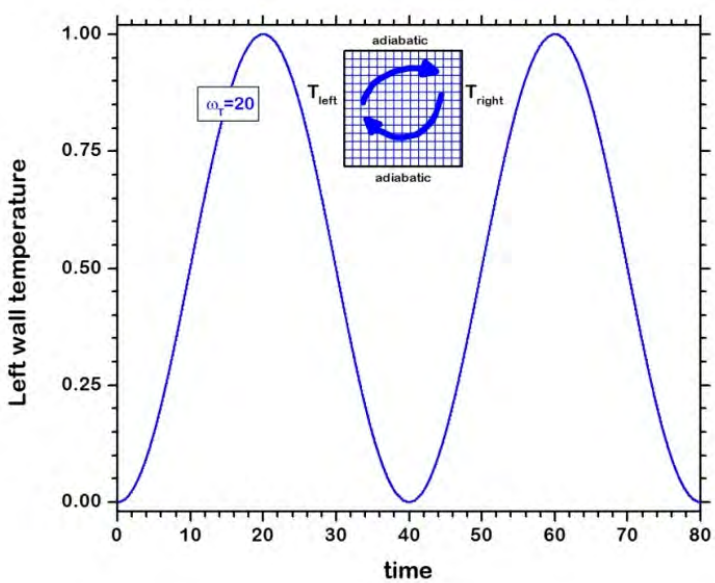

Figure 54: Time-dependent differentially heated cavity problem.

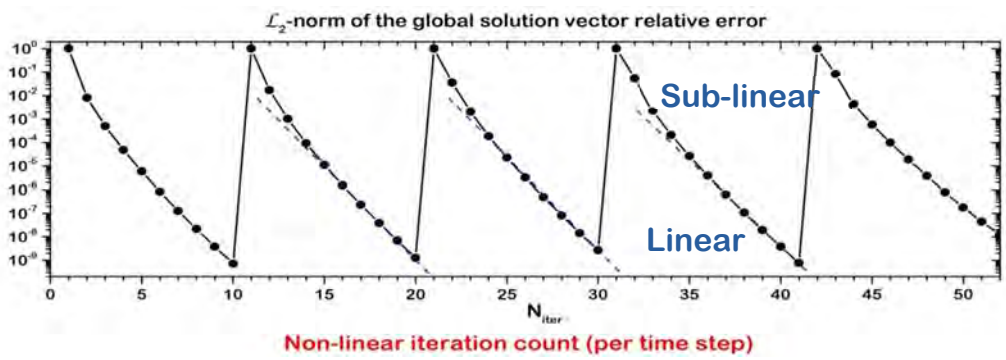

Figure 55: Convergence history during multiple time-steps.

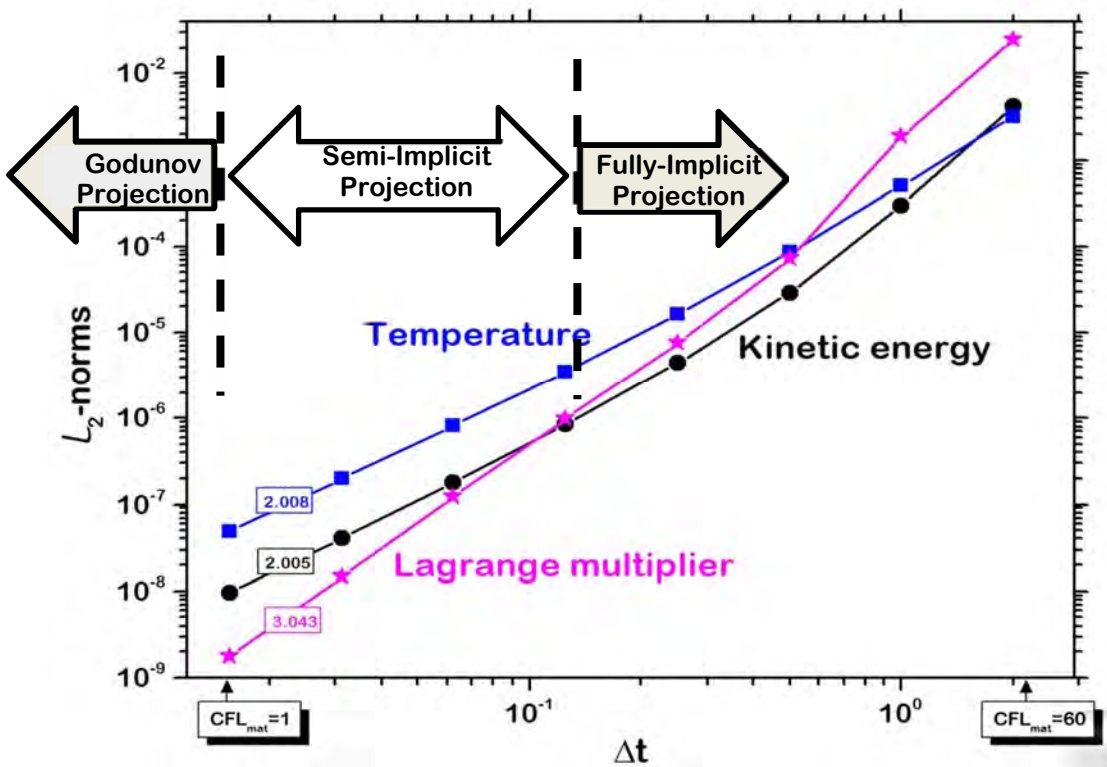

Figure 56: Temporal convergence rates and algorithmic domains for projection methods.

The effectiveness of the fully-implicit projection algorithm was further assessed in terms of the order of convergence and rate of convergence relative to two well-known solution algorithms that are used in research and commercial CFD codes. A $Re = 100$ flow past a circular cylinder was used for the comparison. This flow exhibits a single unstable mode associated with a Hopf bifurcation resulting in the classical Karman vortex street. For this study, OpenFoam was used with modifications that permit the measurement of the residual norms associated with the SIMPLE and PISO solution algorithms. Figure 57 shows snapshots of the instantaneous velocity magnitude for $3.5 \leq CFL \leq 60$. We note that the fully-implicit projection algorithm preserves the vortex street up to $CFL = 60$, a factor 60 increase over a Godunov-type projection method. In addition, while the SIMPLE and PISO algorithms converged at $CFL = 35$, the damping in these solution methods destroyed the vortex street. Here, it appears that the SIMPLE and PISO implementations in OpenFoam require a $CFL < 7$ to preserve any sort of coherent vortex street.

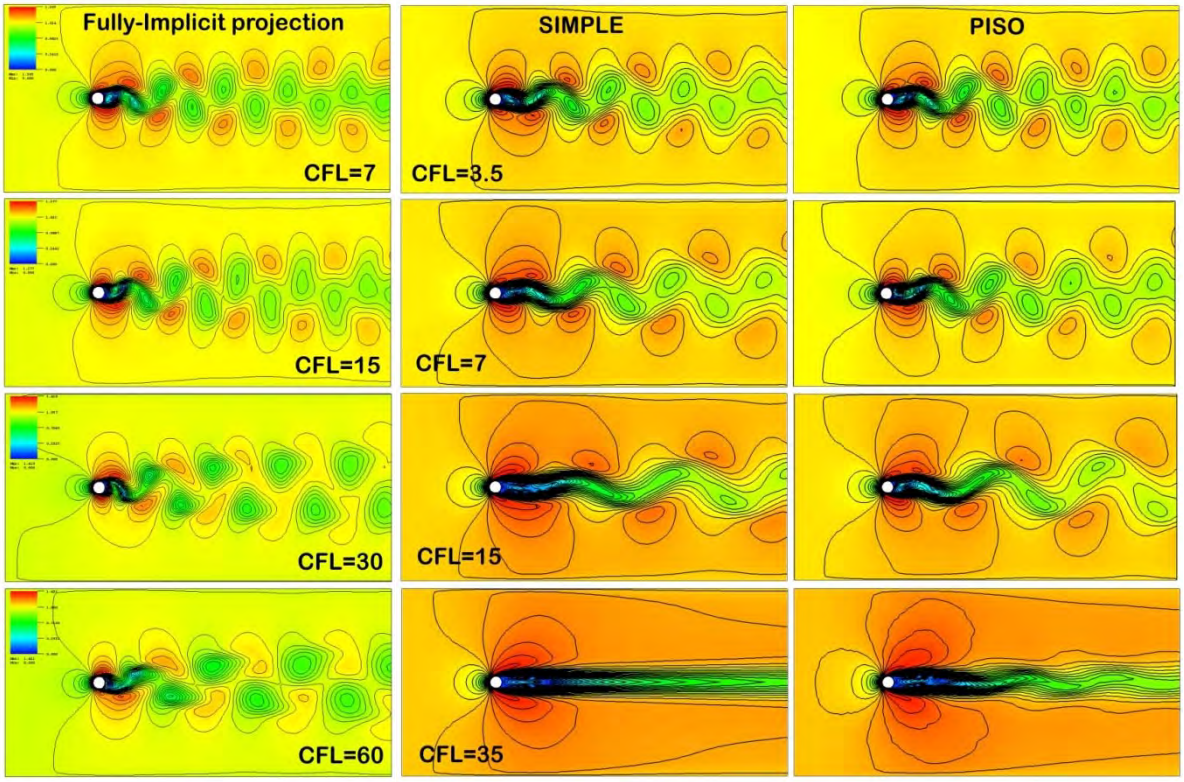

Figure 57: Re=100 flow past a cylinder with $3.5 \leq CFL \leq 60$.

In order to understand the nonlinear convergence properties of the fully-implicit projection methods, the order and rate of convergence were measured for the vortex-shedding problem. The order of convergence is defined in terms of the global residual norm $\|\epsilon\|$ as

$$r = \frac{ln\|\epsilon^{n+1}\| - ln\|\epsilon^{n}\|}{ln\|\epsilon^{n}\| - ln\|\epsilon^{n-1}\|} \qquad 4.1$$

The convergence rate is defined as

$$C^r = \lim_{n\to\infty} \frac{ln\|\epsilon^{n+1}\|}{ln\|\epsilon^{n}\|^r} \qquad 4.2$$

Figure 58 shows the convergence rates for a sequence of time-steps during vortex shedding for the fully-implicit projection and PISO algorithms. The convergence rates were measured at $CFL = 7$ and $CFL = 60$. Both algorithms yield an order of convergence of 1. The fully-implicit projection method remains convergent under iteration with relatively well-behaved convergence histories. In contrast, the PISO algorithm asymptotes to a convergence rate near 1.0 indicating stagnation and an inability to reduce the global errors in residual beyond a given point. Rates above 1 correspond a divergent non-linear iteration.

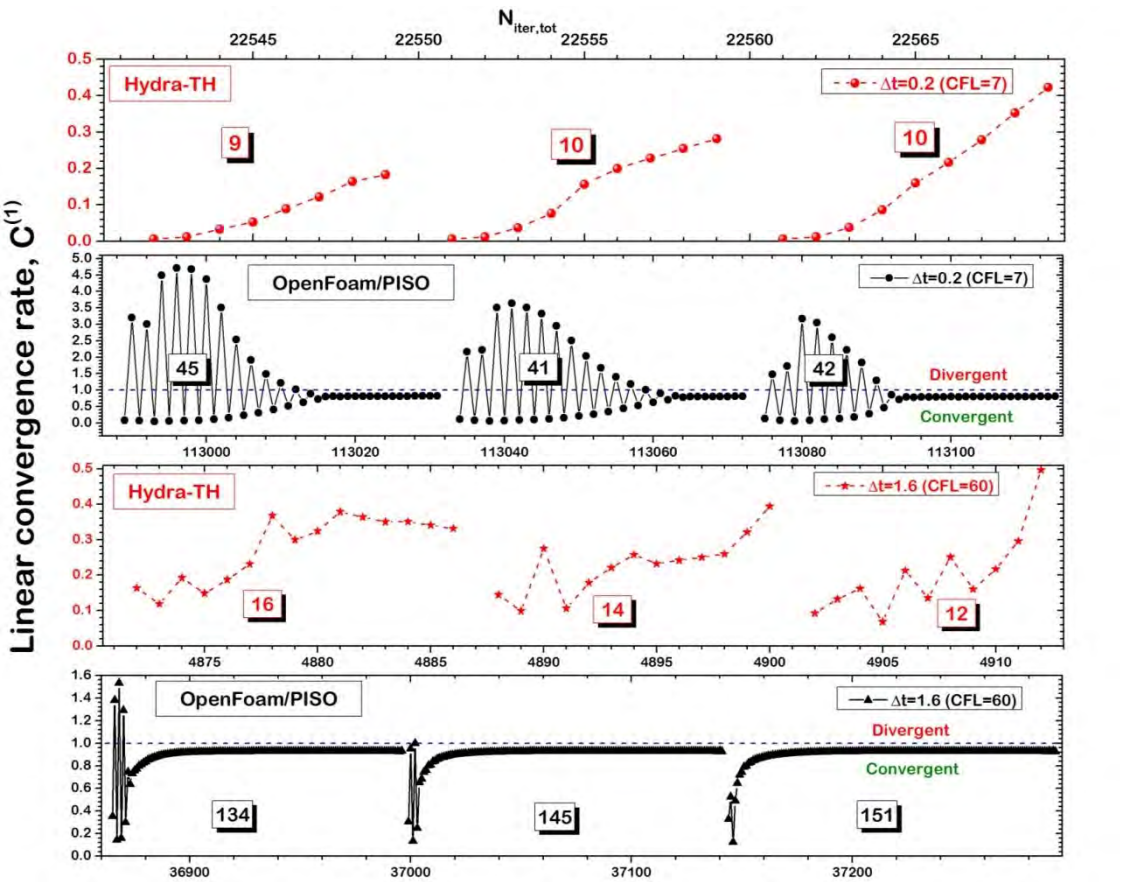

Figure 58: Convergence rates for fully-implicit projection and PISO algorithms.

Finally, a timing comparison for the PISO and fully-implicit projection algorithm was performed. We note here that we made no effort to compare the performance various components of the solution algorithm, e.g., linear algebra, but simply timed the fully-implicit algorithm in Hydra-TH and the corresponding PISO algorithm in OpenFoam. The results shown in Table 6 indicate that the fully-implicit projection method is a factor of 1.78 to 2.57 faster than the corresponding PISO algorithm for equivalent convergence criteria.

Table 6: Timing comparison between the fully-implicit projection algorithm in Hydra-TH and PISO in OpenFoam. A 2.66 GHz i7 processor was used for this comparison.

Method	*CFL*	CPU [sec.]	Ratio
PISO	7	11,750	1.78
Fully-Implicit Projection	7	6,584	--
PISO	60	3,208	2.57
Fully-Implicit Projection	60	1,249	--

4.2.2 Fully-Coupled Momentum Exchange

The treatment of the interphase exchange terms is critical to faithfully simulating the physics involved in multiphase flow. Here, we report on one important aspect associated with momentum exchange. In order to preserve anti-symmetry in the interphase drag forces, an

algorithm that is coupled across phasic momentum is required. Note that preserving the anti-symmetry corresponds to conserving momentum across all phases.

Following the work done with the CartaBlanca code [61], and recommendations by Duan Zhang [62], we have adopted an element-by-element (EBE) fully-coupled update procedure for momentum exchange. This can be easily integrated in both the semi-implicit and fully-implicit multiphase algorithms and used with either Picard or Newton-Krylov iterative procedures. Further, the EBE momentum exchange is very computationally efficient, involves only cell-local data, and may be extended to the mass and energy exchange.

In order to assess the momentum conservation, a series of interphase drag tests have been conducted with varying phasic volume fractions, bubble diameters, and number of phases. The basic problem is shown in Figure 59. Here, $Re = 100$ based on the channel height, and an initial liquid (carrier) phase velocity of unity is used. The second and additional phasic velocities are all specified to be zero. No-penetration conditions at the top/bottom walls. The interphase drag will act to accelerate the second phase until the two fluids are moving at a constant velocity. For equal density and equal initial volume fractions, the velocity is expected to asymptote to approximately one half of the initial carrier velocity. For all computations, a constant interphase drag coefficient, $C_d = 0.44$, was used.

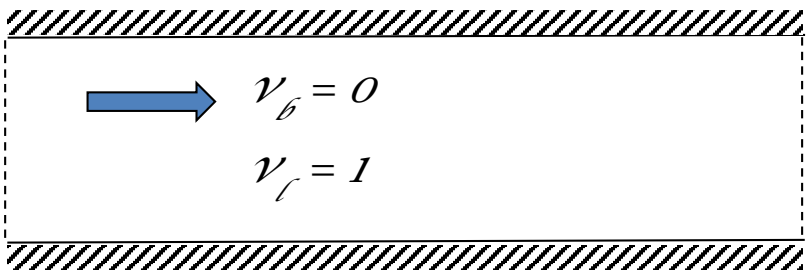

Figure 59: Drag force verification problem.

Figure 60 shows the asymptotic phasic velocity when the drag force is applied in the x, y and z-coordinate direction. As expected, the asymptotic phasic velocities approach one-half the imposed carrier velocity. Because the phasic velocities are fully-coupled, there is no dependence on spatial direction, and momentum is conserved by inspection. Figure 61 shows the asymptotic phasic velocities for a 5-field problem where each phase has a volume fraction of 0.2. The initial velocities range from zero to 1.0 increasing with each phase by 0.25. Again, momentum is conserved by inspection, and the phasic velocities asymptote to a value of 0.5. Figure 62 shows the effect of varying the bubble diameter on the evolution of the drag force. Here, the bubble diameter varied from 10^{-3} to 10^{-1} normalized with respect to the channel height. As the drag force varies inversely with the bubble diameter, the larger bubbles take longer to accelerate to the asymptotic phasic velocity. Figure 63 shows the effect of non-equal volume fractions on the asymptotic velocity. Here, increasing the carrier volume fraction increases the asymptotic phasic velocity proportionally as expected.

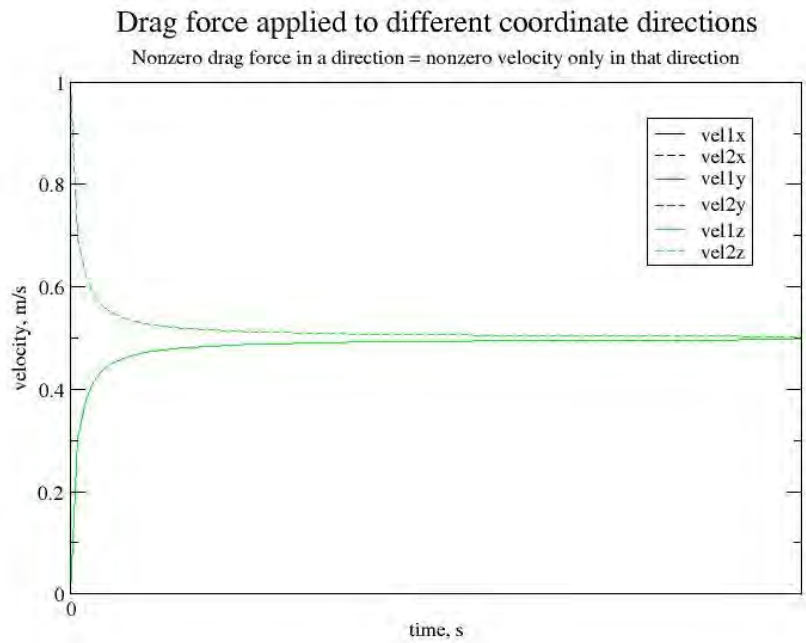

Figure 60: Asymptotic phasic velocities for drag acting in the x, y and z-coordinate directions.

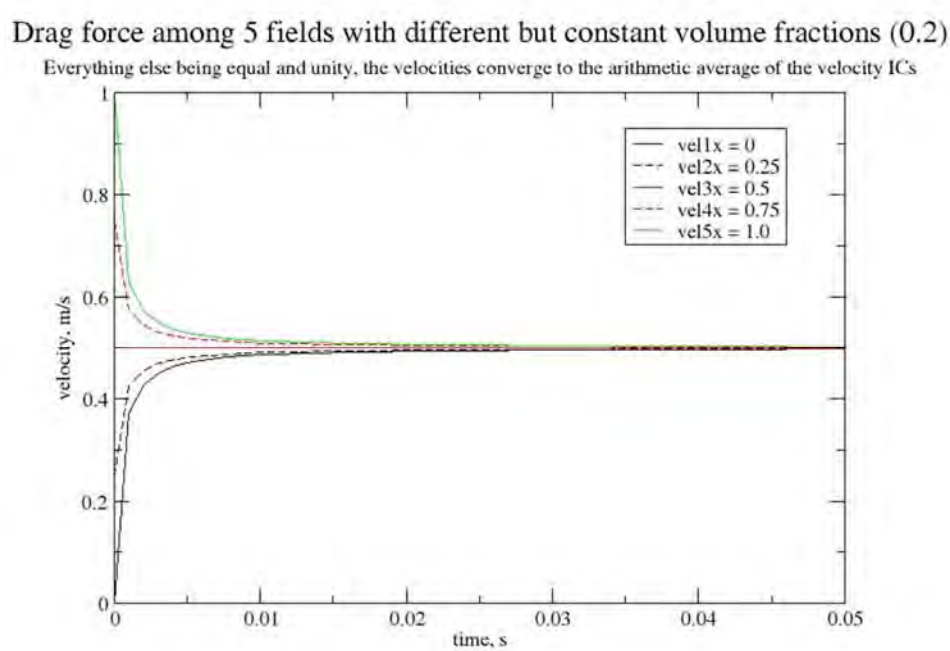

Figure 61: Asymptotic drag test for 5-fields with equal volume fractions.

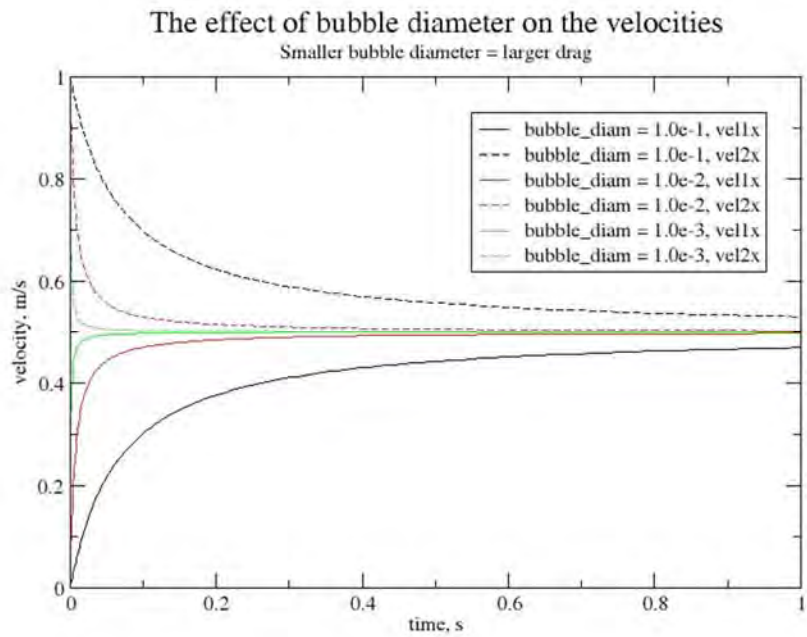

Figure 62: Effect of bubble diameter on phasic velocity.

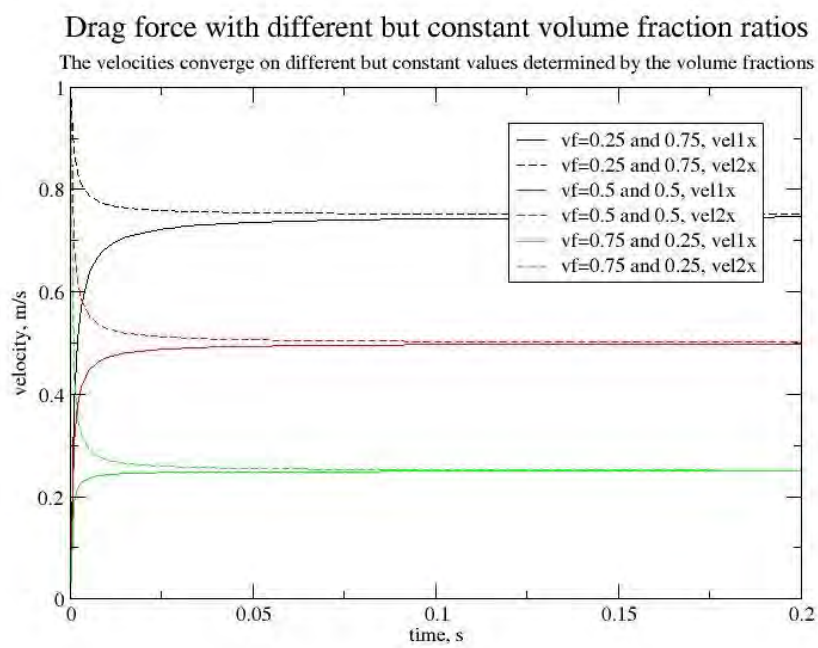

Figure 63: Effect of varying volume fraction on the asymptotic velocity.

Having demonstrated momentum conservation in the EBE momentum exchange algorithm, we turn to a verification of the terminal bubble velocity. This problem is defined by prescribing a zero pressure gradient along with the no-normal penetration conditions as shown in Figure 59. Here, both fluids are inviscid so that the only dissipative mechanism is the interphase drag. A constant drag coefficient is used, $C_d = 0.44$, and both fluids are initially at rest. A bubble volume fraction of 0.001 is used in conjunction with a liquid/bubble density ratio of 100:1. This set of conditions results in the bubble phase accelerating due to a fixed body force. At steady-state, the body force exactly balances the interphase drag. As shown in Figure 64, the bubble velocity asymptotes to the analytical value for a single bubble under a constant body force.

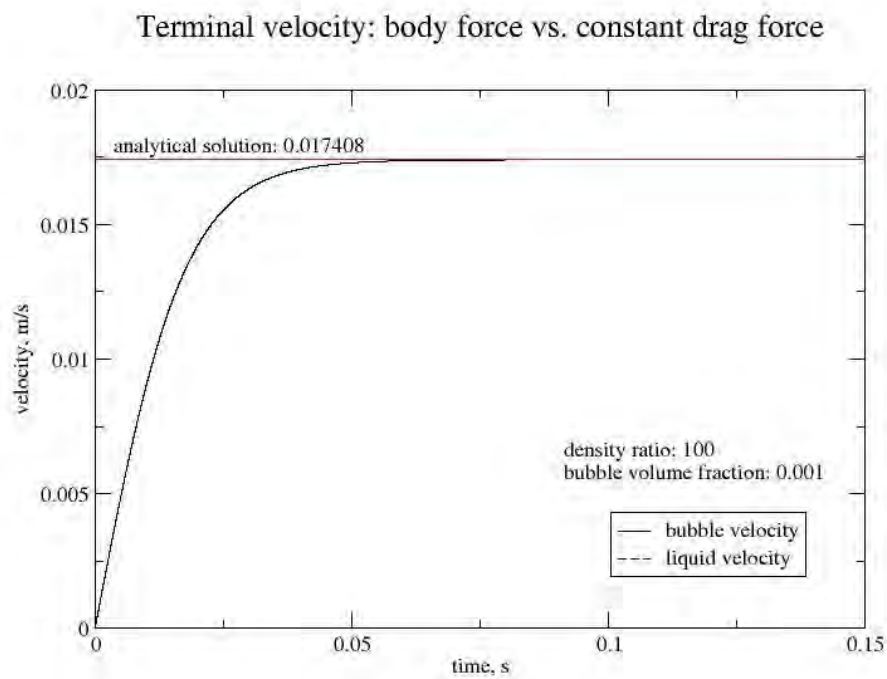

Figure 64: Terminal velocity verification problem.

4.3 General Purpose Library for Steam Properties

Accurate material properties are key for predictive simulation capabilities. They provide closure for the various algorithmic formulations, such as the multiphase algorithms described above. For the boiling problem, in particular, the thermodynamic and transport properties of water, or steam, must be provided. Evaluation of these properties may contribute significantly to the time required for a solve of the compressibility equations. Efficent formulations for property look-ups are thus important for large scale calculations. To this end, tabulated values are often used instead of analytic relations. The following sections describe the chosen analytic models for water and their tabulation for use in Hydra-TH.

4.3.1 Water Property Models

The International Association for the Properties of Water and Steam (IAPWS) has created and published multiple models for the thermodynamic and transport properties of water. The models are analytic formulas based upon polynomial expansions of free energies in density, temperature, and pressure. The many parameters of these expansions are calibrated to the various experimental measurements available for water. The four IAPWS standards used for this work are the 2009 revision of the 1995 formulation for the thermodynamic properties of water (IAPWS95) [10,11], the 2007 revision of the 1997 industrial formulation (IAPWS-IF97) [12,13], the 2008 formulation for viscosity (Visc08) [14,15], and the 2011 formulation for thermal conductivity (Thcon11) [16,17].

Validation of all four models is detailed in their respective references. They models typically agree well with all the available data, except near the critical point. Furthermore, the Visc08 and THcon11 models use thermodynamic properties to compute their respective transport quantities. They have been originally developed to use the IAPWS95 model, but can also use the IAPWS-IF97 formulation with some reduced accuracy. To keep consistency, when tabulating one of the thermodynamic models, the same model is used to compute transport properties. The loss of accuracy arises due to the slight differences between the IAPWS95 and IAPWS-IF97 formulations. IAPWS-IF97 was developed to use simpler analytic expressions which reproduce the IAPWS95 model as closely as possible [4]. The aim is to allow faster evaluation of properties versus IAPWS95.

The IAPWS95 model equation uses density and temperature as independent variables. The IAPWS-IF97 contains five different equations that use a combination of density-temperature and pressure-temperature as independent variables. However, the current desired independent variable space for the solver is pressure-internal energy. Thus any evaluation of properties must invert the model equations in either case. This need is a key reason to tabulate the models, as the tabulation may be done directly in the desire pressure-internal energy space. However, this then invalidates any speed gains between IAPWS95 and IAPWS-IF97 evaluations since both will be equally fast interpolating on tables. Then the key difference between the models is the extended high temperature range of IAPWS-IF97.

As the analytic equations are well validated, the main concern for tabulation is verification that the values represent the desired model within some desired tolerance. To enable this process, the implementation of the analytic models are verified on three levels. First, the standards documents define code verification tests for a subset of quantities at a limited number of points in the domain of applicability. Implementation of all the models have been tested successfully against these values and found to be in good agreement.

The second level of verification deals with consistency and accuracy of the variables that are not reported in the reference documents. This involves both additional variables at the reported verification points, as well as verifying the implementation of the thermodynamic variables across the full domain of interest. This latter step requires defining the liquid-vapor coexistence region, which is not explicitly reported in the reference documents. In the coexistence region, Maxwell constructions have been generated with a critical scaling correction close to the critical

point. Verification of derivatives of the Helmholtz or Gibbs potentials is then performed via fifth order finite differences.

The third level verifies the implementation of the inversion algorithms. For example, if one wishes to know the density R as a function of the pressure P and internal energy E, R(P,E), then the inversion routines are verified as follows. In R-T space, one first calculates P1(R,T) and E1(R,T). Then one uses the inversion routine to calculate R1 = R(P1,E1). Checking that R1 == R completes the verification process. This process is applied to all the desired thermodynamic quantities.

4.3.2 Tabulation of Properties

Once a verified implementation of the models is available, the next step is to tabulate these models for use in state evaluations. The main goal of such tabulation is to speed up the evaluation of state properties. This is accomplished through tabulation of the models directly into the desired pressure-internal energy phase space, avoiding multiple evaluations of the model polynomials. It is important, however, to verify that the tabulated properties still represent the analytic model.

A new unstructured triangular (UTri) tabular format accomplishes these goals by allowing adaptation of the table grid so as to ensure a minimal amount of tabulated points that, when interpolated, reproduce the analytic models to within a certain error tolerance. Linear interpolation on the triangles provides for a very efficient computation. However, this means derivative information is not reliable. So, all desired quantities are tabulated for interpolation. This results in thermodynamic inconsistencies on the same order as the error tolerance. Efficient look up of thermodynamic states is accomplished through a tree structure that subdivides the phase space into regions containing roughly an equal number of triangles. Once a state is placed in one of these regions, the triangles contained therein are searched through using their barycentric coordinates to determine the triangle containing the interpolation point.

Construction of a table requires specification of the desired model, error tolerance, error sample size, independent variables, and table bounds. Currently the IAPWS95 and IAPWS-IF97 models are supported and implicitly include the Thcon11 and Visc08 models. Pressure-internal energy is the only supported phase space, although in the future both pressure-entropy and pressure-enthalpy will be made available. The table bounds are specified as a rectangular region in pressure-temperature space. This space is then warped into the desired space. Thermal stability ($dX/dT|P>0$) of the models ensure this mapping results in a valid boundary in the desired space. To simplify the triangle look up process described above, a rectangular space is then regenerated by adding boundary triangles along the borders of the warped space. The result may be seen in Fig. 65. As these additional triangles lie flat along the boundary, interpolation points that fall in this region may be straightforwardly clipped to the pressure-temperature table bounds. A side effect of this boundary triangle addition is that discontinuities along the warped boundaries are not allowed. Practically, this means that no phase boundary, such as the vapor curve, may intersect the minimum and maximum temperature boundaries. This does slightly restrict the freedom in choosing the domain for tabulation.

Once the tabulation boundaries are defined, the location of phase boundaries inside the domain are determined. Along each boundary nodes are placed adaptively to meet the desired error tolerance. All these boundaries subdivide the full domain into regions containing a single phase, or mixed phase. Each of these phase regions is then meshed by adaptively placing nodes inside the region until the desired error criteria is met. The error is sampled along the boundaries on a uniform grid in the barycentric coordinate system. Together the error tolerance and sample size define the verification level of the tabulation.

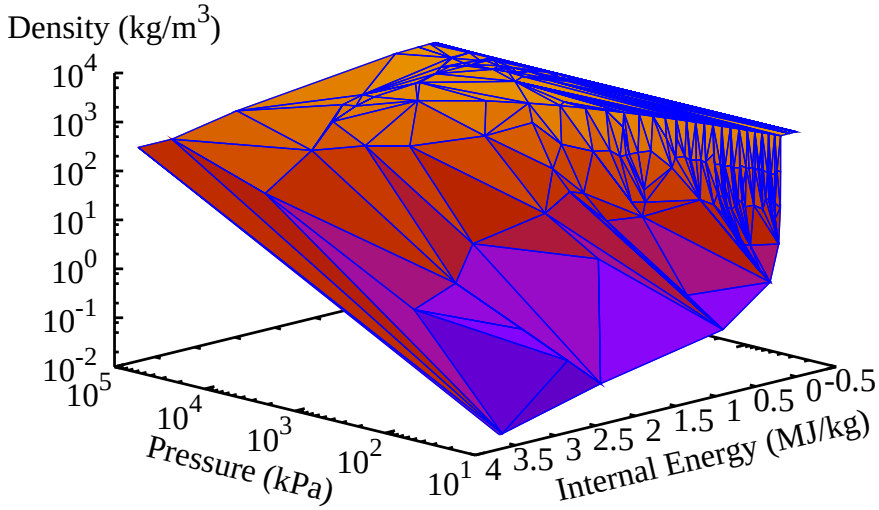

Figure 65: Tabulated density surface with triangulation overlaid in blue for the IAPWS-IF97 model.

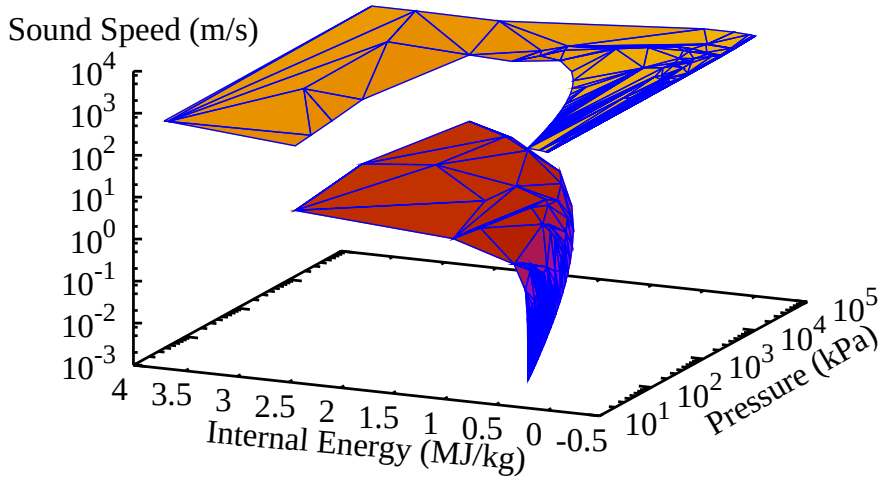

Figure 66: Tabulated adiabatic sound speed surface with triangulation overlaid in blue for the IAPWS-IF97 model.

Once generated, UTri tables are stored in NetCDF format and read into a code such as Hydra-TH through an interpolation package [18]. The thermodynamic variables at a given pressure-internal energy state may be evaluated through a standard interface that supports vectorization. The variables that may be returned for such a state evaluation are enthalpy, entropy, density, temperature, Gibb's free energy, Helmholtz free energy, adiabatic sound speed, isothermal bulk

modulus, isobaric heat capacity, isothermal heat capacity, dynamic viscosity, thermal conductivity, and an identifier for material phase. Figs. 65 and 66 display the density and adiabatic sound speed results for a tabulation of the IAPWS-IF97 model for the region with pressure in the range 0.01-100 MPa and temperature in the range 273.16-1073.15 K at a tolerance of 1.0 with 2 samples along an edge, resulting in a 289 node table. The density is continuous across the space, despite the small discontinuities in the analytic model. This is a designed modification of the IAPWS-IF97 model which has artificial boundaries with discontinuities that are unphysical. On the other hand, the sound speed exhibits discontinuities along the vapor curve, as expected for derivatives across this phase boundary. The benefit of the unstructured triangular mesh results in a sharp resolution of this boundary. Note, although the pressure is plotted in Figs. 65 and 66 on a log scale, the tabulation was performed in linear coordinates. The adaptive tabulation naturally picks up the logarithmic nature of the thermodynamic variables.

The performance of the UTri format was evaluated in a standalone program versus an analytic implementation of the IAPWS-IF97 model from the freesteam [73] library. This freesteam model is openly available online and aims to be an efficient analytic implementation. This allows a more fair speed comparison versus the implementation used for tabulation, as this latter model has been crafted to be as accurate as possible but not optimized at all for speed. The pressure-internal energy phase space was evaluated for the table and freesteam on a rectangular 1001x1001 grid as well as at 10^6 randomly sampled points in that grid. The sample grid boundaries were from 50-100 MPa in pressure and from 1 J/kg to 1.3 MJ/kg in internal energy. At internal energies above these values, the freesteam library was encountering convergence difficulties. Since these may likely be fixed by algorithmic changes, it was decided not to penalize the freesteam timing information with those states. The UTri format was evaluated for three different tables with increasing number of nodes, implying more accurate tabulations. The bounds for the UTri tables were all from 25-100 MPa in pressure and 273.16-1073.15 K in temperature. These temperatures correspond roughly to internal energy between 0-3 MJ/kg. The resulting times, averaged over 10 runs, are shown in Tab. 1. The evaluation time for UTri tables with more nodes varies approximately linearly with the logarithm of the number of nodes. This indicates that triangle look up is dominating the algorithmic complexity of the tabular state evaluations at these node counts. The speed up found using the tabulated values is at least 100 times over the analytic model, easily meeting the L3:THM.CFD.P7.04 milestone goal of a 10 times speedup.

Table 7: Evaluation speed for analytic freesteam model versus three different UTri tabulations of the IAPWS-IF97 model.

Sample type	freesteam	UTri (89 nodes)	UTri (1805 nodes)	UTri (4564 nodes)	UTri (13529 nodes)
Mesh time (s)	42.89	0.21	0.24	0.25	0.26
Random time (s)	42.71	0.26	0.33	0.36	0.41

Finally, the table generator, model implementation, and interpolation package codes are being released as open source software under a BSD style license. Once released, they will be made available for download at http://software.sandia.gov.

4.4 Hydra-TH Multiphase Calculations

This section presents two prototypical multiphase computations using Hydra-TH and the "Option-1" solution algorithm. A single-span 3x3 rod-bundle is presented first, and followed by a 5x5 rod bundle calculation with interphase momentum exchange.

4.4.1 3x3 Rod Bundle

The flow conditions for the 3x3 rod bundle follow those used by Elmahdi, et al. [63]. For the calculation reported here, the working fluid for the continuous phase is water at a temperature of 394.2 K, a density of 942.0 kg/m^{3,} and a dynamic viscosity of 2.32x10^{-4} kg/m/s. The inlet velocity is prescribed as **v** = (0, 0, 5) m/s. This corresponds to a Reynolds number, based on the rod diameter, of Re_D = 1.93x10^5, while the Reynolds number based on the hydraulic diameter is Re_{Dh} = 4.01x10^5. The hydraulic diameter is defined as D_h =4 A_{flow}/P_{wet} where A_{flow} is the cross-sectional flow area, and P_{wet} is the wetted-perimeter. No-slip, no-penetration conditions are prescribed at the rod and spacer surfaces. At the outlet, the hydrostatic pressure is specified to be p_h = 0 in conjunction with a zero shear stress condition. For the first set of calculations, no-penetration conditions with in-plane slip in the axial flow direction were applied at the sub-channel boundaries as shown in Figure 67

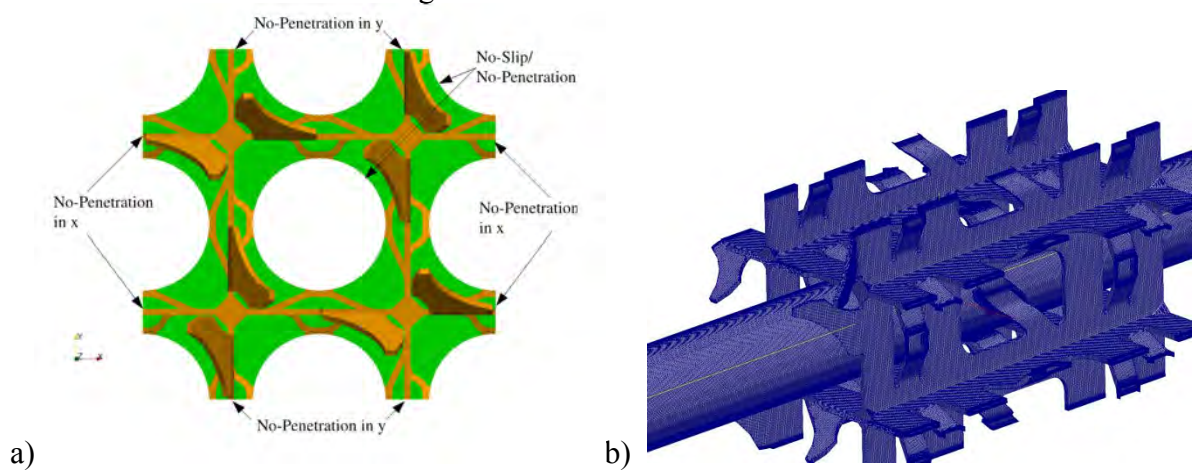

Figure 67: 3x3 Rod bundle showing a) boundary conditions on rod, spacer surfaces, and the sub-channel boundaries, b) surface mesh of the rod surface and spacer grid.

This test is intended to demonstrate the ability of the current algorithm to solve problems where there is a volume fraction wave. For this purpose, the densities of the two phases are identical, and the initial volume fractions were 0.5 for each phase. At the inlet to the domain, the continuous liquid volume fraction is 0.9 resulting is an abrupt shock-like structure in the volume fraction that is convected downstream past the spacer grid.

Figure 68 shows a snapshot of the instantaneous volume fraction isosurfaces for the bubbly phase near the spacer grid. This calculation has been scaled up to a 192M element mesh on Titan using approximately 36,000 cores as a preliminary multiphase "stress test".

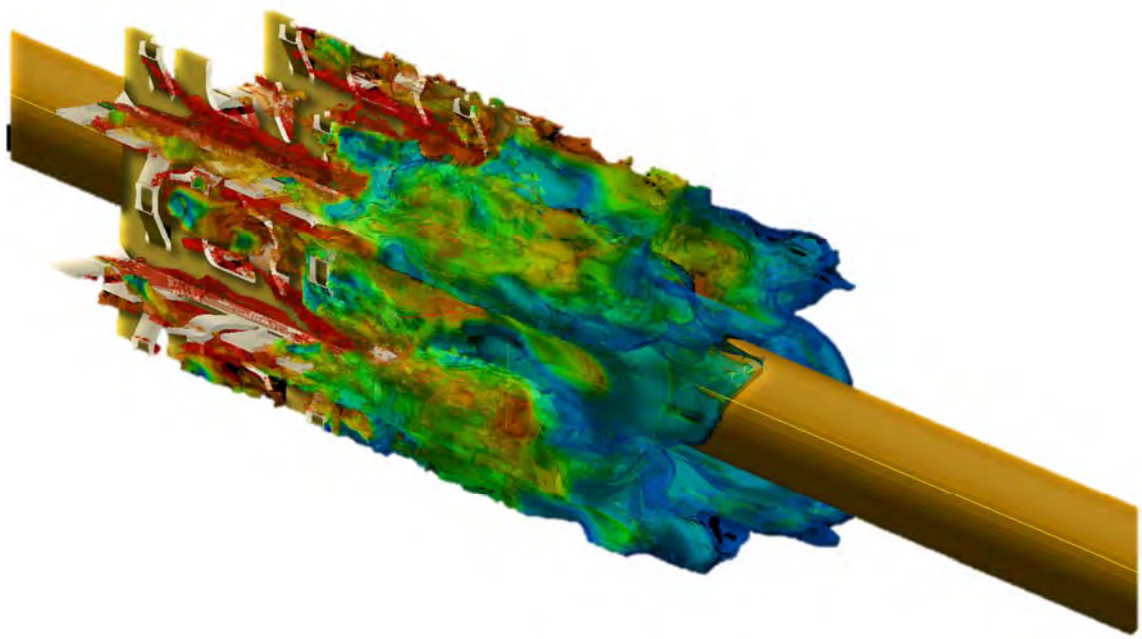

Figure 68: Snapshot of isosurfaces of the instantaneous phasic volume fraction near the spacer grid using the 2M mesh.

4.4.2 5x5 Rod Bundle

This section presents the results of ILES calculations for the 5x5 fuel rod bundle. The geometry was provided in CAD format by Westinghouse, and corresponds to the experimental configuration used at Texas A&M where PIV measurements were carried out. The flow domain is shown in Figure 69. Not shown here are the exterior walls of the flow housing used in the experimental facility.

At the flow domain inlet, a prescribed velocity $v = (0.0, 2.48, 0.0)$ m/s was used for the continuous liquid with the fluid properties for water at 24° C. The bubble phase used a prescribed velocity $v = (0.0, 1.24, 0.0)$ m/s. This corresponds to a Reynolds number of approximately 28,000 based on the hydraulic diameter for the rod bundle and the liquid phase. The phasic velocity difference was intentionally imposed to demonstrate the effect of the interphase momentum exchange. At the surfaces of the flow housing, rods, support and spacer grids, no-slip/no-penetration velocity conditions were prescribed for all phases. Homogeneous Neumann conditions for velocity (zero normal viscous stress) along with a zero pressure condition were prescribed at the outflow plane. The initial volume fraction was 0.99 for the liquid phase, and 0.01 for the bubble phase. Here, a liquid/bubble density ration of 100:1 was used with a bubble diameter of 10 mm and fixed drag coefficient $C_d = 0.44$.

In contrast to earlier single-phase problems performed using ILES, this computation quickly reaches a steady-state condition. Figure 70 shows a snapshot of the instantaneous bubble

velocity in the streamwise direction in the 5x5 rod bundle. The influence of the spacer grid and mixing vane on the local bubble velocity is clear with a short recovery zone downstream of the both the spacer and mixing vane.

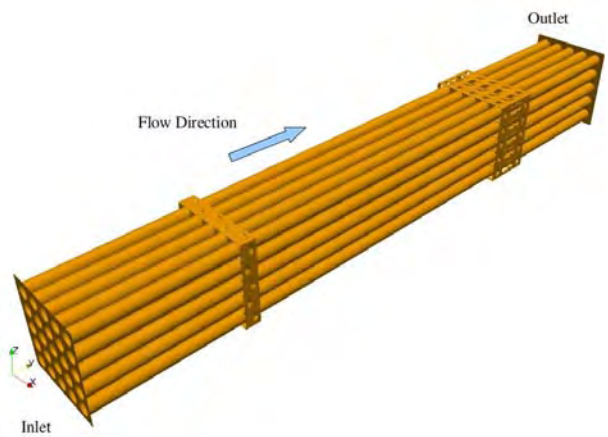

Figure 69: Flow domain for the 5x5 rod bundle showing the rods, the inlet/outlet planes, rod support, and the spacer grid.

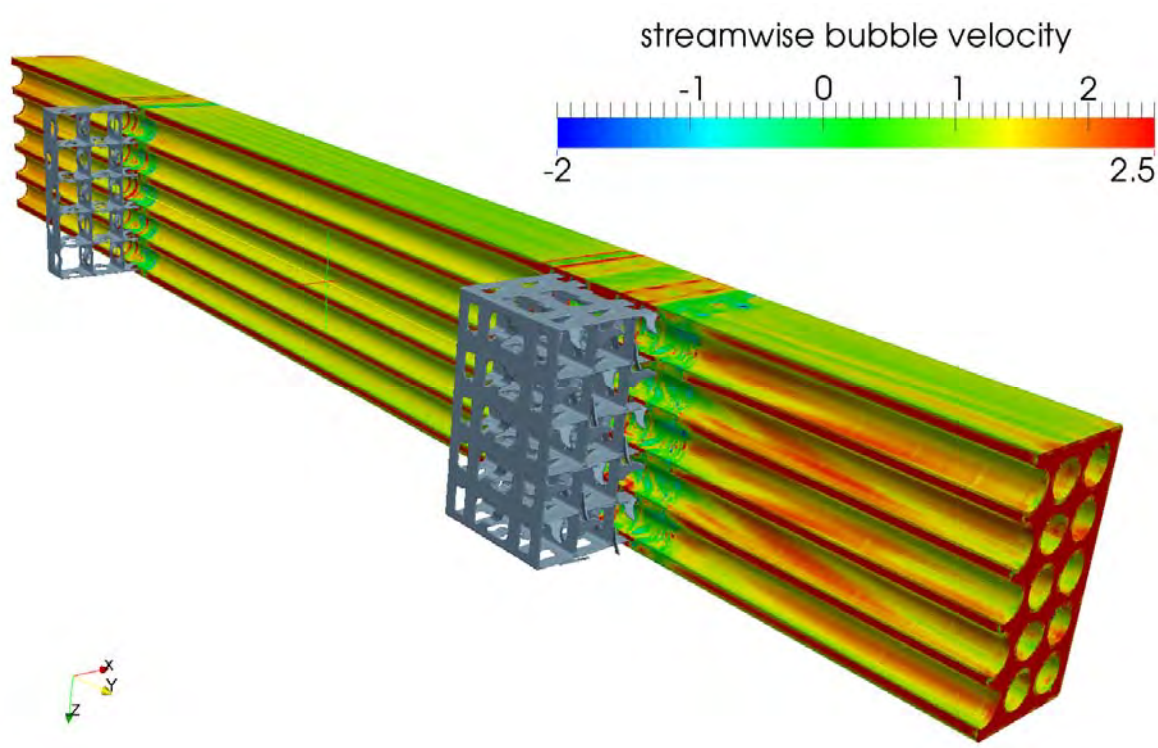

Figure 70: Snapshot of the instantaneous bubble velocity in the streamwise direction.

Figure 71 shows a snapshot of the isosurfaces of the velocity difference between the continuous liquid and bubble phases. The isosurface colors indicate the magnitude of the streamwise drag between the phases. In the region downstream of the spacer grid and mixing vane, the drag force is increased indicating a larger difference in velocity between the continuous liquid and the bubble phases. It would appear that the presence of the bubble phase, with a much lower effective Reynolds number, and the interphase momentum exchange results in a flow field that achieves a steady-state relatively quickly.

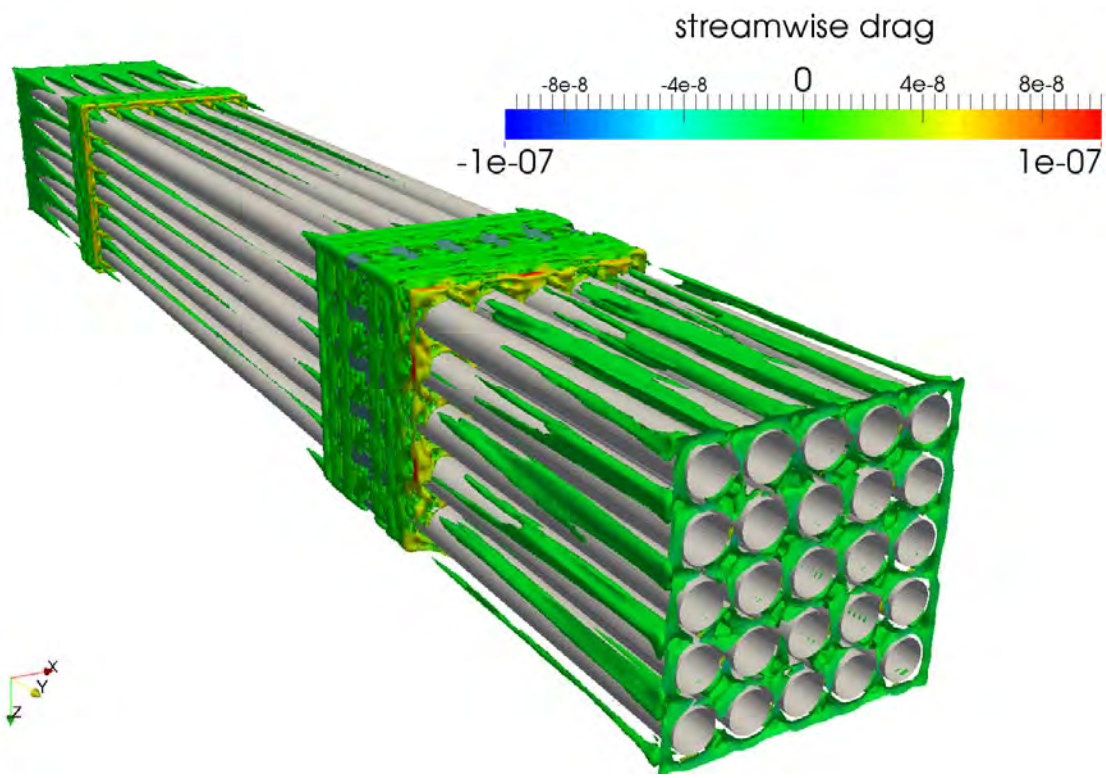

Figure 71: Isosurfaces of the velocity magnitude for the velocity difference between the continuous liquid and bubble phases with the color indicating the magnitude of the streamwise drag.

5. SUMMARY

The work presented in this milestone report is focused on the assessment and demonstration of advanced modeling capabilities for multiphase flow with sub-cooled boiling. The milestone first considers a baseline multiphase model for sub-cooled boiling, i.e., the RPI Baseline model, and its independent implementation and assessment in STAR-CCM+. A new advanced boiling closure model is presented along with the very important use of innovative experiments and ITM/DNS for gaining new physical insights for closure model development. Finally, a preliminary snapshot of the Hydra-TH multiphase capabilities with a development roadmap is presented.

Efforts with the RPI model have shown that the model is reasonably mature and portable in terms of the underlying code infrastructure and discretization making it amenable for direct use in Hydra-TH. As expected, the assessment of the model has shown model sensitivities that will require further improvement under the scrutiny of VUQ studies. Comparisons with the Bartolomei, DEBORA and PSBT experiments have underscored the limitations of the existing experimental data. Finally, extension of this model beyond sub-cooled boiling under PWR conditions will require additional model development.

The role of the advanced and innovative non-invasive experimental methods and ITM/DNS calculations can't be understated. At this point, there has been significant physical understanding gained from the ITM/DNS investigations of bubble forces under various flow shear conditions. These results have been instrumental in hypothesizing an integrated and coherent lift closure model that we hope will eventually provide a standard in closure modeling. The data and insights gained by the sub-cooled boiling experiments have spawned a new advanced boiling model that includes physical phenomena that we view as enabling technology for more predictive critical heat-flux calculations in the future. Finally, the core multiphase code base has been delivered in Hydra-TH for the "option-1" solution algorithm. Preliminary computations have demonstrated that the code infrastructure has retained the parallel scalability of the single-phase flow solver.

Future efforts based on this work will continue to focus on improving multiphase closure models and integrating the "best-in-class" models in Hydra-TH for direct application to the CASL challenge problems. Based on this work, future efforts will

- Explore the effects of high-bubble count on derived turbulent statistics based on ITM/DNS. The goal being to improve the understanding and modeling capabilities for multiphase turbulence closures.
- Continue to explore and improve momentum and boiling closures. Eventually, the role of near-wall effects, CRUD deposition and chimney formation, need to be addressed. For this purpose, direct integration of the MAMBA code into Hydra-TH as a sub-grid scale model is being investigated.
- Finally, as the overall fidelity of multiphase sub-cooled boiling calculations is limited by the quality of closure models, we will continue to invest in efforts to improve our understanding of multiphase phenomena with much directed experimental investigations.

6. REFERENCES

1. NUREG-0800, "U.S. Nuclear Regulatory Commission Standard Review Plan 4.4, Thermal and Hydraulic Design," Revision 2, March 2007.
2. NEA/NSC/DOC(2005)5, ISBN 92-64-01088-2, "OECD-NEA/US-NRC/NUPEC BWR Full-size Fine-mesh Bundle Test (BFBT) Benchmark, Volume I: Specifications, OECD 2006", OECD Nuclear Energy Agency, August 2006
3. NEA/NSC/DOC(2012)1, "OECD/NEA Benchmarking Based on NUPEC PWR Subchannel and Bundle Test (PSBT), Volume 1: Experimental Database and Final Problem Specifications," OECD Nuclear Energy Agency, June 2012.
4. Sensitivity Study of CFD Flow Results to Phase-to-Phase Heat and Momentum Transfer Parameters and to Boiling Models - CASL Milestone L3-THM-CFD-P3-01.
5. M.Z. Podowski, "Mechanistic Modeling of Boiling Heat Transfer", Nuclear Engineering and Technology, Vol. 44, No. 8, December 2012.
6. D. R. Shaver, S. P. Antal and M. Z. Podowski, "Multidimensional Mechanistic Modeling of Interfacial Heat and Mass Transfer", Proceedings of ICAPP'12, Paper 12274, June, 2012, pp.2062-2072.
7. M.Z. Podowski, "Mechanistic Modeling of Boiling Heat Transfer", Proc. Embedded Topical Meeting: Advances in Thermal-Hydraulics, 2012 ANS Winter Meeting, San Diego, CA, November 2012, pp.1-5.
8. 5. H. Jiao and M. Z. Podowski, An Analysis of Multidimensional Models of Gas/Liquid Flows", ANS Proc., 2012 Winter Meeting, San Diego, CA, November, 2012, pp.1393-1394.
9. D.R. Shaver, S.P. Antal, and M.Z. Podowski, "Development, Testing, and Validation of a Multidimensional Model of Subcooled Boiling", ANS Transactions, 2012 Winter Meeting, San Diego, CA, November, 2012, pp. 1366-1368.
10. B.M. Waite, D.R. Shaver and M.Z. Podowski, "Multidimensional Analysis of Flow through Sudden Expansions and Contractions in Pipes", ANS Transactions, 2012 Winter Meeting, San Diego, CA, November, 2012, pp. 1336-1368.
11. N. Dinh, "CIPS validation data plan," INL, Tech. Rep. INL/EXT-12-25347, March 2012.
12. J. Klausner, R. Mei, D. Bernhard, and L. Zeng, "Vapor bubble departure in forced convection boiling," International Journal of Heat and Mass Transfer, vol. 36, no. 3, pp. 651–662, 1993.
13. R. Sugrue and J. Buongiorno, "A modified force-balance model for predicting bubble departure diameter in subcooled flow boiling," in Proceedings of The 15th International Topical Meeting on Nuclear Reactor Thermal-Hydraulics, NURETH-15, 2013.
14. R. Sugrue, T. McKrell, and J. Buongiorno, "On the effects of orientation angle, subcooling, mass flux, heat flux, and pressure on bubble departure diameter in subcooled flow boiling." in Proceedings of Computational Fluid Dynamics in Nuclear Reactor Safety - 4, 2012.
15. N. Basu, G. R. Warrier, and V. K. Dhir, "Wall heat flux partitioning during subcooled flow boiling: Part 1-model development," Journal of Heat Transfer, vol. 127, pp. 131–140, February 2005.
16. R. Judd and K. Hwang, "A comprehensive model for nucleate boiling heat transfer including microlayer evaporation," J Heat Transfer, vol. 115, pp. 955-962, 1976.
17. N. Kurul and M. Podowski, "Multidimensional effects in sub-cooled boiling," in Proceedings of the Ninth Heat Transfer Conference, Jerusalem, 1990.

18. G. H. Yeoh and J. Tu, Computational Techniques for Multi-Phase Flows, Elsevier, 2010.
19. M.-O. Kim, J. Tu, G. H. Yeoh and G.-C. Park, "On Population Balance Approach for Subcooled Boiling Flow Prediction," Journal of Heat Transfer, vol. 127, pp. 253-264, 2005.
20. T. Lee, G. Park and D. Lee, "Local Flow characteristics of Subcooled Boiling Flow of Water in a Vertical Concentric Annulus," International Journal of Multiphase Flow, vol. 28, no. 8, pp. 1351-2368, 2002.
21. L. Zeng, J. Klausner, D. Bernhard and R. Mei, "A Unified Model for the Prediction of Bubble Detachment Diameters in Boiling Systems- II. Flow Boiling," International Journal of Heat and Mass Transfer, vol. 36, no. 9, pp. 2271-2279, 1993.
22. D. Chatzikyriakou, D. Caviezel, J. Buongiorno and D. Lakehal, "ITM Test Case 1: LES and DNS of turbulent flow in a closed channel with flat walls featuring a pattern of small hemispherical solid obstacles," Cambridge, MA, 2011.
23. B. Yun, A. Splawski, S. Lo and C.-H. Song, "Advanced Wall Boiling Model for the Subcooled Boiling Flow with CFD Code," in The Seventh Korea-Japan Symposium on Nuclear Thermal Hydraulics and Safety, Chuncheon, Korea, 2010.
24. R. Situ, T. Hibiki, M. Ishii and M. Mori, "Bubble Lift-Off Size in Forced Convective Subcooled Boiling Flow," International Journal of Heat and Mass Trasnfer, vol. 48, pp. 5536-5548, 2005.
25. W Fullmer, S Pannala, and I Bolotnov. Initial assessment of nphase-cmfd for application to adiabatic bubbly two-phase pipe flow. Technical report, CASL, 2011.
26. D. Legendre and J. Magnaudet. The lift force on a spherical bubble in a viscous linear shear flow. Journal of Fluid Mechanics, 368:81-126, 1998.
27. Bolotnov, I. et al., 2011. Detached Direct Numerical Simulation of Turbulent Two-phase Bubbly Channel Flow. Int. J. Multiphase Flow, Volume 37, pp. 647-659.
28. Biswas, S., Esmaeeli, A. & Tryggvason, G. 2005 Comparison of results from DNS of bubbly flows with a two-fluid model for two-dimensional laminar flows. Int. J. Multiphase Flows 31, 1036–1048.
29. Brackbill, J. U., Kothe, D. B. & Zemach, C., 1992. A continuum method for modeling surface tension. J. Computational Physics, 100(2), pp. 335-354.
30. Bunner, B. & Tryggvason, G. 2002a Dynamics of homogeneous bubbly flows. Part 1. Rise velocity and microstructure of the bubbles. J. Fluid Mech. 466, 17–52.
31. Bunner, B. & Tryggvason, G. 2002b Dynamics of homogeneous bubbly flows. Part 2. Velocity fluctuations. J. Fluid Mech. 466, 53–84.
32. Bunner, B. & Tryggvason, G. 2003 Effect of bubble deformation on the stability and prop- erties of bubbly flows. J. Fluid Mech. 495, 77–118.
33. Esmaeeli, A. & Tryggvason, G. 2005 A direct numerical simulation study of the buoyant rise of bubbles at O(100) Reynolds number. Phys. Fluids 17, 093303.
34. Dijkhuizen, W., Roghair, I., Annaland, M. Van Sint & Kuipers, J. 2010a DNS of gas bubbles behaviour using an improved 3d front tracking model–drag force on isolated bubbles and comparison with experiments. Chem. Eng. Sci. 65, 1415–1426.
35. Dijkhuizen, W., Roghair, I., Annaland, M. Van Sint & Kuipers, J. 2010b DNS of gas bubbles behaviour using an improved 3d front tracking model–model development. Chem. Eng. Sci. 65, 1427–1437.
36. Hao, Y. & Prosperetti, A. 2004 A numerical method for three-dimensional gas–liquid flow computations. J. Comput. Phys. 196, 126–144.

37. Hua, J. & Lou, J. 2007 Numerical simulation of bubble rising in viscous liquid. J. Comput. Phys. 222, 769–795.
38. Jansen, K. E., 1993. Unstructured grid large eddy simulations of wall bounded flows. Annual Research Briefs, Center for Turbulence Research, NASA Ames/Stanford University, p. 151.
39. Jansen, K. E., 1999. A stabilized finite element method for computing turbulence. Comp. Meth. Appl. Mech. Eng., Volume 174, pp. 299-317.
40. Muradoglu, M. & Kayaalp, A. D. 2006 An auxiliary grid method for computations of multiphase flows in complex geometries. J. Comput. Phys. 214, 858–877.
41. Nagrath, S., Jansen, K. E., Lahey, R. T. & Akhatov, I., 2006. Hydrodynamic simulation of air bubble implosion using a FEM based level set approach. Journal of Computational Physics, Volume 215, pp. 98-132.
42. Sahni, O. et al., 2006. Efficient anisotropic adaptive discretization of the cardiovascular system. Computer Methods in Applied Mechanics and Engineering, 195(41-43), pp. 5634-5655.
43. Sethian, J. A., 1999. Level set methods and fast marching methods. s.l.:Cambridge University Press.
44. Sussman, M. et al., 1999. An adaptive level set approach for incompressible two-phase flows. J. Computational Physics, 148(1), pp. 81-124.
45. Sussman, M. & Fatemi, E., 1999. An efficient, interface-preserving level set re-distancing algorithm and its application to interfacial incompressible fluid flow. Siam J. on Scientific Computing, 20(4), pp. 1165-1191.
46. Sussman, M., Fatemi, E., Smereka, P. & Osher, S., 1998. An improved level set method for incompressible two-phase flows. J. Computers & Fluids, 27(5-6), pp. 663-680.
47. Sussman, M. & Smereka, P., 1997. Axisymmetric free boundary problems. J. Fluid Mech., Volume 341, pp. 269-294.
48. Tejada-Martinez, A. E. & Jansen, K. E., 2005. A parametric-free dynamic subgrid-scale model for large-eddy simulation. Computer Methods in Applied Mechanics and Engineering, 194(9), pp. 1225-1248.
49. Tomiyama, A., Tamai, H., Zun, I. & Hosokawa, S. 2002 Transverse migration of single bubbles in simple shear flows. Chem. Eng. Sci. 57, 1849–1858.
50. Tryggvason, G., Bunner, B., Esmaeeli, A., Juric, D., Al-Rawahi, N., Tauber, W., Han, J., Nas, S. & Jan, Y.-J. 2001 A front tracking method for the computations of multiphase flow. J. Comput. Phys. 169, 708–759.
51. Tryggvason, G., Scardovelli, R. & Zaleski 2011 Direct Numerical Simulations of Gas-Liquid Multiphase Flow. Cambridge University Press.
52. Unverdi, S. O. & Tryggvason, G. 1992 A front-tracking method for viscous, incompressible, multi-fluid flows. J. Comput. Phys. 100, 25–37.
53. van Sint Annaland, M., Dijkhuizen, W., Deen, N.G. & Kuipers, J.A.M. 2006 Numerical simulation of gas bubbles behaviour using a 3D front tracking method. AIChE J. 52, 99–110.
54. Whiting, C. H. & Jansen, K. E., 2001. A stabilized finite element formulation for the incompressible Navier-Stokes equations using a hierarchical basis. International Journal of Numerical Methods in Fluids, Volume 35, pp. 93-116.
55. Zhou, M. et al., 2010. Cardiovascular flow simulation at extreme scale. Comput. Mech., Volume 46, pp. 71-82.

56. R. Nourgaliev and M. Christon, *Solution Algorithms for Multi-Fluid-Flow Averaged Equations*, Tech. Rep. INL/EXT-12-27187, Idaho National Laboratory, December, 2012.
57. R. Nougaliev, M. Christon and J. Bakosi, *Notes on the Newton-Krylov Based Incompressible Flow Projection Solver*, Tech. Rep. INL/EXT-12-27197, Idaho National Laboratory, December, 2012.
58. R. Nourgaliev, M. Christon, and J. Bakosi, *Newton-Krylov Based P2 Projection Solver for Fluid Flows*, Tech. Rep. INL/EXT-13-2878, Idaho National Laboratory, January, 2013.
59. R. Nourgaliev, M. Christon, J. Bakosi, R. Lowrie and L. Pritchett-Sheats, *Hydra-TH: a Thermal-Hydraulics Code for Nuclear Reactor Applications*, in NURETH-15 – Fifteenth International Topical Meeting on Nuclear Reactor Thermal Hydraulics, Pisa, Italy, May 2013.
60. J. Bakosi, M. A. Christon, L.A. Pritchett-Sheats, and R. R. Nourgaliev, *Hydra-TH Advanced Capabilities (L3 Milestone THM.CFD.P6.01)*, LA-UR 13-20572, Los Alamos National Laboratory, January, 2013.
61. D. Z. Zhang, W.B. VanderHeyden, Q. Zou, Xia Ma, and P.T. Giguer, *CartaBlanca Multiphase Flow Equations and Numerical Methods*, LA-UR-07-3621, Los Alamos National Laboratory, December, 2007.
62. D. Z. Zhang, *Personal Communication*, May, 2013.
63. Elmahdi A., Lu R., Conner M., Karoutas Z., Baglietto E., *Flow Induced Vibration Forces on a Fuel Rod by LES CFD Analysis*, NURETH 14-365, Toronto, Canada, September 2011.
64. D. G. Friend and R. B. Dooley, "Revised Release on the IAPWS Formulation 1995 for the Thermodynamic Properties of Ordinary Water Substance for General and Scientific Use", (International Association for the Properties of Water and Steam, Doorwerth, The Netherlands, 2009). Available from http://www.iapws.org.
65. W. Wagner and A. Pruss, "The IAPWS Formulation 1995 for the Thermodynamic Properties of Ordinary Water Substane for General and Scientific Use", J. Phys. Chem. Ref. Data 31, 387-535 (2002).
66. J. R. Cooper and R. B. Dooley, "Revised Release on the IAPWS Industrial Formulation 1997 for the Thermodynamic Properties of Water and Steam", (International Association for the Properties of Water and Steam, Lucerne, Switzerland, 2007). Available from http://www.iapws.org.
67. W. Wagner, et. al., "The IAPWS Industrial Formulation 1997 for the Thermodynamic Properties of Water and Steam", J. Eng. Gas Turbines & Power 122, 150-182 (2000).
68. J. R. Cooper and R. B. Dooley, "Release on the IAPWS Formulation 2008 for the Viscosity of Ordinary Water Substance", (International Association for the Properties of Water and Steam, Berlin, Germany, 2008). Available from http://www.iapws.org.
69. M. L. Huber, et. al., J. Phys. Chem. Ref. Data 38, 101 (2009).
70. K. Daucik and R. B. Dooley, "Release on the IAPWS Formulation 2011 for the Thermal Conductivity of Ordinary Water Substance", (International Association for the Properties of Water and Steam, Plzen, Czech Republic, 2011). Available from http://www.iapws.org.
71. M. L. Huber, et. al., J. Phys. Chem. Ref. Data 41, 033102 (2012).

72. J. H. Carpenter and N. Belcourt, "Tabular water properties interface for Hydra-TH: CASL THM.CFD.P6.03 Milestone Report",Tech. Rep. SAND2013-2697, Sandia National Laboratories (2013).
73. Freesteam is available from http://freesteam.sourceforge.net/.
74. T. Cebeci and P. Bradshaw, Momentum Transfer in Boundary Layers, Hemisphere/McGraw-Hill, 1977.
75. H. Schlichting and K. Gersten, Boundary Layer Theory, New York: Springer, 2000.
76. B. Phillips, J. Buongiorno and T. McKrell, "Nucleation Site Density, Bubble Departure Diameter, Bubble Departure Freqency, and Local Temperature Distribution in Subcooled Flow Boiling of Water," CASL L3.THM.CLS.P7.01, Cambridge, MA, 2013.
77. X. Duan, B. Phillips, T. McKrell and J. Buongiorno, "Synchronized high-speed video, infrared thermometry, and particle image velocimetry data for validation of interface-tracking simulations of nucleate boiling phenomena," *Experimental Heat Transfer,* vol. 26, pp. 169-197, 2013.